TECHNISCHE UNIVERSITÄT MÜNCHEN
Lehrstuhl für Physik funktionaler Schichtsysteme, E10

Control of Spin Waves on the Nanoscale in One-Dimensional Magnonic Crystals and Atomic Layer Deposition of Metallic Ferromagnets for Second Generation of Nanomaterials

Rupert Huber

Vollständiger Abdruck der von der Fakultät für Physik der Technischen Universität München zur Erlangung des akademischen Grades eines

Doktors der Naturwissenschaften

genehmigten Dissertation.

Vorsitzender: Univ.-Prof. Dr. Peter Vogl
Prüfer der Dissertation:
1. Univ.-Prof. Dr. Dirk Grundler
2. Univ.-Prof. Paolo Lugli, Ph.D.

Die Dissertation wurde am 08.10.2013 bei der Technischen Universität München eingereicht und durch die Fakultät für Physik am 06.12.2013 angenommen.

Abstract

Spin waves (SWs) in arrays of ferromagnetic nanowires, so called one-dimensional magnonic crystals and atomic layer deposition (ALD) of metallic ferromagnets have been studied. The arrays of nanowires were fabricated by electron beam lithography of about 30 nm thick permalloy $Ni_{80}Fe_{20}$. By all electrical spectroscopy in the GHz regime propagating SWs were investigated. SW propagation across several air gaps was found. In the artificial antiferromagnetic configuration of the structure reciprocal excitation of Damon-Eshbach like SWs was discovered. This is attributed to a metamaterial behavior. It was found that a reprogrammable magnetic defect is a nanoscale semitransparent mirror for SWs. ALD of Ni and NiFe alloys has been improved to provide conformal coatings of ferromagnets with low SW damping.

Es wurden Spinwellen (SW) in einer periodischen Anordnung von ferromagnetischen Nanodrähten, sogenannten eindimensionalen magnonischen Kristallen, und die Atomlagenabscheidung (ALD) von metallischen Ferromagneten untersucht. Die periodische Anordnung von ferromagnetischen Nanodrähten wurde durch Elektronenstrahllithographie von ungefähr 30 nm dicken Permalloy $Ni_{80}Fe_{20}$ hergestellt. Durch rein elektrische Spektroskopie im GHz Bereich wurden propagierende SW untersucht. SW-Propagation über viele Luftspalte wurde nachgewiesen. In der künstlichen, antiferromagnetischen Konfiguration der Struktur wurde eine reziproke Anregung von Damon-Eshbach-artigen SW entdeckt. Dies wird durch dessen Metamaterialverhalten erklärt. Es wurde gezeigt, dass ein programmierbarer, magnetischer Defekt ein nanoskaliger, teildurchlässiger Spiegel für SW ist. ALD von Ni- und NiFe- Legierungen wurde verbessert um konforme Abscheidung von Ferromagneten mit niedriger Spinwellendämpfung zu liefern.

Contents

Scientific Collaboration

Parts of this thesis have profited by scientific collaborations. The author would like to state the contributions by the respective researchers:

- Plane wave method calculations have been conducted by Dr. M. Krawczyk at Adam Mickiewicz University in Poznań, Poland. He provided the reprogrammable band structures of magnonic crystals.
- Transmission electron microscopy and electron energy loss spectroscopy have been performed by Prof. Dr. Jordi Arbiol at Universitat Autònoma de Barcelona, Spain.
- Magnetic force microscopy has been performed at Institute for Technical Electronics at Technische Universität München with kind help by Dr. Markus Becherer.
- Anisotropic magnetoresistance measurements have been conducted by Daniel Rüffer at École Polytechnique Fédérale de Lausanne, Switzerland.

The author would like to express his gratitude for the productive collaborations.

1 Motivation and Introduction

In the last decade life has changed significantly by the incredible progress in information technology, the so called digital revolution. One of the important contributions is the development of tailored radio frequency components. The wavelength of radio frequency electromagnetic waves is in the range of some centimeters, which determines the typical dimensions of conventional electromagnetic components. Only the coupling of electromagnetic waves to elementary excitations of solids has shrunk the wavelength, and simultaneously the dimensions of radio frequency components, by orders of magnitudes. For instance, key components for information processing in wireless local area networks are radio frequency filters. By using bulk acoustic waves (phonons) the functional area of the filter component has a size of several micrometers yielding small-sized, commercially available wireless local area network products.
Restrictions of recent technologies, such as the shortage of external tuning, can be dealt by collective spin excitations in ferromagnetic material. These excitations are called magnons, which is the quasiparticle of wave-like excitations that are known as spin waves.
For spin waves the electromagnetic and the exchange interaction contribute to the wave-like excitations. Both interactions yield the versatile spin wave characteristics. The physics of both contributions are very different: (i) the exchange interaction dominates the interplay of spins on a length scale of a few nanometers, (ii) while the long-ranged electromagnetic, dipolar interaction influences on the spin-spin interaction even up to very long distances. Due to these strong interactions the wavelength of spin waves shrinks in contrast to an electromagnetic wave in vacuum similar to the abovementioned case. Therefore, nanostructuring of ferromagnetic material allows for manipulating the spin wave properties.

The investigation of spin dynamics in such nanostructured ferromagnets is an emerging field of research. [Kru10, Neu09b, Ser10, Len11] This field is called *Magnonics* and is covering the creation, control and detection of magnons. Nanostructuring changes the magnetostatic as well as the magnetodynamic properties significantly and allows for an additional control parameter of the related effects. As example, demagnetizing effects influence the spin wave behavior drastically. This has been intensively investigated since the 1950's, where the demagnetizing field is assumed to be constant across the dimensions of a ferromagnetc body. The structuring on small length scales (nanometers) yields locally inhomogeneous demagnetizing effects. This locally inhomogeneous demagnetizing field provokes manifold effects. Nowadays, key elements in nanosciences are magnetic nanowires as they are potentially used in future technical applications, such as magnetic recording, logic operation devices, or micromagnetic sensors. [Vin05] In nanowires first approaches were done with parallel magnetization. [Gus02] This seminal work solved the dynamical magnetization problem with electromagnetic boundary condition and found a non-zero amplitude at the edge of the nanowire. This is equivalent with a dynamical electromagnetic stray field vicinal to the nanowire. Another finding was done when applying the magnetic field oblique to the nanowire. For this scenario the inhomogeneous demagnetizing field within the nanowire allows for an inhomogeneous magnetization, where the central magnetization already follows the applied magnetic field, whereas the magnetization of the edge regions remains parallel to the border. [Bai03a, Top08] In contrast to a saturated magnetization in such nanowires, where no propagating spin wave is detected, for a zig-zag magnetization a pronounced spin wave propagation is detected due to a self-cladding effect. [Due12] The above-mentioned dynamical stray field couples vicinal nanowires with a low separation (separation $\simeq$ thickness). [Gub05, Gub07, Top10, Top11b] Such periodically patterned structures are often called magnonic crystals. There, the creation of band structures has been described by a Bloch-wave ansatz for spin waves. This is similar to related fields of research, such as photonics, phononics, and plasmonics, where also the periodical patterning yields a band structure. [Leu93, Joa97, Joa08] A special case are so called reprogrammable magnonic crystals. [Top10, Tac10c, Top11b, Din11b] There, controlled by the magnetic history, distinct magnetic ground states are accessible. Thus, in one-and-the-same magnetic nanostructure different magnetic ground states, and in particular distinct unit cells of the magnonic crystal, are investigated. An interesting differentiation thereof are the reprogrammable magnonic crystals that are controlled by a so called reversal or injection pad. [Top11b] There, the switching of selected nanowires is performed by injected domain walls. [McG07] We find propagation of spin waves in one-dimensional magnonic crystals (1D MCs) consisting of an array of nanowires. In this thesis we found novel effects, such as the reciprocal excitation of spin waves in antiferromagnetically ordered 1D MCs. Several attempts have been done to provide logic elements based on propagating spin waves. An interferometric setup has been presented on yttrium iron garnet (YIG), where one interferometer arm is manipulated by the local magnetic field of an electrical current vicinal to the YIG. [Kos05, Sch08a] Another, similar setup made from Py controls the interference of two spin wave beams by different types of domain walls. [Her04] In this thesis we found that the switching of one single nanowire in the propagation path of the spin wave allows for the control of the spin wave propagation properties, which can be used as a magnetic logic element.

A very recent trend in nanoscience is the fabrication of nanomaterials. One promising and powerful technique is atomic layer deposition (ALD). It allows to cover templates that exhibit a complex topology. The rapid progress in nanotechnology and nanoscience research provides a variety of templates, so called nanomaterials. Nanospheres, nanowires, and nanoporous membranes have become available. Conformal coating by ALD onto such templates creates a *second generation of nanomaterials* [Bae11] that are novel and unexplored. Exemplarily, ALD of ferromagnetic material into nanoporous membranes result in an array of ferromagnetic nanotubes that show unprecedented reversal behavior of the magnetization. [Bac07, Dau07] A very recent trend in nanoscience is the fabrication of two [Neu08a, Neu08b, Neu10, Tac10b, Tac10a, Mad10] and three [Kos12] dimensional (2D and 3D) ferromagnetic, periodically patterned nanomaterials, so called 2D and 3D magnonic crystals. ALD is a powerful tool to create such 2D and 3D magnonic crystals, however the deposition of the necessary, low damping ferromagnetic material has been in its beginnings. A dynamical investigation of ferromagnetic material deposited by ALD is still missing at all. Therefore, the deposition of low damping ferromagnetic material and its application to nanotemplates has been conducted in this thesis. This might be used for future fabrication of 3D MCs and ferromagnetic nanomaterials.

Organization of the thesis

In Chapter 2 the theoretical background of the relevant fields in ferromagnetism and spin waves is presented, including the used numerical methods. In Chapters 3 and 4 we report on the used experimental measurement techniques and the preparation process of the studied samples. In Chapter 5 we show measured data on permalloy plain films. In Chapters 6 and 7 spin waves in a one-dimensional magnonic crystal in two different magnetic configurations are shown. The spin wave propagation through a reprogrammable magnectic defect is analyzed in Chapter 8. In Chapter 9 the atomic layer deposition technique of ferromagnetic material is presented and investigated by ferromagnetic resonance measurements. In Chapter 10 we close with a summary and outlook.

2 Theory

In this chapter basics of ferromagnetism are introduced to provide the necessary background for the experiments presented in this thesis. We discuss the different energy contributions which describe the static (Sec. 2.2) and dynamic (Sec. 2.4) behavior of the magnetization. We derive the high frequency susceptibility (Sec. 2.4.1) and address the different spin wave geometries in thin films (Sec. 2.4.4). Finally, we introduce two numerical methods for simulation of dispersion relations for spin waves in complex ferromagnetic systems (Secs. 2.5 and 2.6). For this chapter we follow substantial reviews on ferromagnetism [WD39, Kit68, Boz68, Chi97, Blu01] and on spin wave physics. [Gur96, Hil02, Sta09]

2.1 Ferromagnetism

Materials in an external magnetic field $\mathbf{H}$ exhibit a magnetization, which is described by

$$\mathbf{M} = \hat{\chi}\mathbf{H}. \tag{2.1}$$

$\hat{\chi}$ is the complex valued susceptibility tensor and describes in general an anisotropic magnetic response on a field $\mathbf{H}$. In the isotropic case $\hat{\chi} = \chi$. The susceptibility classifies solids in diamagnets ($\chi < 0$), paramagnets ($\chi > 0$), ferromagnets and ferrimagnets ($\chi \gg 0$), and antiferromagnets ($\chi \simeq 0$). For the last three types the magnetic moments are spontaneously ordered (i.e. without external field) for temperature $T < T_c$ and T_c is a critical temperature (e.g. for ferromagnets $T_c = T_C$ with T_C is the Curie temperature).

In this thesis we focus on ferromagnetic materials. There are three chemical elements that are ferromagnetic: Fe, Co, and Ni. Also alloys thereof are often ferromagnets, e.g. permalloy $Ni_{80}Fe_{20}$ (Py) which is used throughout this thesis. The magnetic flux density $\mathbf{B}$ is given by

$$\mathbf{B} = \mu_0(\mathbf{M} + \mathbf{H}) = (\hat{\chi} + 1)\mathbf{H}, \tag{2.2}$$

where μ_0 is the vacuum permeability, and $\hat{\chi} + 1$ is defined as the permeability $\hat{\mu}$.

2.2 Static Magnetization and Total Energy

The magnetic ground state $\mathbf{M}(\mathbf{r})$ in ferromagnets results from the interplay of multiple interactions. These interactions can be described as an energy landscape that is essential in order to describe the magnetization dynamics. The major energy contributions are written in a continuum model, where the magnetization $\mathbf{M}$ is given by the total of the magnetic moments divided by the enclosing volume.

Zeeman Energy

The energy contribution due to the interaction of the magnetization $\mathbf{M}$ with an external magnetic field $\mathbf{H}_{\text{ext}}$ is described by

$$\epsilon_{\text{zee}} = -\frac{\mu_0}{V} \int \mathbf{M} \cdot \mathbf{H} \, dV. \tag{2.3}$$

This energy is minimized for the magnetization having a parallel orientation with the external field.

Exchange Energy

The exchange energy, responsible for the spontaneous magnetization, is based on the Coulomb interaction in combination with the quantum mechanical Pauli exclusion principle. Two atoms with the spins $\mathbf{S_i}$ and $\mathbf{S_j}$ minimize its energy by parallel alignment of their spins. For localized spins the corresponding energy contribution is written as

$$E_{ex} = -\sum_{i,j}^{N} J_{ij}(\mathbf{S_i} \cdot \mathbf{S_j}) = -2\sum_{i<j}^{N} J_{ij}(\mathbf{S_i} \cdot \mathbf{S_j}), \tag{2.4}$$

where J_{ij} is the exchange integral. The summation is sometimes limited to nearest neighbors only, as this interaction decreases rapidly with increasing distance due to the overlap of electronic orbitals. In

spite of this limited range, the exchange interaction causes the spontaneous long range ordering in ferromagnets due to its magnitude.
In the Stoner model [Blu01] ferromagnetism of itinerant ferromagnets is discussed. For a high enough density of states at the Fermi energy $D(E_\mathrm{F})$ the reduction of Coulomb energy by a ferromagnetic ordering overcompensates the increase of kinetic energy. It can be shown that this is valid for

$$\mu_0 \mu_\mathrm{B}^2 \lambda_\mathrm{St} D(E_\mathrm{F}) \geq 1, \tag{2.5}$$

where μ_B is the Bohr magneton, the magnetic moment of an electron, and λ_St is an empirical parameter describing the average exchange field.
On a macroscopic level we make the transition to a continuum representation including the magnetization $\mathbf{M}$. The exchange energy density is written as

$$\epsilon_\mathrm{ex} = \frac{A_\mathrm{ex}}{V} \int (\nabla \mathbf{M})^2 \, dV, \tag{2.6}$$

where A_ex is a measure of the exchange stiffness.

Demagnetizing Field Energy

The demagnetizing field is a dipolar field contribution which is based on the Maxwell's equation

$$\begin{aligned} \nabla \cdot \mathbf{B} = \mu_0 \nabla \cdot (\mathbf{H}_\mathrm{dem} + \mathbf{M}) &= 0 \\ \Rightarrow \nabla \cdot \mathbf{H}_\mathrm{dem} &= -\nabla \cdot \mathbf{M} \end{aligned}$$

and

$$\nabla \times \mathbf{H}_\mathrm{dem} = 0, \tag{2.7}$$

which is valid for zero current density. Then, we can define a scalar potential Φ_dem with

$$\mathbf{H}_\mathrm{dem} = -\nabla \Phi_\mathrm{dem}, \tag{2.8}$$

which fullfils the Poisson equation

$$\Delta \Phi_\mathrm{dem} = \rho_M. \tag{2.9}$$

$\rho_M = -\nabla\mathbf{M}$ is a magnetic charge density. This standard problem in electrodynamics can be solved by a Green's function approach. [Kal86, Gus02] Generally speaking the field $\mathbf{H}_{\text{dem}}$ is generated by the divergence of the magnetization, i.e. the presence of magnetic charges. The calculation of $\mathbf{H}_{\text{dem}}$ is complicated in the general case. For a uniformly magnetized ellipsoid the following relation is valid

$$\mathbf{H}_{\text{dem}} = -\hat{\mathbf{N}}\mathbf{M}, \tag{2.10}$$

with the location-independent demagnetizing tensor $\hat{\mathbf{N}}$. When orienting the coordinate system along the principal axes of the ellipsoid, $\hat{\mathbf{N}}$ is diagonal and expressed as

$$\hat{\mathbf{N}} = \begin{pmatrix} N_x & 0 & 0 \\ 0 & N_y & 0 \\ 0 & 0 & N_z \end{pmatrix}. \tag{2.11}$$

$\hat{\mathbf{N}}$ is analytically solved for a few geometric forms. For an infinitely extended thin film one obtains $N_x = N_y = 0$, and $N_z = 1$. For thin, infinitely extended stripes with thickness t and width w there is an analytical solution. [Aha98] For the case of $\mathbf{M}$ parallel to the stripe axis ($t \ll w$) the demagnetizing values for the center of a wire are evaluated to be $N_x = 0$, $N_y = \frac{2t}{\pi w}$, and $N_z = 1 - \frac{2t}{\pi w}$. [Dem01]
The dipolar interaction between the stray field $\mathbf{H}_{\text{dem}}$ and the magnetic field of a magnetic moment is long ranged. It gives rise to a non-local energy contribution, as every magnetic moment interacts with the dipolar field of every other magnetic moment. In a continuum model the demagnetizing field energy is described by

$$\epsilon_{\text{dem}} = -\frac{\mu_0}{2V}\int \mathbf{M}\cdot\mathbf{H}_{\text{dem}}\, dV. \tag{2.12}$$

Anisotropy Energy

A further energy contribution depends on the direction of the magnetization $\mathbf{M}$. An uniaxial anisotropy is often observed. Its energy density is described by

$$\epsilon_{\text{uni}} = -K_{\text{uni}}(\mathbf{M}\cdot\mathbf{e_x})^2, \tag{2.13}$$

where K_{uni} is the uniaxial anisotropy constant. Uniaxial anisotropy is attributed to the sample shape and to the spin-orbit interaction. For $K_{\mathrm{uni}} > 0$ the x-axis becomes a so-called easy axis, i.e. the energy is minimal when the magnetization is collinear. For $K_{\mathrm{uni}} < 0$ the x-axis is a hard axis and the magnetization tends to align perpendicular to it.

Surface Anisotropy

Additionally to volume anisotropies, in thin films surface anisotropies become important. This effect is attributed to the reduced symmetry of the atomic environment of surface atoms. It is described using a phenomenological uniaxial perpendicular anisotropy parameter $K_\perp$ as

$$\epsilon_{\mathrm{sur}} = -\frac{K_\perp}{d}(\mathbf{M} \cdot \mathbf{e_z})^2, \tag{2.14}$$

where d is the film thickness.
Summing up the different contributions, we can now calculate the total energy density as

$$\epsilon_{\mathrm{tot}} = \epsilon_{\mathrm{ex}} + \epsilon_{\mathrm{zee}} + \epsilon_{\mathrm{dem}} + \epsilon_{\mathrm{uni}} + \epsilon_{\mathrm{sur}}. \tag{2.15}$$

We emphasize that finding the minima in Eq. 2.15 permits to determine the magnetic ground state of the magnetization. The total energy density allows us to introduce the total effective magnetic field $\mathbf{H}_{\mathrm{eff}}$. It is defined as the functional derivative of ϵ_{tot} with respect to the magnetization $\mathbf{M}$ as

$$\mathbf{H}_{\mathrm{eff}} = -\frac{1}{\mu_0}\nabla_{\mathbf{M}}\epsilon_{\mathrm{tot}} \tag{2.16}$$

For equilibrium, $\mathbf{M}$ is collinear with $\mathbf{H}_{\mathrm{eff}}$. For $\mathbf{M}$ being not parallel to $\mathbf{H}_{\mathrm{eff}}$, $\mathbf{H}_{\mathrm{eff}}$ represents the precessional axis of the magnetization.

2.3 Domains and Domain Walls

In previous sections, we have supposed that the ground state of a ferromagnetic body is the uniform magnetization. However, such a state is an equilibrium state only in sufficiently high magnetic fields, or for small enough samples, with lateral dimensions less than $\simeq 1$ μm for permalloy (for thin structures). [Chi97] For lower field values, in particular, in zero field, large enough samples split into magnetic domains. This is caused by the magnetic stray field when the sample is split into domains, and therefore the total energy is minimized. The magnetization inside the domains are approximately uniform but vary from one domain to another, so that only at the coercive field the magnetization averaged over a volume containing many domains equals to zero. The transition from the magnetization direction in a domain to a neighbouring domain occurs gradually via tilted spins, so called domain walls.

2.4 Magnetization Dynamics

As introduced in the last section the effective magnetic field $\mathbf{H}_{\text{eff}}$ determines the static equilibrium orientation of the magnetization. The dynamical model for the magnetization $\mathbf{M}$ was proposed by Landau and Lifshitz [Lan35]:

$$\frac{\partial \mathbf{M}}{\partial t} = -\gamma\mu_0 \mathbf{M} \times \mathbf{H}_{\text{eff}} + \lambda \mathbf{M} \times (\mathbf{M} \times \mathbf{H}_{\text{eff}}). \tag{2.17}$$

Here, $\gamma = g|e|/(2m_e)$ is the gyromagnetic ratio ($\gamma = 184.7 \cdot 10^9$ rad/(sT)), that couples the angular momentum $\mathbf{L}$ and the magnetic dipole moment $\tilde{\mathbf{m}} = \gamma \mathbf{L}$. e and m_e are the charge and the mass of an electron, respectively, and λ is a phenomenological damping parameter. Equation 2.17 is a torque equation of motion, resulting in a precessional motion. The most often employed equation of motion is the so-called Landau-Lifshitz-Gilbert (LLG) equation [Gil55]

$$\frac{\partial \mathbf{M}}{\partial t} = -\gamma\mu_0 \mathbf{M} \times \mathbf{H}_{\text{eff}} + \frac{\alpha}{\mathbf{M}_{\text{s}}} (\mathbf{M} \times \frac{\partial \mathbf{M}}{\partial t}), \tag{2.18}$$

where α is the phenomenological dimensionless Gilbert damping parameter with

$$\lambda = \alpha\gamma\mu_0 M_{\text{s}}.$$

This is valid for a low magnetic damping, e.g. $\alpha \simeq 10^{-2}$ for permalloy. The damping term imitates a 'viscous' damping. An important feature of the LL equation is that it ensures the conservation of the length of $\mathbf{M}$. Indeed, scalar multiplication of both sides by $\mathbf{M}$ yields $\frac{\partial}{\partial t}\mathbf{M}^2 = 0$.

2.4.1 Dynamic Susceptibility

An analytical solution of Eqn. 2.18 is not feasible in a general form. Therefore, we solve it for a special case with the following assumptions: [Bil08]

- Our sample is a thin film extended in the x-y plane, with $N_x = N_y = 0$ and $N_z = 1$.
- A homogeneous magnetic field $\mathbf{H} = H\ \mathbf{e_x}$ is applied along the x-axis yielding a uniform magnetization in the same direction.
- A small uniform excitation field $\mathbf{h} = h(\mathbf{e_y} + \mathbf{e_z})$ with $h \ll H$ is applied.
- For the dynamic component $\mathbf{m}$, $|\mathbf{m}| \ll |\mathbf{M}|$ is assumed.
- Anisotropy fields are neglected.

The harmonic excitation field sustains a harmonic precession of $\mathbf{M}$. $|\mathbf{m}| \ll |\mathbf{M}|$ allows us to decompose the magnetization into a static and a dynamic part $\mathbf{M} \simeq M_\mathrm{s}\mathbf{e_x} + m_y\mathbf{e_y} + m_z\mathbf{e_z}$. Inserting this into Eqn. 2.18 yields a set of coupled linear differential equations. The coupled set of linearized equations of motion reads

$$\begin{aligned} (\omega_H + i\alpha\omega)m_y - i\omega m_z &= \quad \omega_\mathrm{M} h_y \\ (\omega_H + i\alpha\omega + \omega_\mathrm{M})m_z + i\omega m_y &= \qquad 0, \end{aligned} \tag{2.19}$$

where $\omega_M = \gamma\mu_0 M_\mathrm{s}$, $\omega_H = \gamma\mu_0 H$. Rewriting Eqn. 2.19 in a matrix we obtain

$$\begin{pmatrix} \omega_H + i\alpha\omega & -i\omega \\ i\omega & \omega_H + \omega_\mathrm{M} + i\alpha\omega \end{pmatrix} \begin{pmatrix} m_y \\ m_z \end{pmatrix} = \begin{pmatrix} h_y \\ h_z \end{pmatrix}. \tag{2.20}$$

The complex valued high frequency or *Polder* susceptibility is defined as

$$\mathbf{m} = \hat{\chi}\mathbf{h} = (\hat{\chi'} - i\hat{\chi''})\mathbf{h}, \tag{2.21}$$

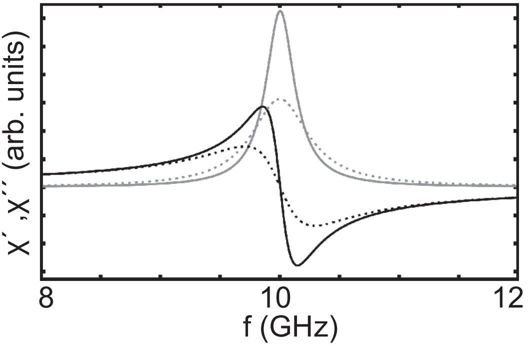

Figure 2.1: (a) Real (black) and imaginary (gray) part of the susceptibility χ_{yy} (see Eqn. 2.24) for $\alpha = 0.01$ (line) and $\alpha = 0.02$ (dotted) and the resonance frequency is $f_{\mathrm{res}} = 10.0$ GHz.

with $\hat{\chi}'$ and $\hat{\chi}''$ are the real and imaginary part of $\hat{\chi}$. Therefore, inverting the matrix in Eqn. 2.20 yields the susceptibility

$$\hat{\chi} = \frac{\omega_M}{\omega_H(\omega_{\mathrm{M}} + \omega_H) - \omega^2 + i\omega\alpha(\omega_{\mathrm{M}} + 2\omega_H)} \cdot \cdot \begin{pmatrix} \omega_H + \omega_{\mathrm{M}} + i\alpha\omega & i\omega \\ -i\omega & \omega_H + i\alpha\omega \end{pmatrix}. \tag{2.22}$$

Equation 2.22 exhibits an extremal value if the denominator equals zero. This is interpreted as a resonance of the uniform precessing magnetization. Thus, we obtain the field dependent resonance frequency by

$$\omega_{\mathrm{res}}^2 = \omega_H(\omega_{\mathrm{M}} + \omega_H) = \gamma^2\mu_0^2 H \cdot (H + M_{\mathrm{s}}) \tag{2.23}$$

The manual evaluation of the single tensor components is cumbersome, however possible to solve by the programm *Mathematica*. The complex components $\chi'_{yy} - i\chi''_{yy}$ are

$$\begin{aligned} \chi'_{yy} &= \frac{\omega_M(\omega_H+\omega_{\mathrm{M}})(\omega_{\mathrm{res}}^2-\omega^2)}{(\omega_{\mathrm{res}}^2-\omega^2)^2+\alpha^2\omega^2(2\omega_H+\omega_{\mathrm{M}})^2} \\ \chi''_{yy} &= \frac{\alpha\omega\omega_M[\omega^2+(\omega_{\mathrm{M}}+\omega_H)^2]}{(\omega_{\mathrm{res}}^2-\omega^2)^2+\alpha^2\omega^2(2\omega_H+\omega_{\mathrm{M}})^2}. \end{aligned} \tag{2.24}$$

Correspondingly, the other components are listed:

$$\begin{aligned}\chi'_{yz} = & -\chi'_{zy} = \frac{\alpha\omega\omega_M(\omega_\mathrm{M}+2\omega_H)^2}{(\omega_\mathrm{res}^2-\omega^2)^2+\alpha^2\omega^2(2\omega_H+\omega_\mathrm{M})^2}\\ \chi''_{yz} = & -\chi''_{zy} = \frac{\omega\omega_M(\omega_\mathrm{res}^2-\omega^2)}{(\omega_\mathrm{res}^2-\omega^2)^2+\alpha^2\omega^2(2\omega_H+\omega_\mathrm{M})^2}.\end{aligned} \tag{2.25}$$

$$\begin{aligned}\chi'_{zz} = & \frac{\omega_M\omega_H(\omega_\mathrm{res}^2-\omega^2)}{(\omega_\mathrm{res}^2-\omega^2)^2+\alpha^2\omega^2(2\omega_H+\omega_\mathrm{M})^2}\\ \chi''_{zz} = & \frac{\alpha\omega\omega_M(\omega^2+\omega_H^2)}{(\omega_\mathrm{res}^2-\omega^2)^2+\alpha^2\omega^2(2\omega_H+\omega_\mathrm{M})^2}.\end{aligned} \tag{2.26}$$

This allows to examine the ellipticity of the forced precession for $\mathbf{h} = h\mathbf{e_y}$. We compare the maxima of m_y and m_z which corresponds to

$$\frac{\max[\mathrm{m_y(t)}]}{\max[\mathrm{m_z(t)}]} = \frac{\max[\mathrm{Re(m_ye^{i\omega t})}]}{\max[\mathrm{Re(m_ze^{i\omega t})}]} = \frac{|m_y|}{|m_z|} = \frac{|\chi_{yy}|}{|\chi_{zy}|} \simeq \frac{\omega_H + \omega_\mathrm{M}}{\omega}. \tag{2.27}$$

In resonance the out-of-plane component is much smaller than the in-plane component.
The resonant behavior in Eqn. 2.24 of the magnetization $\mathbf{M}$ is called ferromagnetic resonance (FMR) and described by a resonance frequency ω_res and a linewidth $\Delta\omega$. The line shape is approximated by a Lorentzian function. For $\omega \simeq \omega_\mathrm{res}$ we approximate $\omega_\mathrm{res}^2 - \omega^2 = (\omega_\mathrm{res} + \omega)(\omega_\mathrm{res} - \omega) \simeq 2\omega_0(\omega_\mathrm{res} - \omega)$. We define $\Delta\omega = \alpha\omega_M$. The linewidth $\Delta\omega = 2\pi\Delta f$ is equal to the full width at half maximum. Therefore, the susceptibility χ''_{yy} can be written as

$$\chi''_{yy} \simeq K\frac{\Delta\omega}{4\cdot(\omega_\mathrm{res} - \omega)^2 + \Delta\omega^2}, \tag{2.28}$$

where K is a constant value. This approximation is valid if $\Delta\omega \ll \omega_\mathrm{res}$.

2.4.2 Kittel equation

For the general case the demagnetizing field of ferromagnetic body is described by Eqn. 2.10. Introducing this into the susceptibility $\hat{\chi}$ Eqn. 2.23 transforms to

$$f_\mathrm{res} = \frac{1}{2\pi}\gamma\mu_0\sqrt{[H + (N_y - N_x)M_\mathrm{s}][H + (N_z - N_x)M_\mathrm{s}]} \tag{2.29}$$

This equation is called Kittel formula and describes the field dependence of the resonance frequency of an arbitrary ferromagnetic body. [Kit48] In this form homogeneously magnetized ferromagnetic structures are described.

2.4.3 Eigenoscillations

In section 2.4 Eqn. 2.18 was solved with a harmonic excitation field. We now use a step function as excitation field $\mathbf{h} = \mathbf{h_0}\Theta(t - t_0)$ where $\Theta(t - t_0)$ is the Heaviside step function. We define $M_y = M_\mathrm{s}\tilde{\Phi}(t)$. At $t = t_0$ the field step shifts the magnetization from the equilibrium position to $\tilde{\Phi}_0$. To analyze the response we rewrite the Landau-Lifshitz equation to [Sil99]

$$\frac{d^2\tilde{\Phi}}{dt^2} + \lambda\frac{d\tilde{\Phi}}{dt} + \mu_0\gamma^2\frac{\partial\epsilon_\mathrm{tot}}{\partial\tilde{\Phi}} = 0. \tag{2.30}$$

By a Taylor expansion the last term is transformed to

$$\frac{\partial\epsilon_\mathrm{tot}}{\partial\tilde{\Phi}} \rightarrow \frac{\partial^2\epsilon_\mathrm{tot}}{\partial\tilde{\Phi}^2}[\tilde{\Phi} - \tilde{\Phi}_0\Theta(t - t_0)].$$

The solution is a damped, harmonic oscillation of the magnetization

$$M_y \propto \beta_0 e^{-t/\tau_0}\sin(\omega_0 t + \tilde{\Phi}_0), \tag{2.31}$$

with an eigenfrequency ω_0 and the intrinsic relaxation time τ_0. The resonance frequency ω_res obtained for a forced oscillation is related to the eigenfrequency by

$$\omega_\mathrm{res}^2 = \omega_0^2 - (\lambda/2)^2. \tag{2.32}$$

The intrinsic relaxation time τ_0 is connected to the forced oscillation by [Sil99]

$$\tau_0 = \frac{2}{\lambda} = \frac{2}{\Delta\omega}. \tag{2.33}$$

2.4.4 Spin Waves in Thin Films

In the preceding sections we discussed uniform magnetization motion, i.e. the excitation field is uniform and all magnetic moments are in phase. This can be described as a uniform precession with infinite wavelength. In the following we provide the general formalism for spin waves in a thin film of thickness d. The calculation has been done by Kalinikos and Slavin. [Kal86] Let the wave vector $\mathbf{k}$ consist of an in plane component k_ζ and an out-of-plane component k_p. The in plane component is decomposed in a component parallel to the magnetic field, i.e. $k_{||}$, and a perpendicular component $k_\perp$ by ${k_\zeta}^2 = k_{||}^2 + k_\perp^2$. k is given by $k^2 = k_\zeta^2 + k_p^2$, and

$$k_p = \frac{p\pi}{d}, p = 0, 1, 2...$$

The dispersion relation of spin waves without damping is given by

$$\omega_{\text{res}}^2(k, H)|_p = (\omega_H + A_{\text{ex}}\omega_M k^2)[\omega_H + \omega_M(A_{\text{ex}}k^2 + F_{pp}(k_p))], \quad (2.34)$$

where $F_{pp}(k_p)$ is the dipolar matrix element. In the case of *exchange spin waves* the exchange term $A_{\text{ex}}k^2$ becomes large when compared to unity. In contrast, when $A_{\text{ex}}k^2 \ll 1$, the excitations are called *dipolar spin waves* or *magnetostatic waves.* The dipolar interaction causes a deviation from a quadratic dispersion relation. $F_{pp}(k_p)$ is given by

$$F_{pp}(k_p) = 1 - P_{pp}cos\vartheta^2 + \omega_M \frac{P_{pp}(1 - P_{pp})\sin\vartheta^2}{\omega_H + A_{\text{ex}}\omega_M k^2}, \quad (2.35)$$

where ϑ is the angle between propagating spin wave and the magnetization M. Then

$$P_{pp} = \frac{{k_\zeta}^2}{k_p^2} + \frac{2{k_\zeta}^3}{dk_p^4}\frac{1}{1 + \delta_{0p}}[1 - (-1)^p \exp(-k_\zeta d)]. \quad (2.36)$$

In the following we discuss Eqn. 2.34 for special geometries. [Sta09]

For the case of magnetostatic waves the exchange interaction can be neglected. In the Damon-Eshbach geometry [Dam61] ($M \perp k$) the spin wave dispersion is given by

$$\omega_{DE}^2 = \omega_H(\omega_H + \omega_{\text{M}}) + \frac{\omega_{\text{M}}^2}{4}(1 - e^{-k_\perp d}). \quad (2.37)$$

The phase velocity (ω/k) and group velocity (see Eqn. 2.41) have the same sign. Thus, this so called Damon-Eshbach wave (DE) or

magnetostatic surface wave is a forward wave.
The dispersion relation of the magnetostatic backward volume wave (MSBVW)

$$\omega_{MSBVW}^2 = \omega_H[\omega_H + \omega_\mathrm{M}(\frac{1-e^{-k_{||}d}}{k_{||}d})]. \tag{2.38}$$

In Fig. 2.2 (a) the dispersion relations of DE waves and MSBVWs are depicted. The field dependence of DE waves and MSBVWs coincide for $k \rightarrow 0$, where we yield Eqn. 2.29.
For the magnetic field pointing perpendicular to the thin film the magnetostatic forward volume wave (MSFVW) dispersion follows as

$$\omega_{MSFVW}^2 = \omega_H[\omega_H + \omega_\mathrm{M}(1 - \frac{1-e^{-k_\zeta d}}{k_\zeta d})]. \tag{2.39}$$

We emphasize, that in this case the spin wave propagation does not depend on the direction of the in-plane wave vector $\mathbf{k}_\zeta$.
The field dependence of the MSFVW for $k \rightarrow 0$ has to consider the intrinsic energetic contribution of the thin film demagnetization. Two regions are distinguished, the first for $H \geq M_\mathrm{s}$, which yields

$$\omega_{MSFVW} = \omega_H = \mu_0\gamma(H - M_\mathrm{s}). \tag{2.40}$$

For small fields $H < M_\mathrm{s}$ the field dependence is dominated by the non-saturated magnetic ground state, which changes continuously with the applied field H. The minimum frequency is obtained for $H = M_\mathrm{s}$, where the applied field equals the demagnetizing field of the thin film.
The group velocity v_g is defined by

$$v_g = \frac{\partial\omega}{\partial k}. \tag{2.41}$$

In Fig. 2.2 (b) the group velocities of DE and MSBVW are depicted. The group velocity of DE has values in the order of 10^4 m/s for typical material parameters used in this thesis. Note, that the group velocity of the MSBVW is negative for small k. The group velocity of the MSFVW is given by $v_g|_{p=0} = \frac{\omega_M d}{4} \propto M_\mathrm{s}$. For propagating spin waves we can define the relaxation length

$$s_r = v_g\tau_0. \tag{2.42}$$

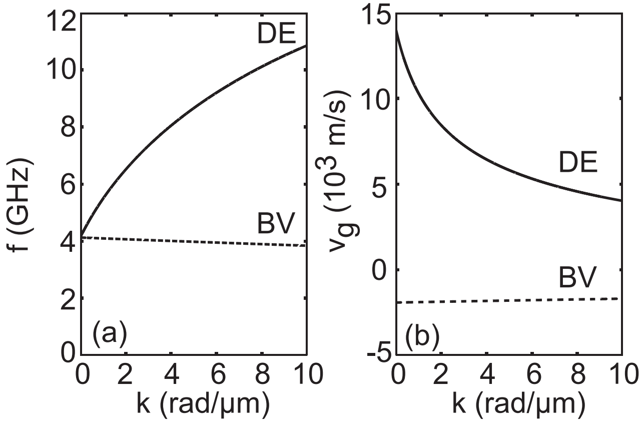

Figure 2.2: (a) Dispersion of DE wave (solid line) and MSBVW (dashed line). The peculiar behavior of the MSBVW, i.e. the negative slope, is observed. (b) The group velocity of DE wave (solid) and MSBVW (dashed) is shown. DE waves (MSBVWs) show a group velocity of the order 10^4 m/s (-10^2 m/s). The magnetic parameters of both graphs are $\mu_0 M_\mathrm{s} = 1.05$ T, $\mu_0 H = 20$ mT, $d = 30$ nm. The field is applied in-plane.

For several applications it is desirable to have a high relaxation length (Eqn. 2.42). Thus, taking the definition of the group velocity for MSFVW a material with high M_s is necessary.

2.5 Plane Wave Method

Plane wave method (PWM) is a powerful technique to solve band structures (dispersion relations) of periodically patterned structures, e.g. magnonic crystals. [Vas96, Kra08] Additionally, PWM is capable of providing spin wave excitation profiles. Theoretical results presented in this thesis which are based on the PWM are performed by Dr. M. Krawczyk at Adam Mickiewicz University in Poznán, Poland. The PWM is applied for a one-dimensional array of nanowires. The method is described in [Sok11]. For PWM initially the demagnetizing field H_{dem} is determined. Then Eqn. 2.18 with H_{eff} containing external, exchange and demagnetization fields is solved. The Bloch ansatz considers

$$\mathbf{m}(x,t) = \sum_{G} \mathbf{m}_{\mathbf{k}}(\mathbf{G}) exp[i((\mathbf{k}+\mathbf{G})x - \omega t)]$$

where $\mathbf{G}$ is a reciprocal lattice vector defined by periodic patterning of the ferromagnet. The underlying Landau-Lifshitz equation contains the relevant magnetostatic and dynamic coupling fields. PWM provides dispersion relations and excitation profiles of spin waves.

2.6 Micromagnetic Simulation

We use micromagnetic simulations (MS) to analyze the experimental resonance spectra and interpret the data. By micromagnetic simulations using the software MicroMagus [Ber08] we obtain the ferromagnetic ground state and the dynamic magnetic properties of patterned ferromagnets. For the simulations the ferromagnetic structure is subdivided into a mesh of N rectangular cells. Each individual cell i, with $i = 1...N$, in the grid possesses a uniform magnetization $\mathbf{M_i}$ and is in subject to the effective magnetic field $H_{\mathrm{eff,i}}$. The effective magnetic field $H_{\mathrm{eff,i}} = \frac{1}{\mu_0}\frac{\partial \epsilon_{\mathrm{tot}}}{\partial \mathbf{M_i}}$ contains internal contributions, e.g. from anisotropy, and external contributions, such as exchange and dipolar magnetic fields from neighbours.

2.6.1 Magnetostatic Configuration

For each cell, the total energy, see Eqn. 2.15, is minimized to obtain the static magnetic configuration by integrating the LLG equation 2.18 given by

$$\frac{\partial \mathbf{M_i}}{\partial t} = -\gamma\mu_0 \mathbf{M_i} \times \mathbf{H}_{\mathrm{eff,i}} + \frac{\alpha}{\mathbf{M}_{\mathrm{s}}}(\mathbf{M_i} \times \frac{\partial \mathbf{M_i}}{\partial t}) \qquad (2.43)$$

and calculating the integral torque. If the integral torque is lower than a certain threshold value the equilibrium position is reached. The total energy of Eqn. 2.15 is minimum when $M_i \parallel H_{\mathrm{eff,i}}$.

2.6.2 Magnetodynamic Behavior

For dynamic magnetization behavior the static magnetic configuration obtained in Sec. 2.6.1 is used as a starting configuration. Then the magnetization of L ($L \leq N$) cells is disturbed by a magnetic field pulse with Gaussian shape of 0.1 ns full length. After the initial field pulse the magnetization relaxes towards the equilibrium position. There are ringing, i.e. spin precessional motion, and damping involved. The relaxation of the magnetization $\mathbf{M_i}(\mathbf{r}, t)$ is simulated in discrete time steps Δt of a few ps. The uneven temporal spacing of the data causes the usage of a least-squares spectral analysis (Lomb method) to calculate the frequency spectrum $P(f, \mathbf{r})$. Typically the out-of-plane compoment of $\sum_i M_{i,z}$ is used for the spectral analysis (if not denoted differently).

In general, two different simulation geometries have been used. In order to simulate $k = 0$ all cells $L = N$ are uniformly excited by the field pulse. In this case only a few unit cells of a periodic magnetic structure are simulated. We employ periodic boundary conditions in two dimensions. This imitates an infinite wavelength and therefore leads to a simulation of the ferromagnetic resonance. For the typically applied damping of $\alpha = 0.01$ a simulation duration of 6 ns is sufficient. The results of such simulations is the eigenmode spectrum, which we compare to the experimental data. Additionally, the spatial mode profile $P(f, x, y)$ is provided which gives further physical insight. The second simulation geometry is used in order to simulate spin waves with $k \neq 0$. A structure of several tens or hundreds of alligned unit cells (w.l.o.g. in the x direction) are discretized. A small area of a few cells $L \ll N$ and with a width in x direction of 2.5 pixels is excited. There, a Gaussian field pulse is applied. A two-dimensional, i.e. spatio-temporal, Fast Fourier transformation is performed to obtain the spectral response $P(f, k)$. In this manner propagating spin waves and dispersion relations are simulated. [Neu11a]

3 Experimental Setup and Techniques

In this chapter the experimental setups and techniques are introduced. We discuss three types of all electrical broadband resonance spectroscopy. Additonally we present anisotropic magnetoresistance measurements, and the sample designs.

3.1 All Electrical Spin Wave Spectroscopy

3.1.1 Experimental Setup

The broadband measurement setup comprises the following elements, see also Fig. 3.1:

1. (a) A vector network analyzer (VNA) PNA-X N-5242A (with two) or PNA N-5222A (with four ports) from Agilent providing a continuous microwave with frequency f from 10 MHz to 26.5 GHz. The VNA provides an electromagnetic wave voltage signal with f at a given port. All ports are measuring at the same frequency f. All ports can act as a source. The output power is typically -5 dBm. The VNA allows frequency resolved measurements with a high sensitivity.
   (b) A digital sampling analyzer DSA 8200 from Tektronix with a module for time-domain reflectometry (TDR). The TDR applies a voltage step pulse from 10% to 90% maximum voltage with a short rise time of 11.7 ps to one CPW. The step pulse has a maximum voltage of 500 mV. The TDR allows time-resolved measurements with a picosecond resolution. TDR is a stroboscopic technique.

2. Contact is established between both ports of the measurement device and the device under test (DUT) using microwave cables and high frequency tips (microprobes). Microprobes provide

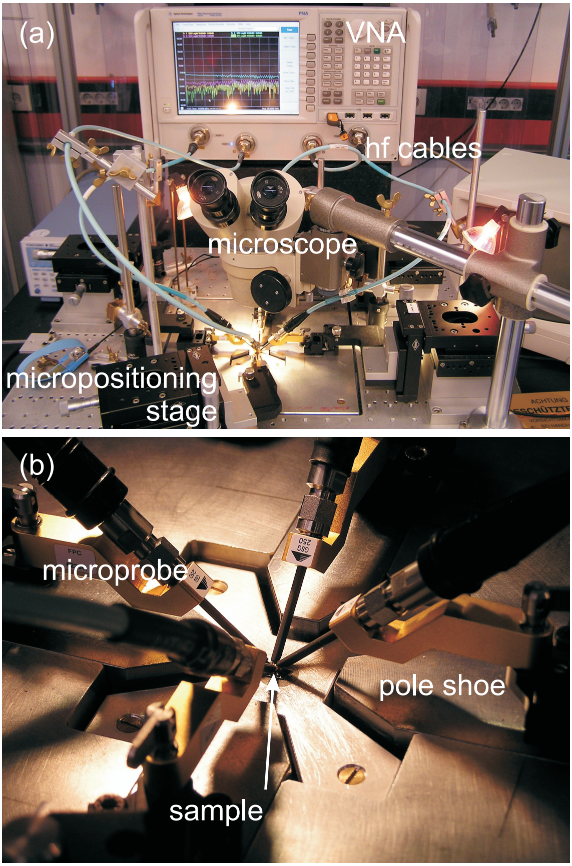

Figure 3.1: Photograph of the experimental setup for all electrical spectroscopy. (a) A VNA (4-port) provides a high frequency wave and is connected to coaxial cables. The micropositioning allows an exact approach of the microprobes onto the sample viewed by the microscope. The experimental setup is located on a shock absorbing table. (b) Surrounding area of the sample. Four microprobes are contacting the sample. Two pairs of pole shoes supply the vector magnetic field.

impedance-matched high frequency contacts. It is important to avoid mechanical motion during the measurements.

3. (a) An in-plane magnetic field **H**, with $|\mu_0 H| \leq 120$ mT can be generated. The magnetic field coils are orientated perpendicular with respect to each other, allowing a magnetic field of arbitrary in-plane direction η to be generated. The bipolar power sources allow, both, continuous sweeps and a fixed current output.
   (b) An out-of-plane magnetic field **H**, with $\mu_0 H \leq 2.5$ T can be generated. Also the temperature may be controlled from 4 K to 400 K.

4. Hall sensors allow an absolute measurement of the magnetic field **H**. They are positioned in close vicinity to the specimen. The Hall sensor bias currents are modulated. Hall voltages are read out using a lock-in detector for an increased signal-to-noise ratio.

5. A computer software programm allows the control of the measurement device and the magnetic field coils. Data acquisition is fully automated. A feedback circuit using the Hall sensor voltage as a set point controls the current through the magnetic field coils to stabilize **H** at the present value.

6. Setup for shielding off environmental noise comprising a shock absorbing table to suppress vibrations and a laminar flow box with soft-PVC curtains to suppress dust and air draft.

3.1.2 Scattering Parameters

Scattering parameters are powerful tools for the analysis and design of high frequency devices. [Mav96] An electrical circuit is characterized in terms of high frequency electromagnetic wave scattering by a set of S-parameters as sketched in Fig. 3.2.

$$\begin{pmatrix} b_1 \\ b_2 \end{pmatrix} = \begin{pmatrix} S_{11} & S_{12} \\ S_{21} & S_{22} \end{pmatrix} \begin{pmatrix} a_1 \\ a_2 \end{pmatrix}. \tag{3.1}$$

The parameter a_i represents the incident power-wave amplitude at port i, and b_j represents the reflected power-wave amplitude at port j

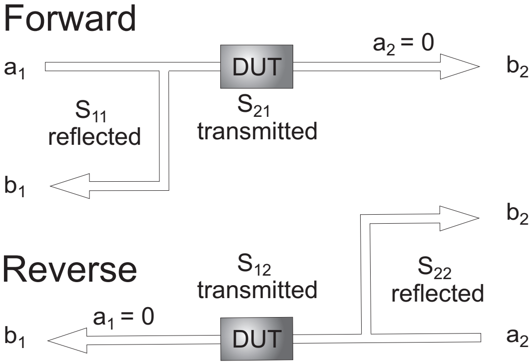

Figure 3.2: Scheme of the S-parameters of an electrical 2 port circuit with a device under test (DUT). The parameter a_i (i is the port number) indicates the emitting port, and b_i the detecting ports. S_{ij} is the measured S-parameter for emission at port j and detection at port i. A forward (emission at port 1) and a backward (emission at port 2) geometry is possible.

$(i, j = 0, 1)$. A VNA measures a set of S-parameters, which is a ratio of reflected amplitude and incident amplitude of a wave as described in Eqn. 3.1. S-parameters are complex numbers and described by magnitude $Mag(S_{ij})$ and phase $\Phi(S_{ij})$, or $\Re(S_{ij})$ and $\Im(S_{ij})$. For a 2-port geometry there are two parameters, S_{11} and S_{22}, characterizing the reflected wave measured at port 1, respectively port 2. And there are two further parameters, which are attributed to the transmission of the electromagnetic signal. These are denoted S_{21} (S_{12}), and describe the forward (backward) transmission from port 1 to port 2 (from port 2 to port 1).

3.1.3 Calibration of Vector Network Analyzer

Network analysis, i.e., the measurement of S-parameters of a DUT, is concerned with the accurate measurement of the ratios of reflected to the incident signal, and the transmitted signal to the incident signal. Each VNA can be separated into an ideal vector network analyzer and an error network. In this error network the corresponding parameters are called error terms. The primary goal of a calibration is the correction of system errors. Any remaining errors depend on the accuracy of the error terms and the repeatability of the measurement process. By the calibration process the error terms are determined. A test system consisting of a VNA, cables, and calibration standards is required. These calibration standards are one-port and two-port networks where the characteristics are known. The characteristics of the calibrations standards (also with the deviations from ideality) is provided to the VNA.

There are three basic sources of measurement errors: systematic, drift, and random errors. Systematic errors are caused by imperfections in the measurement setup. They are time invariant and repeatable. Systematic errors are identified by the calibration process and are then mathematically removed in the measurements. Drift errors are based on a changing performance of the measurement setup after the calibration. Drift is typically induced by temperature variations. A further calibration can handle the drift error. In a stable ambient temperature, provided in our laboratories, a calibration is stable for a long time. Random errors cannot be predicted as they randomly

vary with time. Thus, an elimination of random errors is not possible by calibration. The main contributors are the source phase noise, the sampler noise, and the intermediate frequency (IF) noise.
To eliminate all systematic errors a calibration is needed which applies a 2-port vector-error correction. This vector-error correction requires several calibration standards. We use open, short, load, and through calibration standards on a calibration substrate for microwave tips. This method is known as 2-port SOLT (short-open-load-through) technique. [Agi04] The definition of the calibration standards is summarized in a file stored on the VNA, i.e., the cal-kit definition. A calibration of the measurement setup is indispensable, e.g. it provides a stable phase relationship between the ports of the VNA. [Agi04] For the calibration of the 4-port VNA each port has to be calibrated with the three remaining ones, therefore six calibration processes are needed.

3.1.4 Coplanar Waveguide Design

A coplanar waveguide (CPW) is a metallic device structure for guiding a high frequency electromagnetic wave on a substrate. [Sim01] It consists of three parallel electrically conducting lines on top of a insulating substrate. The outer conductors (OCs) are denoted as the ground lines with width w_{OC}, the inner conductor (IC) in between the ground lines is denoted as signal line with a width w_{IC}, see Fig. 3.3. The gap width s_C separates outer and inner conductors. In this thesis the CPWs are made from 5 nm thick Cr and 120-200 nm thick Au by optical lithography, see Sec. 4.1, or electron beam lithography, see Sec. 4.2. Electron beam lithography is employed to position the CPWs with an high accuracy of tens of nanometers. The CPWs comprise (i) two pad regions, where high frequency tips provide contact to cables, (ii) a taper region to feed the electromagnetic wave to the (iii) excitation region with micrometer-sized dimensions, where the spin waves are excited in a ferromagnetic sample. The pad region is customized on the dimensions of the high frequency tips. The excitation region of the CPW is tailored for an optimum spin-precessional motion at a defined spin wave vector k. In Fig. 3.3 we define the x, y, and z direction.
In good approximation a transversal electromagnetic wave propa-

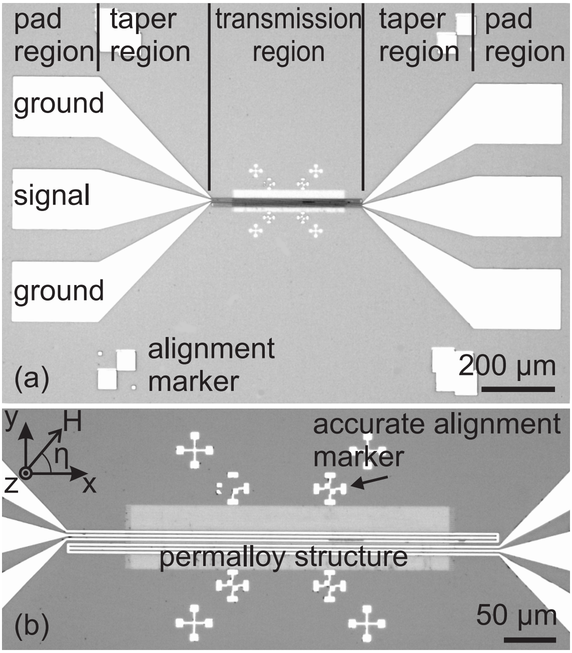

Figure 3.3: Optical photo of a typical sample. (a) CPW with pad region, taper region, and transmission region on top of a permalloy structure is shown. The two ground lines and the signal line are denoted. Marker are implemented for a coarse alignment. (b) The transmission region of two CPWs is positioned on top of a permalloy structure. Small markers allow an accurate alignment.

gates along the CPW. For an optimized CPW the high frequency impedance $Z_c = \sqrt{\frac{L}{C}}$ of the CPWs is tailored to $Z_c = 50\ \Omega$. Here $L = \mu_0/4\tilde{f}(s_{\mathrm{C}}, w_{IC})$ and $C = 4\tilde{\epsilon}/f(s_{\mathrm{C}}, w_{IC})$, where $f(s, w_{IC})$ is an involved function depending on s_{C} and w_{IC}, and $\tilde{\epsilon}$ is the effective permittivity. We then obtain [Wan90]

$$Z_c = 1/4\sqrt{\frac{\mu_0}{\tilde{\epsilon}}}\tilde{f}(s_{\mathrm{C}}, w_{IC}). \tag{3.2}$$

Scattering of propagating electromagnetic waves occurs at a discontinuity of impedance described by the high frequency scattering parameter $\Gamma_Z = \frac{Z_1 - Z_c}{Z_1 + Z_c}$, where Z_1 is the impedance of the discontinuity. The impedance Z of a CPW is given by Eqn. 3.2. If the substrate material is ferromagnetic Eqn. 3.2 is transformed by $\mu_0 \rightarrow \tilde{\mu}$, where $\tilde{\mu}$ is the effective permeability:

$$Z_c = 1/4\sqrt{\frac{\tilde{\mu}}{\tilde{\epsilon}}}\tilde{f}(s_{\mathrm{C}}, w_{IC}) \tag{3.3}$$

As $\hat{\mu}$ varies in the resonance case a scattering of the electromagnetic wave occurs. For a more detailed analysis of the measurement technique focusing on the high frequency properties of the measurement the reader is referred to [Bil08].

3.1.5 Signal Generation and Detection

The VNA injects a microwave current $i(f)$ into a CPW that generates a high frequency field $\mathbf{h}^{\mathrm{rf}}(y, f)$ that encircles the conductor lines according to Biot-Savart's law. This high frequency field excites spin-precessional motion in the magnetic material [c.f. Sec. 2.4.1]. A precessing magnetization causes a magnetic flux Φ_M in the CPW that induces a voltage. Following [Gie05, Neu11a] the magnetic flux in a CPW is given by the magnetization $\mathbf{M}$ and the dynamic magnetic field $\mathbf{h}^{\mathrm{rf}}$

$$\Phi_M = \mu_0 \int_{V_S} \frac{\mathbf{h}^{\mathbf{rf}}}{I} \cdot \mathbf{M} dV. \tag{3.4}$$

V_S is the sample volume, and I is the current in the CPW. The magnetic field $\mathbf{h}^{\mathrm{rf}}$ is oriented perpendicular to the CPW and simplified in that it only contains in-plane contributions $\xi(y)$. $\mathbf{h}^{\mathrm{rf}}$ exhibits a spatial distribution $\xi(y)$ with $\int dy\xi(y) = \Xi$. In general Eqn. 3.4 can be rewritten

$$\Phi_M = \frac{\mu_0 dl \sin\iota}{w\Xi} \int \xi(y) \cdot M_y(y,t)dy, \tag{3.5}$$

where ι is the angle between $\mathbf{M}$ and the x-axis, l is the length of the conductor. The induced voltage is then given by

$$\begin{aligned} V_{\mathrm{ind}} &= -\frac{d\Phi_M}{dt} = \\ &= -C\int \xi(y) \cdot \frac{dM_y(y,t)}{dt}dy = \\ &= -C\int \xi(y) \cdot \chi_{\mathrm{yy}}\frac{dh(y,t)}{dt}dy. \end{aligned}$$

Here χ_{yy} is the susceptibility. We can rewrite the integration in the reciprocal space

$$V_{\mathrm{ind}} = -C'\int \rho(k) \cdot \chi_{\mathrm{yy}}(k)h(k,\omega)dk, \tag{3.6}$$

where $\rho(k)$ is the spin wave excitation distribution. The time derivative is evaluated for harmonic excitation $\frac{dh(t)}{dt} = -i\omega h(\omega)$. Furthermore, for harmonic excitations $\rho(k) = h(k)$. Then the measured signal a_{ii} that is proportional to V_{ind} consists of the susceptibilities of all excited spin waves [Vla10]

$$a_{ii}(\omega) \propto \int \chi(\omega,k)\rho(k)^2 dk, \tag{3.7}$$

where a_{ii} is the measured relative self inductance of a CPW. Spin waves that propagate over a distance y acquire a phase and are attenuated. This is included by an exponential term with a complex wave vector

$$a_{ji}(\omega) \propto \int \chi(\omega,k)\rho(k)^2 exp(-iky)dk. \tag{3.8}$$

a_{ji} is the measured relative mutual inductance of two CPWs, where CPW i acts as emitter and CPW j acts as detector. The induced voltage changes the impedance matrix Z_{ij} of the CPW and according to the $S_{ij} \longleftrightarrow Z_{ij}$ relationship [And97] also the S-parameters matrix.

3.1.6 CPW Excitation Spectrum

Due to the spatial variation of the excitation field $\xi(y)$ a CPW excites spin waves with a wave vector distribution $\rho(k)$. The currents in the outer conductors flow in opposite direction to the current in the inner conductor. Thus, the in plane excitation field h_y^{rf} varies spatially. It can be shown, that the Fourier transformation of the microwave current density $\xi(y)$ directly yields the wave vector distribution $\rho(k)$. [Vla10] The normalized current density is in good approximation given by $h_y^{\mathrm{rf}}(OC)/h_0 = -0.5$ and $h_y^{\mathrm{rf}}(IC)/h_0 = 1$, normalized on the maximum field value h_0. The Fourier transform provides the wave vector distribution $\rho(k) \propto FFT(h_y^{\mathrm{rf}})$. The finite width of excited wave vectors adds a further contribution to the intrinsic linewidth $\Delta\omega$ derived in Sec. 2.4.1. This contribution represents the inhomogeneous broadening $\Delta\omega_{\mathrm{ib}}$. In Fig. 3.4 (a) numerically obtained results from Eqn. 3.7 are depicted for the case of a plain film with $M_{\mathrm{s}} = 820$ kA/m, $\alpha = 0.005$, and $\Delta k = 0.5$ rad/μm. We use the described $\rho(k)$, and $\chi(\omega, k)$ is constructed by the dispersion relation and a Lorentzian line shape for each wave vector with an intrinsic linewidth

$$\Delta\omega = 2\alpha\omega + \Delta\omega_{\mathrm{ex}}. \tag{3.9}$$

Here $2\alpha\omega$ are frequency dependent losses from Eqn. 2.18, which describes a 'frictional' damping (see. Eqn. (1.75) in [Gur96]), and $\Delta\omega_{\mathrm{ex}}$ is a damping contribution that addresses different scattering effects of spin waves. Three simulated intrinsic resonances (black) at different excited wave vectors k and the effective resonance (blue) are shown. Equation 3.7 yields then a modified resonance behavior which exhibits an effective linewidth $\Delta\omega_{\mathrm{eff}}$. A valid approximation is [Vla10]

$$\Delta\omega_{\mathrm{eff}} \simeq \Delta\omega + v_{\mathrm{g}}\Delta k. \tag{3.10}$$

$\Delta\omega_{\mathrm{eff}}$ contains direct and indirect contributions to the damping. [Bab08, Bab11, Sta09, Ari99, Fae11]

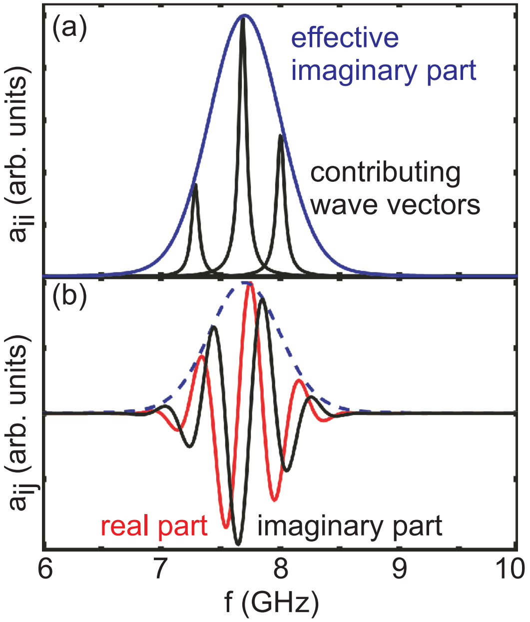

Figure 3.4: (a) The effective absolute amplitude $Mag(a_{ii})$ (blue) obtained by numerically solving Eqn. 3.7 comprises intrinsic resonances for each frequency f (black). The sketched intrinsic resonances illustrate the contributing wave vectors (transformed to frequency scale). (b) For propagating spin waves an acquired phase Φ, see Eqn. 3.8, yields an oscillating behavior of $\Im(a_{ij})$ and $\Re(a_{ij})$. The data is also obtained numerically. The dashed line symbolizes the excitation from (a). The parameter was $\alpha = 0.005$ and the excitation width $\Delta k = 0.5$ rad/μm.

Let us discuss the valid parameter regime of this approximation by focusing on the specific limiting cases. For $v_g \Delta k \ll \Delta\omega$ the measured linewidth is dominated by the intrinsic contribution. This is the case for typical VNA-FMR measurements with 20 μm wide CPWs, where $k \simeq 0$. Here a Lorentzian-type curve is detected, which is caused by the intrinsic contribution. In contrast, if $v_g \Delta k \gg \Delta\omega$, the contribution due to the intrinsic damping is vanishingly small and the measured signal is dominated by the inhomogeneous broadening. In this work, we assume a Gaussian wave vector distribution $\rho(k)$ for the used CPWs (see Fig. 3.5), furthermore, the ratio $(2/\tau)/(v_\mathrm{g}\Delta k_\mathrm{CPW}) \simeq 1$, then the SW resonance is a convolution of Gaussian- and Lorentzian-type curve. Correspondingly, in Fig. 3.4 (a) results from Eqn. 3.8 are numerically solved also for the case of a plain film. The oscillatory behavior is based on the acquired phase shift. Real and imaginary part are additionally phase shifted by 90° to each other.

3.2 Methodics of Measurement

3.2.1 Vector Network Analyzer Ferromagnetic Resonance

Vector Network Analyzer Ferromagnetic Resonance (VNA-FMR) is a technique to investigate FMR over the full frequency spectrum. [Kua02, Cou04, Gie05, Bil08] For VNA-FMR a 9 mm long CPW with a inner conductor width $w_\mathrm{IC} = 20$ μm and an edge-to-edge separation of 10 μm is connected to a VNA. The investigated sample with ferromagnetic material is positioned face-down (so called flipchip geometry) onto the CPW. A connected VNA acquires the S-parameter S_{21} as a function of frequency f and applied field $\mathbf{H}$. The technique is continuous wave experiment. For a given magnetic field H and angle η of the external magnetic field a spectrum $S_{21}(Meas)$ is measured. Following Eqn. 3.6 the scattering of electromagnetic waves changes when resonant spin precession takes place. We subtract a reference spectrum $S_{21}(Ref)$ without resonance[1] to obtain $a_{21} = S_{21}(Meas) - S_{21}(Ref)$ and to increase the signal-to-noise ratio. a_{21} is a measure of the total susceptibility χ, see Sec. 3.1.5.

---

[1] Typically $S_{21}(Ref) = S_{21}(\mu_0 H = 100\text{ mT}, \eta = 90°)$

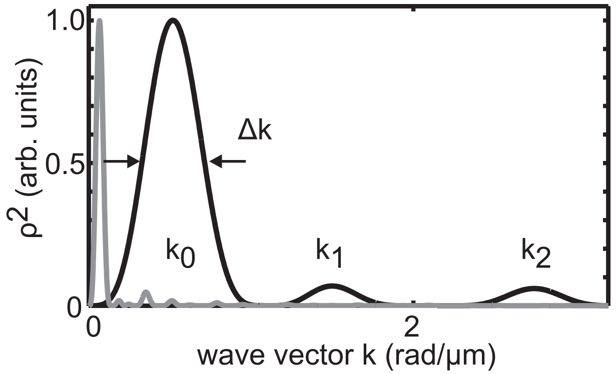

Figure 3.5: Spin wave excitation distribution $\rho(k)^2$ for a AESWS CPW (black) and a VNA-FMR CPW (gray) as described in the text. The AESWS CPW exhibits three relevant maxima at k_0, k_1, and k_2. The main peak k_0 exhibits a full-width-half-maximum Δk.

In Fig. 3.5 the excitation strength of the used CPW is shown. It exhibits a maximum at $k_0 = 5 \cdot 10^{-2}\ \frac{\text{rad}}{\mu\text{m}}$, which is close to $k = 0$. The small wavevector motivates to call the technique VNA-FMR. In Fig. 3.5 we present the wave vector distribution for a CPW used in this thesis.

3.2.2 Frequency-resolved AESWS

For frequency-resolved all electrical spin wave spectroscopy (FR-AESWS) two CPWs, see Sec. 3.4, with an inner conductor $w_{\text{IC}} = 2\ \mu$m and an gap width of 1.6 μm are connected to a VNA, as seen in Fig. 3.1. The two parallel CPWs are shorted and separated by a distance of typically 12 μm (i.e. center-to-center distance between inner conductors). The first CPW is used as an emitter, the second CPW is used as a detector. Thereby, we investigate propagating spin waves of wave vector $k \neq 0$. The wave vector distribution $\rho(k)$ with a maximum excitation strength at k_0 is calculated by a Fourier Transformation of the excitation field h_y^{rf} of the CPW, see Sec. 3.1.5. In

Fig. 3.5 we present the wave vector distribution of a AESWS CPW. The excitation width Δk is defined by the full width at half maximum value around k_0 [c.f. Fig. 3.5].

As shown in Sec. 3.2.1 we perform measurements at a given magnetic field H and angle η, where $S_{ij}(Meas)$ is acquired. We subtract a reference measurement without resonance in the measured frequency range which yields $a_{ij} = S_{ij}(Meas) - S_{ij}(Ref)$ to increase the signal-to-noise ratio, correspondingly to Sec. 3.2.1. All S-parameters S_{ij} provide complementary information and are separately evaluated. It has been shown, that also propagation analysis is possible [Bai03b, Vla10, Yu12]. a_{ii} is a measure of the susceptibility χ of the material, see Sec. 3.1.5. The transmission signal a_{ij} with $j \neq i$ contains further phase information. The relative phase Φ at the detector depends on the wave vector k and the distance y

$$\Phi = -k \cdot y. \tag{3.11}$$

Introducing this into Eqn. 2.41 yields

$$v_{\mathrm{g}} = -\frac{\partial f \cdot 2\pi}{\partial \Phi / y}. \tag{3.12}$$

For a propagating spin wave the amplitude decreases exponentially with the distance

$$a_{21} = \beta a_0 \exp^{-\frac{y}{s_{\mathrm{r}}}} \tag{3.13}$$

where β is the non-reciprocity factor [Dem09]. s_{r} is the relaxation length.

3.2.3 Time-resolved AESWS

For time-resolved all electrical spin wave spectroscopy (TR-AESWS) two CPWs from to Sec. 3.2.2 are connected to a TDR, see Sec. 3.1. The TDR applies a voltage step pulse with a short rise time of 11.7 ps to one CPW. The step pulse gives rise to a current pulse in the CPW and excites spin wave eigenmodes. The response of the electromagnetic system is measured with a high temporal resolution (0.8 ps). The measurement signal-to-noise ratio is improved by averaging 10^4 traces under the same experimental conditions. Similar to Sec. 3.1.2

the electrical circuit is defined by four parameters: we detect time dependent reflection T_{ii} and transmission T_{ji} parameters $(i, j = 1, 2)$. The characteristic electromagnetic signals T_{ii} and T_{ji} are presented in [Due09].

As shown in Sec. 3.2.1 we perform measurements at a given magnetic field H and angle η, where $t_{ij}(Meas)$ is measured. We subtract a reference data set which yields $t_{ij} = T_{ij}(Meas) - T_{ij}(Ref)$ to extract the magnetic response and increase the signal-to-noise ratio. t_{ii} contains the eigenmode signal as introduced in Sec. 2.4.3, which is described by a damped sinusoidal oscillation

$$t_{ii} \propto \exp^{-t/\tau_0} \sin \omega_0 t + \tilde{\Phi}. \tag{3.14}$$

The propagation signal t_{ij} $(i \neq j)$ is derived in [Cov02, Cov04] to be

$$\begin{aligned} t_{ij}(y,t) \propto & \frac{Ce^{-\frac{t}{\tau_0}}}{(\delta^4 + \varsigma^2 t^2)^{\frac{1}{2}}} \cdot \exp\left[\frac{-\delta^2 (y - v_g t)^2}{4(\delta^4 + \varsigma^2 t^2)}\right] \cdot \\ & \cdot \cos\left(k_0 y - \omega_0 t + \Phi\right), \end{aligned} \tag{3.15}$$

where C is a constant, $\delta = 2/\Delta k$ is the inverse excitation width of a Gaussian distribution of wave vectors, and $\varsigma = \frac{1}{2}\partial^2\omega/\partial k^2|_{k_0}$.

3.3 Anisotropic Magnetoresistance Measurement

In a ferromagnetic material the resistance depends on the relative angle $\hat{\vartheta}$ of the electrical current $\mathbf{I}$ and the magnetization $\mathbf{M}$. [Blu01, Miy12] It has been shown that a ferromagnetic material exhibits a higher electrical resistivity $\rho_{\parallel}$ when the magnetization $\mathbf{M}$ is parallel to the electrical current flow, and a lower resistivity $\rho_{\perp}$ when the magnetization $\mathbf{M}$ is perpendicular to the electrical current flow. This phenomenon is called Anisotropic Magnetoresistance (AMR). The AMR is defined as the relative change in resistivity between two configurations: AMR $= (\rho_{\parallel} - \rho_{\perp})/\rho_{\parallel}$. The reader is referred to comprehensive reviews on the subject in [Blu01, Miy12].

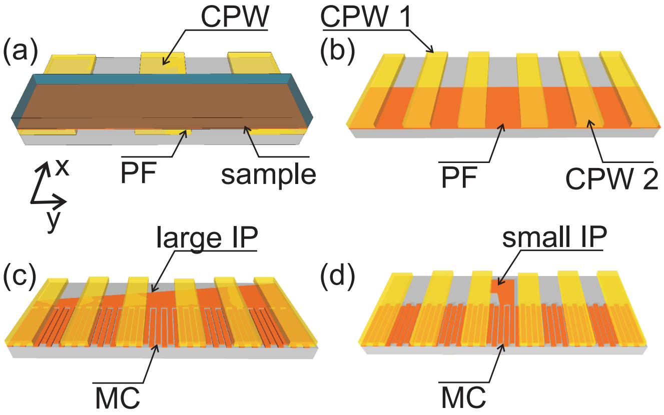

Figure 3.6: Typical sample setups: (a) VNA-FMR setup for plain films (PF) investigated with a wide CPW, where the measured sample is positioned top-down (flip chip) onto the CPW, (b) AESWS setup for plain films with two CPWs, (c) AESWS setup for a nanowire array with a large injection pad (IP) to reprogramm the magnetic state of the whole array, and (d) AESWS setup for a nanowire array with a tailored IP for control of the magnetization in single nanowires.

3.4 Sample Design

Plain Film

Plain films of Py, i.e. $Fe_{20}Ni_{80}$, are investigated by VNA-FMR and AESWS. For VNA-FMR Py is deposited on a substrate, which is top-down positioned onto a CPW [Fig. 3.6 (a)]. For AESWS a thin Py film is structured by optical lithography, see Sec. 4.1. The lateral dimensions are 120 μm × 300 μm [Fig. 3.6 (b)]. The thickness is variable in the range of tens of nanometers. CPWs are then integrated on top of the Py film.

Nanowire Arrays

The nanowire array is structured by electron beam lithography, see Sec. 4.2. The single nanowires are made of Py and have a length of 300 μm, a width w, and a thickness d. w is tailored for different samples. The period of the nanowire array is chosen to be 300 nm for all presented samples. In some samples, nanowires are connected to a μm wide Py area, which behaves as a nucleation or injection pad (IP) for domain walls, see Sec. 2.3. This pad enables us to control the magnetic ground state of the connected nanowires independently from the rest of the nanowires, which will be discussed in Sec. 6. Two typical sample setups are shown in Fig. 3.6 with a large IP (c) to reprogramm the magnetic state across the whole nanowire array, and with a small IP (d) to control only selected nanowires.

4 Preparation

For the preparation of samples, two lithography methods have been employed, optical and electron beam lithography (EBL). Both methods are complementary: while optical lithography is fast and covers large areas, EBL provides much higher resolution. CPWs with $w_{\mathrm{IC}} > 2\ \mu$m have been prepared by optical lithography, while nanowires and alignment markers have been prepared using EBL.

4.1 Optical Lithography

CPWs were prepared using optical lithography and lift off processing. Requirements for the preparation of CPWs, see Sec. 3.1.4, were challenging: CPWs with a total length of 9 mm and a lateral width of 2 μm were needed. The steps of preparation were as follows to meet the requirements:

1. Masks for optical lithography were prepared using a laser writer at Walter-Schottky-Institut of TUM.
2. Semi-insulating Gallium Arsenide GaAs[1] was used as the substrate material [GaAs (001)].
3. A commercially available bilayer resist system was used. First LOR-3A resist[2] was spin coated onto the substrate at 4500 rpm for 60 s, and baked out for 60 s at 180°C. Then, S1813 G2 resist[3] was spin coated on top at 6000 rpm for 40 s, and baked out for 60 s at 115°C. Bilayer resist systems create undercut resist structures enabling easy lift-off processing.
4. For exposure, an optical mask aligner equipped with a chromium mask was used. Typical exposure times were 3.5 s at a power of 11 mW/cm^2.

---

[1] Freiberger Compound Materials GmbH, Freiberg, Germany

[2] MicroChem Corp., Newton, MA, USA

[3] Rohm and Haas Company, Philadelphia, PA, USA

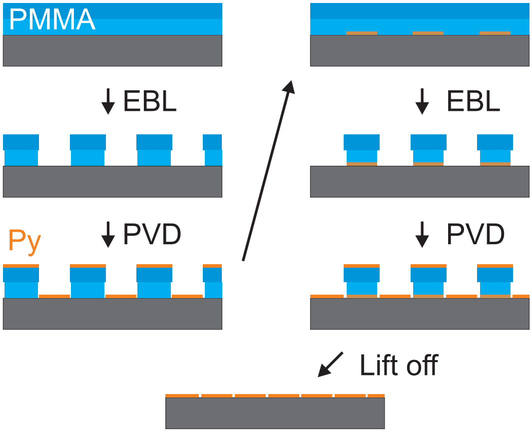

Figure 4.1: Process flow of a multistep EBL process. Accurate alignment is achieved by tailored and optimized alignment marker. A double layer of PMMA resists 50k and 950k is used to obtain an undercut structure. The lithography by EBL and PVD of Py is performed twice.

5. Development of the structures was done using an optical developer MF-26A[4] for 30 s.

6. For material deposition physical vapor deposition (PVD) was used. For CPWs 5 nm thick Cr and 120 to 200 nm thick Au were evaporated.

7. Lift off was achieved by using the commercially available remover 1165[5] for 2 h at 55°C.

4.2 Electron Beam Lithography

Nanowires were prepared using EBL and lift-off processing. To obtain a nanowire array with minimum edge-to-edge separation a double-step EBL process was used as depicted in Fig. 4.1. First,

---

[4] Rohm and Haas Company, Philadelphia, PA, USA

[5] Rohm and Haas Company, Philadelphia, PA, USA

each second nanowire is fabricated (left column in Fig. 4.1), afterwards the second half of the nanowires is prepared in a separate EBL step (right column in Fig. 4.1). The crucial aspect is the alignment of the two separate preparation steps. This was achieved by an accurate marker system on the sample, where an alignment on the same coordinate system was possible for each preparation step. Steps of preparation are as follows:

1. Semi-insulating Gallium Arsenide GaAs was used as the substrate material [GaAs (001)].
2. Coating and baking. A commercially available bilayer electron beam resist 639.10 50k or 639.04 50k[6] is spin coated and baked out, then 679.04 950k is spin coated on top. The 20% higher sensitivity of the 50k resist with respect to the 950k yields undercut for an effective lift off. Typical parameters are: spin speed 6000 rpm with stepped acceleration and duration of 120 s, bake out 2 minutes at 160°C.
3. For exposure of nanowires an Raith e_Line EBL[7] system was used. Importantly for the nanowire exposure, a precise lateral alignment is performed using the perpatterned marker system.
4. For exposure of markers and nanowires the dose was optimized to be 150 μC/cm^2. The stepsize was defined to 6.4 nm, an aperture of 10 μm and an acceleration voltage of 20 kV were used.
5. For the preparation of CPWs by EBL a process with subsequent change of aperture and re-alignment was used. This was necessary to overcome the emerging problems when exposing on different lateral length scales, i.e. 10^2-10^3 nm for the transmission regime, and $10^5 - 10^6$ nm for the pads of a CPW. For the transmission region a stepsize of 6.4 nm, and an aperture of 30 μm were used. For the pad region a stepsize of 50 nm and an aperture of 120 μm were set. These optimizations reduced the exposure time for a set of CPWs to a feasible value, i.e. tens of minutes.

---

[6] Allresist GmbH, Strausberg, Germany

[7] Raith GmbH, Dortmund, Germany

6. Development was done by AR-600 56[8] for 60 s.
7. PVD was used for Py (nanowires) and Cr/Au (markers).
8. Lift off was achieved by using the above mentioned remover 1165f
9. For the preparation of a nanowire array steps 2. to 8. are repeated. The successive EBL exposure allows for a small edge-to-edge separation.

The nanowire array is insulated by a 8 nm thick Al_2O_3 layer deposited by atomic layer deposition [c.f. Sec. 9]. The CPWs are monolithically integrated onto the nanowire array by optical lithography or electron beam lithography. A typical sample is presented in Fig. 4.2. There, four successive electron beam lithography steps were performed (markers, nanowire array 1, nanowire array 2, CPW), where the alignment for each step was crucial. A repeatability of the alignment of some nanometers was achieved as shown by the symmetric nanowire array.

---

[8] Allresist GmbH, Strausberg, Germany

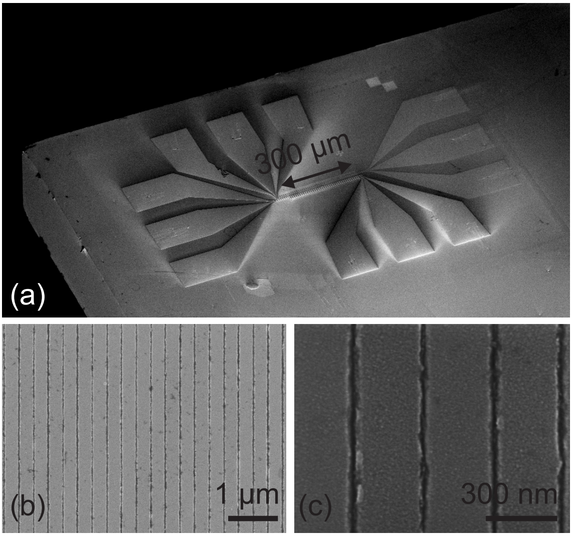

Figure 4.2: SEM image of a typical sample. (a) Four CPWs are integrated on top of a nanowire array. (b) The nanowire array has dimensions of 300 μm $\times$ 100 μm. (b) The period of the array is p = 300 nm, and (c) the edge-to-edge separation amounts to an averaged value of 25 nm.

5 Plain Film Measurements

In this chapter VNA-FMR (see Sec. 3.2.1), TR-AESWS (see Sec. 3.2.3), and FR-AESWS (see Sec. 3.2.2) are performed on Py thin films. We analyze Py thin films of a thickness of 20-30 nm, which are deposited on a GaAs substrate. In Sec. 5.3.2 we focus on the group velocity determination.
Comprehensive investigations using VNA-FMR have been performed by [Kua02, Cou04, Gie05, Kal06, Bil08]. In this chapter we present VNA-FMR on a Py thin film as a reference measurement for the Chapter 9, where the effective magnetization M_{eff} and the linewidth Δf are investigated. AESWS on Py thin films has been reported in literature (TR-AESWS by [Cov02, Cov04, Due09] and FR-AESWS by [Bai03b, Koz09a, Vla10, Yu12], respectively). Comparing to VNA-FMR AESWS additionally allows for the investigation of the group velocity and relaxation length of spin waves.In literature different evaluation methods for the group velocity $v_g = \frac{\partial \omega}{\partial k}$ are reported. We present these methods and suggest their appropriate application depending on the signal-to-noise ratio of the available datasets. This is necessary for the evaluation and discussion in the Chapters 6 and 8.

5.1 Ferromagnetic Resonance Measurements

It is instructive to start with spectra obtained by VNA-FMR measurements, where the maximum k_0 of the spin wave excitation $\rho(k)$ is close to $k_0 = 0$, as shown in Sec. 3.1.6. A 20 nm thick permalloy thin film deposited on a GaAs substrate (sample RH_pf) is positioned in flip chip geometry onto a CPW, see 3.2.1, with an inner conductor width $w_{\text{IC}} = 20$ μm and a gap width of 10 μm, respectively. First we saturated the sample by applying $\mu_0 H_{\text{sat}} = +100$ mT. Then H is decreased in a step-wise manner, and spectra are recorded. The dependence of $Mag(a_{21})(H)$ on the magnetic field strength $\mu_0 H$ at $\eta = 0\,^\circ$ is measured. In Fig. 5.1 (a), $Mag(a_{21})$ data taken for

-100 mT < μ_0H < 100 mT over a wide frequency spectrum is presented. Dark color in the gray-scale plots indicates resonant absorption. A typical resonance behavior is shown in Fig. 5.1 (b). For $\eta = 0\,^\circ$ and $\mu_0 H = 100$ mT the imaginary part $\Im(a_{21})$ (dashed), the real part $\Re(a_{21})$ (dotted) and the magnitude $Mag(a_{21})$ (line) is presented. The data is normalized to the maximum of $Mag(a_{21})$. A resonance is observed at $f_{\mathrm{res}} = 9.1$ GHz. The linewidth Δf of $\Im(a_{21})$, defined in Sec. 2.4.1, is indicated by horizontal arrows in Fig. 5.1 (b). Due to incomplete calibration [Sec. 3.1.3] a_{21} contains a mixture of real and imaginary part of the susceptibility χ. Therefore, we use $Mag(a_{21})$ for the evaluation of the linewidth. It has been shown that the linewidth of $\Delta f_{\mathrm{Mag}} = \frac{1}{\sqrt{3}}\Delta f$. [Sta09] The linewidth is evaluated to be $\Delta f = 0.37$ GHz in Fig. 5.1 (b).
Dark color in Fig. 5.1 (a) represents the ferromagnetic resonance with frequency f_{res}. The response $Mag(a_{21})(H)$ is symmetric, i.e.

$$Mag(a_{21})(-H) = Mag(a_{21})(+H).$$

Furthermore, f_{res} increases monothonically with the absolute value of the applied field $|H|$. The minimum frequency $f_{\mathrm{res}} \simeq 0$ is found at $\mu_0 H = 0$ and increases to $f_{\mathrm{res}} = 9.1$ GHz at $|\mu_0 H| = 100$ mT.
Assuming a homogeneous excitation field we use the Kittel formula Eqn. 2.29 considering the demagnetizing tensor

$$\hat{\mathbf{N}}_{\mathrm{pf}} = \begin{pmatrix} 0 & 0 & 0 \\ 0 & 0 & 0 \\ 0 & 0 & 1 \end{pmatrix} \tag{5.1}$$

which yields

$$f_{\mathrm{res}}^2 = (\frac{|\gamma|}{2\pi})^2 \mu_0^2 \; H \cdot (H + M_{\mathrm{eff}}). \tag{5.2}$$

M_{eff} takes the surface anisotropy, see Sec. 2.2, into account by $M_{\mathrm{eff}} = M_{\mathrm{s}} - \frac{2K_\perp}{d\mu_0 M_{\mathrm{s}}}$. For $H \ll M_{\mathrm{eff}}$ the Kittel formula reduces to a linear relation $f_{\mathrm{res}}(H)^2 \simeq \frac{|\gamma|}{2\pi}^2 \mu_0^2 \; H \cdot M_{\mathrm{eff}}$. This stimulates to display f_{res}^2 versus the applied field, shown in Fig. 5.1 (c). An almost linear field dependence is obtained. The effective magnetization is fitted to be $M_{\mathrm{eff}} = 0.94$ T.

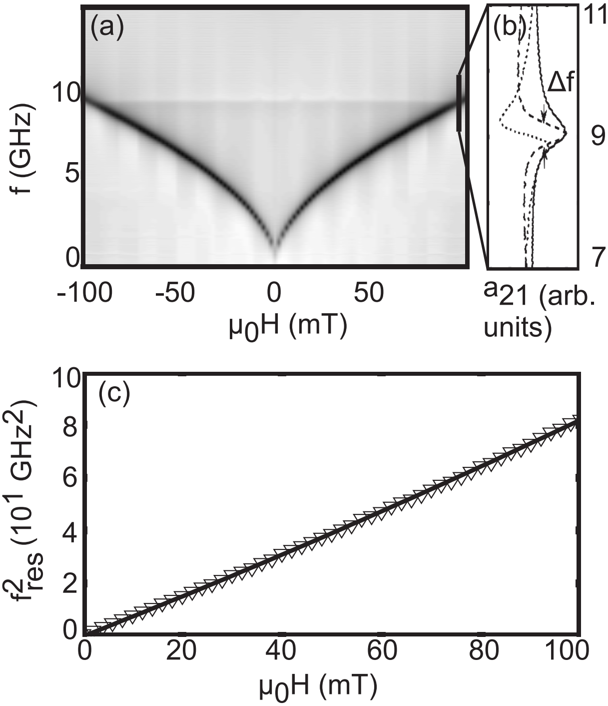

Figure 5.1: (a) Gray scale plot depicting $Mag(a_{21})$ of sample RH_pf versus applied field H on the x-axis and the frequency f on the y-axis. Dark contrast indicates a resonance behavior. A typical ferromagnetic resonance is depicted in (b). At $\mu_0 H = +100$ mT (perpendicular line) the spectra shows a resonance at $f_{\text{res}} = 9.1$ GHz where $Mag(a_{21})$ (line), $\mathfrak{Im}(a_{21})$ (dashed), and $\mathfrak{R}(a_{21})$ (dotted) are depicted. The arrows indicate the linewidth Δf as defined in Sec. 2.4.1. The resonance frequency f_{res} increases with increasing absolute field value $|H|$. (c) The square of the resonance frequency f^2_{res} is presented (triangles). The line is calculated according to the adapted Kittel equation Eqn. 2.29 using $\mu_0 M_{\text{eff}} = 0.94$ T.

5.2 Time-resolved AESWS

For TR-AESWS two CPWs are integrated on top of an insulated Py thin film (sample RH_50PF) exhibiting a thickness of 30 nm. The two CPWs exhibit a nominal inner conductor width $w_{\mathrm{IC}} = w_{\mathrm{OC}} = 2.0\ \mu$m, gap width of 1.6 μm, and a separation of 12 μm as shown in Sec. 3.2.2. The CPWs are connected to the two ports 1 and 2 of the TDR [Sec. 3.2.3]. A voltage step pulse is used to excite the spin system. The spin system precesses with the eigenfrequency f_0 and decays with the effective relaxation time τ_{eff} (see Sec. 2.4.3). Furthermore, spin waves propagate with a group velocity v_{g} of several km/s and are detected at the second CPW. First, we focus on the self-inductance measurements detecting SWs at the emitter CPW (i.e. t_{ii}) and then address propagating spin waves (i.e. t_{ji}, $i \neq j$).

5.2.1 Self-inductance Measurements

In Fig. 5.2 (a) the self-inductance signal t_{11} (black) obtained at $\mu_0 H = 10$ mT for $\eta = 0°$ is presented. The TDR applies the voltage step pulse at time $t = 0$. For $t > 0$ a damped oscillation occurs. We describe the data by a decaying sinusoidal oscillation as described by Eqn. 2.31. The equation is adapted for a distribution of excited wave vectors and is transformed to

$$t_{11}(t) \propto \exp\left(-\frac{t}{\tau_{\mathrm{eff}}}\right) \cdot \cos\left(2\pi f_0 + \tilde{\Phi}\right), \tag{5.3}$$

where the distribution of excited wave vectors is considered by introducing an effective relaxation time τ_{eff}. f_0 is the center frequency of the wave vector distribution and $\tilde{\Phi}$ is a phase shift. We obtain $\tau_{\mathrm{eff}} = 0.37$ ns and $f_0 = 4.0$ GHz by the fitting procedure [c.f. red curve in Fig. 5.2 (a)]. f_0 and τ_{eff} at different magnetic fields $\mu_0 H$ are determined. The obtained f_0 and the effective linewidth $\Delta\omega_{\mathrm{eff}} = 2/\tau_{\mathrm{eff}}$ (Eqn. 2.33) are summarized in Fig. 5.2 (b). f_0 (circles) increases with increasing absolute field value $|H|$, whereas $\Delta\omega_{\mathrm{eff}} = 2/\tau_{\mathrm{eff}}$ decreases slightly. An average value of $\Delta f_{\mathrm{eff}} = \frac{1}{\pi\tau_{\mathrm{eff}}} \simeq 0.8$ GHz is evaluated, which is larger compared to the value obtained in Sec. 5.1. We attribute this to the extrinsic contributions, see Sec. 3.1.6.

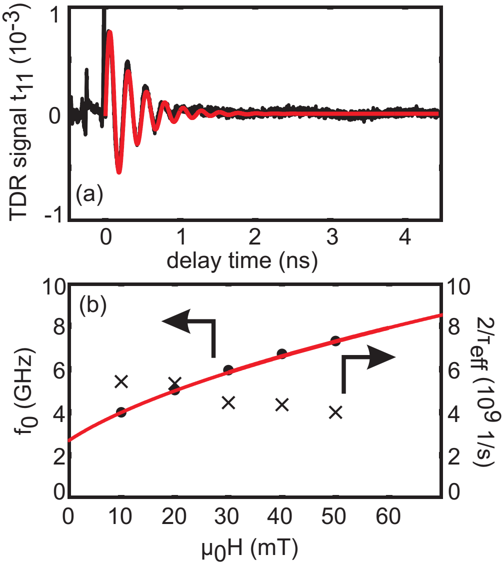

Figure 5.2: (a) Self-inductance measurement t_{11} (sample RH_50PF) of a 30 nm thick permalloy thin film by a TDR module (black). The step voltage pulse at $t = 0$ applied to the CPW deflects the spin system, which starts to precess. The decaying oscillation measured at $\mu_0 H = 10$ mT is fitted by a damped sinusoidal behavior (red), where $f_0 = 4.0$ GHz and $\tau_{\text{eff}} = 0.37$ ns. (b) Evaluated eigenfrequency f_0 (circles) and decay $2/\tau_{\text{eff}}$ (crosses) for different magnetic field values. The fitted red line is obtained by the dispersion relation [Kal86] with wave vector $k_0 = 0.5\ \frac{\text{rad}}{\mu\text{m}}$, and the effective magnetization $M_{\text{eff}} = 1.08$ T.

We use the dispersion relation for DE waves Eqn. 2.37 to calculate f_0 at different field values (red line). The fitting parameters are the wave vector $k_0 = 0.5\ \frac{\text{rad}}{\mu\text{m}}$, and the effective magnetization $M_{\text{eff}} = 1.08$ T. We attribute the difference of M_{eff} compared to the obtained value in Sec. 5.1 to small variations of the evaporation process.

5.2.2 Transmission Measurements

In the following the transmission data obtained by TR-AESWS (sample RH_50PF) is discussed. We model the data by a set of parameters. Some values, i.e. the resonance frequency and the effective lifetime are taken from the preceding section. Further parameters needed for modeling are the group velocity and the excitation width of the CPW.

In Fig. 5.3 (a) the transmitted signal t_{21} is presented for $\mu_0 H = 10$ mT (Sec. 3.2.3). Ringing is seen up to $t \approx 2.8$ ns. At the detector CPW we observe a delayed response with a maximum amplitude at $t_{\text{M}} = 1.2$ ns. For $\mu_0 H = 80$ mT such wave packets show ringing up to $t \approx 4$ ns (not shown). Note that there are voltage spikes also at $t \simeq 0$. We attribute them to direct electromagnetic crosstalk. The crosstalk occurs at the speed of light being much faster than the SW with the group velocity v_{g}. For a quantitative analysis we now consider Eqn. 3.15. As we are in the limit $\Delta k \ll \frac{\pi}{p}$ we assume $\varsigma \simeq 0$. Then we get

$$t_{21}(t) \propto \frac{Ce^{-\frac{t}{\tau_0}}}{\delta^2} \cdot \exp\left[\frac{-(y - v_g t)^2}{4\delta^2}\right] \cdot \cos\left(k_0 y - 2\pi f_0 t + \Phi\right). \quad (5.4)$$

Using Eqn. 3.10 the intrinsic relaxation time reads

$$\tau_0 \simeq \frac{2}{\frac{2}{\tau_{\text{eff}}} - v_g \frac{2}{\delta}}. \quad (5.5)$$

This relation is discussed in more detail in Sec. 6. Combining Eqns. 5.4 and 5.5 we obtain

$$t_{21} \propto \frac{C \exp \frac{t}{2}\left(\frac{2}{\tau_{\text{eff}}} - v_g \frac{2}{\delta}\right)}{\delta^2} \cdot \exp\left[\frac{-(s - v_g t)^2}{4\delta^2}\right] \cdot \\ \cdot \cos\left(k_0 s - 2\pi f_0 t + \Phi\right), \quad (5.6)$$

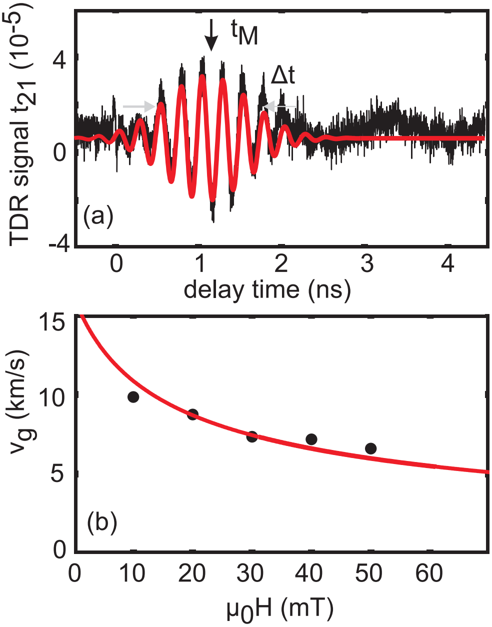

Figure 5.3: (a) Transmission data t_{21} (sample RH_50PF) showing propagation of a spin wave packet with a maximum amplitude at $t_{\mathrm{M}} \simeq 1.2$ ns (black). Equation 5.6 is used to model t_{21} with $v_{\mathrm{g}} = 9.8\ \frac{\mathrm{km}}{\mathrm{s}}$, $\tau_{\mathrm{eff}} = 0.37$ ns, and $\delta = 3.4 \cdot 10^{-6}$ m (red line). (b) Group velocity v_g obtained for different magnetic field values (circles). The calculated group velocity (red) is obtained from the dispersion relation with the values obtained from Fig. 5.2 ($k_0 = 0.5\ \frac{\mathrm{rad}}{\mu\mathrm{m}}$ and $M_{\mathrm{eff}} = 1.08$ T).

which we use as a fitting function for the transmission signals. Here, the effective relaxation time τ_{eff} and the eigenfrequency f_0 are obtained by the self-inductance measurement. We obtain best agreement for a group velocity of $v_{\mathrm{g}} = 9.8$ km/s and an excitation width of $\delta = 3.4 \cdot 10^{-6}$ m [red line in Fig. 5.3 (a)]. In particular the temporal width of the wave packet is modeled excellently, which allows to obtain the excitation width δ. This value is used in the following sections as a reference value for the excitation width.

TR-AESWS is systematically performed at different magnetic fields. The results are presented in Fig. 5.3 (b) (circles). The group velocity decreases with increasing magnetic field from 9.8 km/s to 6.6 km/s. The group velocity is modeled by $v_{\mathrm{g}} = \partial\omega/\partial k$ using Eqn. 2.37 considering the parameters from Fig. 5.2 ($k_0 = 0.5\ \frac{\mathrm{rad}}{\mu\mathrm{m}}$ and $M_{\mathrm{eff}} = 1.08$ T) (red line).

The TR-AESWS is a powerful technique to analyze the group velocity and the excitation properties.

5.3 Frequency-resolved AESWS

In the following we present data obtained from sample Pa_1, i.e. a Py thin film with integrated CPWs as described in Sec. 3.2.2. The thickness of the Py thin film is 28 nm. A VNA is connected to the CPWs, which supplies a continuous electromagnetic wave in the GHz regime. The spin system is excited by the stray field of the electromagnetic wave and resonances with frequency f_{res} and linewidth Δf are detected and discussed.

5.3.1 Self-inductance Measurements

In Fig. 5.4 (a) a typical spectrum is depicted ($\mu_0 H = 30$ mT), which contains three resonances at $f_{\mathrm{res},0} = 6.1$ GHz, $f_{\mathrm{res},1} = 7.0$ GHz, and $f_{\mathrm{res},2} = 7.9$ GHz. The linewidth of the main mode is determined by full width at half maximum of $\Delta f_{\mathrm{eff}} = 0.8$ GHz.

For a continuous wave experiment the SW amplitude a_{11} is described by Eqn. 3.7

$$\Im(a_{11})(\omega) \propto \Im\left[\int \chi(\omega, k)\rho(k)^2 dk\right], \tag{5.7}$$

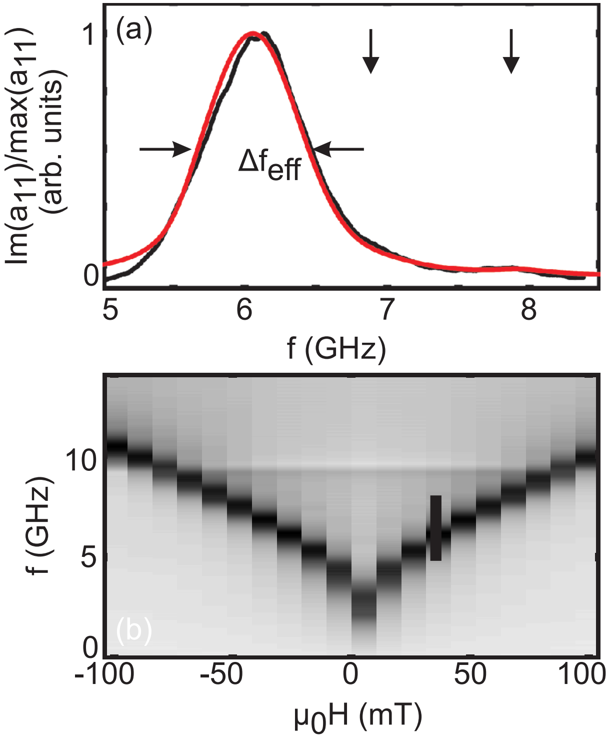

Figure 5.4: (a) Measured (black) and calculated (red) $\Im(a_{11})$ at $\mu_0 H = 30$ mT (sample Pa_1). The perpendicular arrows indicate the higher modes of the CPW. The linewidth Δf_{eff} is marked by horizontal arrows. (b) Gray scale plot of $Mag(a_{11})$ presented as a function of H and f. The perpendicular line at $\mu_0 H = 30$ mT indicates the field position used in (a).

We use Eqn. 5.7 to model the resonant behavior. We construct $\chi(\omega, k)$ by using the spin wave dispersion relation and a Lorentzian-type resonance behavior for each wave vector. Then, $\rho(k)$, M_s, and Δf are used as fitting parameters. We find three relevant wave vectors $k_0 = 0.5$ rad/μm, $k_1 = 1.8$ rad/μm, $k_2 = 3.2$ rad/μm. For the main mode k_0 a Gaussian wave vector distribution $\rho(k)$ as presented in Sec. 3.1.6 is employed. Best agreement is obtained for $M_\mathrm{s} = 1.05$ T, $\Delta f = 0.32$ GHz, and $\Delta k_0 = 0.52$ rad/μm. We only use M_s in this model, however it can be easily expanded to M_eff for the special geometry of our setup. The obtained values are in good agreement with the values obtained in Sec. 5.2. There in particular, $\Delta k_0 = \frac{2}{\delta} = 0.58$ rad/μm is found. The small discrepancy of M_s to the already reported values might arise from minor variations of the evaporation processes.

In Fig. 5.4 (a) the calculated $\Im(a_{11})$ is depicted and shows excellent agreement between measurement and calculation. Calculated as well as measured data is normalized to its maxima. The effective linewidth (see Sec. 3.1.6) amounts to $\Delta f_\mathrm{eff} = 0.8$ GHz. Remaining discrepancies of the main resonance between measurement and model are attributed to the wave vector distribution, which might exhibit deviations from the pure Gaussian distribution.

In Fig. 5.4 (b) $Mag(a_{11})(H)$ is presented. The resonance frequency f_res (dark) increases with the absolute field value $|H|$ and is symmetric, i.e. $Mag(a_{11})(-H) = Mag(a_{11})(+H)$. The minimum frequency $f_\mathrm{res} = 3.0$ GHz is found at $\mu_0 H = 0$ and increases to $f_\mathrm{res} = 10.4$ GHz at $|\mu_0 H| = 100$ mT. There, the linewidth Δf of $Mag(a_{11})$ is evaluated to be 1.44 GHz. The field dependence of $\Im(a_{11})$ $[\Re(a_{11})]$ looks similar compared to $\Im(a_{21})$ $[\Re(a_{21})]$ obtained by VNA-FMR measurements in Fig. 5.4 (b). However, the absolute frequencies at each field value are higher, i.e., $f_\mathrm{res,AESWS} > f_\mathrm{res,FMR}$ and in particular do not show $f_\mathrm{res} = 0$ at $H = 0$. We attribute this to the excitation of SWs with $k \neq 0$. In Sec. 3.1.6 it has been shown, that the excited wave vector by the CPW is $k_0 \simeq 0.5 \frac{\mathrm{rad}}{\mu\mathrm{m}}$. Thus, a propagating spin wave is excited with a finite wave length, which raises the frequency of Damon-Eshbach type SWs (see Eqn. 2.37).

The field-dependent resonance frequencies match well the eigenfrequencies obtained in Fig. 5.2 (b).

5.3.2 Transmission Measurements

In the following the transmission data obtained by FR-AESWS is discussed. Parameters, which we have already obtained by TR-AESWS, are discussed and compared. Further parameters, such as the non-reciprocity parameter β of DE waves and the relaxation length s_r are evaluated.

Modeling of FR-AESWS data

In Fig. 5.5 (a) $\Im(a_{21})$ (black line) and $\Re(a_{21})$ (black dotted) is presented for $|\mu_0 H| = 30$ mT (each normalized to the maximum of $Mag(a_{21})$, i.e., max[Mag(a$_{21}$)]). The oscillatory behavior of $\Im(a_{21})$ and $\Re(a_{21})$ due to a phase accumulation is phase shifted by 90° as expected. For a continuous wave experiment the propagating SW amplitude is described by Eqn. 3.8

$$\Im(a_{21})(\omega) \propto \Im\left[\int \chi(\omega,k)\rho(k)^2 exp(-iks+\Phi_0)dk\right], \tag{5.8}$$

where s is the propagation distance, k is the complex wave vector and $\Im(k) = 1/s_r$ is the inverse spin wave relaxation length, and Φ_0 is the initial phase. We use the same procedure as in Sec. 5.3.1. Also the same parameters are used , i.e., $M_\mathrm{s} = 1.05$ T, and $\Delta f = 0.32$ GHz. At a wave vector of $k_0 = 0.5$ rad/μm this corresponds to a group velocity of $v_\mathrm{g} = 7.1$ km/s. A calculated spectrum is shown in Fig. 5.5 (a) with $\Im(a_{21,calc})$ (red line) and $\Re(a_{21,calc})$ (red dotted).

In Fig. 5.5 (b) $\Im(a_{21})$ is depicted as a gray scale plot. Here, white (black) represents a positive (negative) value therof, and the gray areas depict non-resonant behavior. The frequency of the spin wave modes increase with the absolute field value $|H|$. The phase relation $\Phi(a_{21})_\mathrm{VNA} = \arctan\frac{\Im(a_{21})}{\Re(a_{21})}$ is presented in Fig. 5.6 (a) at $|\mu_0 H| = 30$ mT. For propagating spin waves at $f_\mathrm{res,0} = 6$ GHz, $f_\mathrm{res,1} = 7$ GHz, and $f_\mathrm{res,2} = 8$ GHz [each marked by a perpendicular line in Fig. 5.6 (a)], a negative slope of $\Phi_\mathrm{VNA}(a_{21})$ is observed as expected. For the non-resonant regime an almost constant $\Phi_\mathrm{VNA}(a_{21})$ is detected. Consequently, we extract the resonance frequencies for the three modes depending on H as presented in Fig. 5.6 (b). The

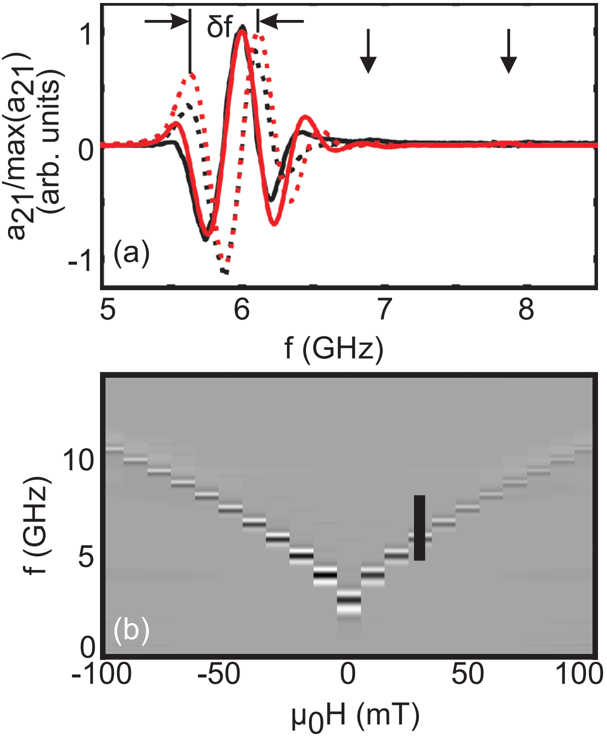

Figure 5.5: (a) Measured data $\Im(a_{21})$ (black line) and $\Re(a_{21})$ (black dotted) obtained at $\mu_0 H = 30$ mT (sample Pa_1), normalized to its maximum value. It exhibits an oscillatory behavior due to an accumulated phase. Vicinal, local extrema in $\Im(a_{21})$ [$\Re(a_{21})$] have a phase shift of $\Delta\Phi = 2\pi$. The difference is defined as δf. Calculated $\Im(a_{21})$ (red line) and $\Re(a_{21})$ (red dotted) by Eqn 5.8. Perpendicular arrows indicate the position of the higher spin wave modes. (b) Gray scale plot of $\Im(a_{21})$ plotted versus H and f. The black-white contrast is a signature of the propagation of the SWs. The perpendicular line at $\mu_0 H = 30$ mT indicates the field position used in (a).

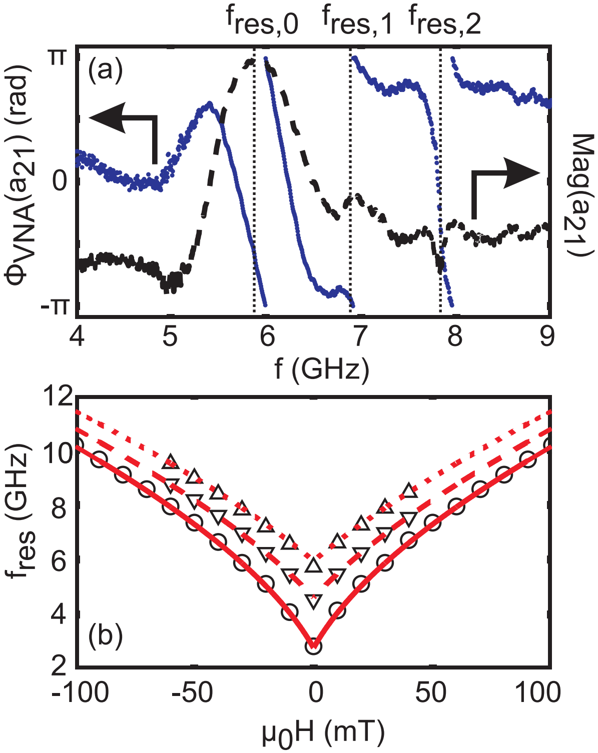

Figure 5.6: (a) The phase $\Phi_{\mathrm{VNA}}(a_{21})$ (points) and $Mag(a_{21})$ (dashed) is presented (sample Pa_1). The main maximum denoted with $f_{\mathrm{res},0}$ exhibits a maximum of $Mag(a_{21})$. At the same time the phase $\Phi_{\mathrm{VNA}}(a_{21})$ decreases as suggested by Eqn. 3.11. For non-resonant behavior, e.g. $f < 5$ GHz the phase $\Phi_{\mathrm{VNA}}(a_{21})$ stays constant. The higher modes denoted by $f_{\mathrm{res},1}$ and $f_{\mathrm{res},2}$ exhibit a charactersitic change of slope. (b) The maxima of $Mag(a_{21})$ are fitted by the dispersion relation Eqn. 2.37. The corresponding wave vectors are $k_0 = 0.5\ \frac{\mathrm{rad}}{\mu\mathrm{m}}$ (line), $k_1 = 1.8\ \frac{\mathrm{rad}}{\mu\mathrm{m}}$ (dashed), and $k_2 = 2.9\ \frac{\mathrm{rad}}{\mu\mathrm{m}}$ (dotted).

dispersion relation for DE waves Eqn. 2.37 is used as fitting function. The effective magnetization M_{eff} and the excited wave vectors k_i are used as fitting parameters. Best results are obtained for the effective magnetization $M_{\mathrm{eff}} = 1.05$ T, the wave vectors $k_0 = 0.5\ \frac{\mathrm{rad}}{\mu\mathrm{m}}$ (line), $k_1 = 1.8\ \frac{\mathrm{rad}}{\mu\mathrm{m}}$ (dashed), and $k_2 = 2.9\ \frac{\mathrm{rad}}{\mu\mathrm{m}}$ (dotted) as shown in Fig. 5.6 (b).

The presented method is a comprehensive model to describe the reflection data as well as the transmission data. It incorporates the dispersion relation and an excitation profile that allows to include different local excitation maxima. Thus, it is capable of analyzing also complicated excitation profiles and dispersion relations or band structures.

When comparing the measured with the modeled data in reflection [Fig. 5.4 (a)] we find a good agreement. In particular also the flanks of the main resonance (i.e. $f \neq f_0$) are modeled well. However, focusing on the transmission data [Fig. 5.5 (a)] discrepancies of measured and modeled amplitudes in the corresponding regions $f \neq f_0$ are found. In fact, the measured data there exhibit smaller propagation signals as expected from Fig. 5.4 (a). We attribute this feature to small differences of the two CPWs (also stated in [Vla10]). This is also confirmed by the reflection data $Mag(a_{11})$ and $Mag(a_{22})$, where the measured datasets exhibit a relative frequency shift to each other of 50 MHz. This small frequency shift (50 MHz $\ll \Delta \mathrm{f}_{\mathrm{eff}}$) results in a severe suppression of the transmitted signal in the flanks of the resonance (i.e. $f \neq f_0$). This result, obtained due to the simultaneous modeling of reflection and transmission data, highlights the necessity of a precise lithography for the fabrication of equal CPWs.

Group Velocity

In the preceding section we obtained the group velocity as a side effect of the modeling of the spin wave resonance. There are three different methods to evaluate the group velocity without the necessity of a full, involved description of the spin wave resonance. The group velocity is obtained by evaluation of the phase $\Phi(a_{21})$, the imaginary (real) part $\Im(a_{21})$ [$\Re(a_{21})$], and the higher modes of the excitation spectrum $\rho(k)$ of the CPW. Though we mainly use the two last methods, for completeness we shortly describe all three meth-

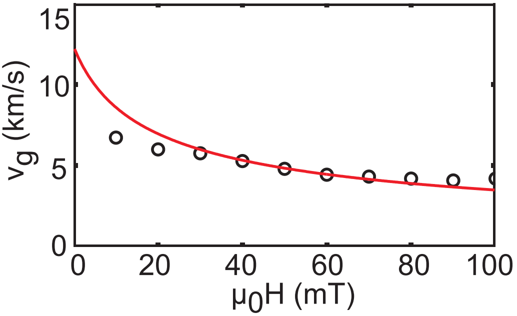

Figure 5.7: The group velocity v_g evaluated by Eqn. 5.9 of sample Pa_1. The line shows the calculated group velocity from the dispersion relation for the relevant parameters, i.e., $M_\mathrm{s} = 1.03$ T and $k_0 = 0.5$ rad/μm.

ods. We will discuss the pros and cons when considering the three different approaches.

First, we discuss the method based on Φ, which exhibits a frequency resolution in the 10^6 Hz regime given by the frequency steps of the VNA. The phase relationship Φ_VNA between emitter and detector is $\Phi_\mathrm{VNA} = -k \cdot s$ (see Eqn. 3.11). Furthermore, the resonance frequency f_res depends on k. Thus, exciting a certain k' we get $f_\mathrm{res}(k')$ with a phase relationship $\Phi_\mathrm{VNA}(k')$. In FR-AESWS a spectrum of wave vectors $\rho(k)$ around k_0 is excited, which yields a phase evolution Φ_VNA as shown in Fig. 5.6 (a). We extract the group velocity by Eqn. 3.12. Thus, for a continuous wave experiment the phase relationship between emitter and detector contains the full information about $v_\mathrm{g}(\Phi_\mathrm{VNA})$. The slope of the k_0 mode at $\mu_0 H = 30$ mT amounts to $\frac{\partial \Phi_\mathrm{VNA}}{\partial f} = 1.05 \cdot 10^{-8}\ \frac{\mathrm{rad}}{\mathrm{s}}$, see Fig. 5.6 (a). Consequently, this corresponds to a group velocity of $v_\mathrm{g} = 7.2$ km/s, which is in good agreement with value from the preceding section. It has been shown that using this method a high-resolution dispersion mapping is possible. [Bao08] However, the evaluation technique is suitable as long as the transmission signal is dominated by the propagating SW and not the direct eletromagnetic coupling. Direct electromagnetic coupling mimics a SW with higher group velocity.

Second, we discuss the method based on $\Im(a_{21})$, which offers a frequency resolution in the 10^8 Hz regime, concomitant with an improved stability in presence of electromagnetic crosstalk. This way [Bai03b, Neu10, Yu12] established to extract the group velocity for a transmission signal, that contains both, SW propagation and direct electromagnetic crosstalk, is based on the evaluation of extrema of $\Im(a_{21})$ and $\Re(a_{21})$. Vicinal, local extrema in $\Im(a_{21})$ [$\Re(a_{21})$] have a phase shift of $\Delta\Phi = 2\pi$. This reduces Eqn. 3.12 to

$$v_g = \frac{\Delta f \cdot 2\pi}{\Delta\Phi/s} = \frac{\delta f \cdot 2\pi}{2\pi/s} = \delta f \cdot s, \qquad (5.9)$$

where s is the propagation distance and δf is the difference between local extrema in $\Im(a_{21})$ [$\Re(a_{21})$] as depicted in Fig. 5.5 (a). We identify the oscillations as the propagation signal of spin waves. The frequency difference between the two maxima of $\Im(a_{21})$ [$\Re(a_{21})$] in Fig. 5.5 (a) amounts to $\delta f = 0.469$ GHz ($\delta f = 0.474$ GHz). With $s = 12\ \mu$m this corresponds to a group velocity of $v_{\mathrm{g}} = 5.7 \pm 0.2$km/s. The evaluated group velocity v_{g} is summarized in Fig. 5.7 (a) (circles), the line is the calculated group velocity exploiting the fitted values M_{eff} and k_0. The values are smaller compared to the first method. We attribute this to the averaging over the bending of the dispersion relation.

The third method uses different modes of the CPW excitation $\rho(k)$ as shown in Fig. 3.5. This method is independent from electromagnetic crosstalk between the CPWs. We approximate equation 3.12 by

$$v_g = \frac{\partial\omega}{\partial k} \simeq \frac{2\pi(f_2 - f_1)}{k_2 - k_1}. \qquad (5.10)$$

The group velocity is averaged over a broad range of wave vectors $k_2 - k_1$, which explains the systematically smaller values for DE-type modes already observed in different studies [Yu12]. Evaluating the dataset from Fig. 5.6 (a) we find a group velocity of $v_{\mathrm{g}} = 5.3 \pm 0.4$km/s. Caused by the bending of the dispersion relation the expected group velocity values extracted by this method are smaller compared to the preceding methods.

In conclusion we state, that the appropriate method depends on the dataset and amount of electromagnetic crosstalk.

Method	Accuracy	Stability
$\Delta\Phi$	very high	low
$\mathfrak{I}(a_{21})$	high	good
$\rho(k)$	low	very good,

where *accuracy* describes the frequency resolution, and *stability* describes the stability of the group velocity evaluation in presence of disturbing contributions, e.g. electromagnetic crosstalk. This analysis prepares for the discussion in Sec. 6, where the contribution due to electromagnetic crosstalk is large.

Non-reciprocity

Analyzing spin wave propagation in detail we focus on the spin wave amplitude at the detector. A characteristic quantity is the propagation attenuation $a_{21}/a_{11} = \frac{\max[\mathrm{Mag}(a_{21})]}{\max[\mathrm{Mag}(a_{11})]}$ ($a_{12}/a_{22} = \frac{\max[\mathrm{Mag}(a_{12})]}{\max[\mathrm{Mag}(a_{22})]}$), which describes the detected maximum amplitude normalized to the input amplitude. In Fig. 5.8 (a) a_{21}/a_{11} (open circles) and a_{12}/a_{22} (filled circles) is presented, where for $H < 0$ ($H > 0$) a_{12}/a_{22} (a_{21}/a_{11}) is higher and amounts to a maximum value of 0.55 in contrast to 0.35 for the lower value. This effect is called non-reciprocity. We define the non-reciprocity parameter β by

$$\begin{aligned} a_{21} &= \beta a_{11} \exp^{-\frac{s}{s_\mathrm{r}}} \\ a_{12} &= (1-\beta) a_{22} \exp^{-\frac{s}{s_\mathrm{r}}} \\ \Rightarrow \beta &= \frac{\frac{a_{21}}{a_{11}}}{\frac{a_{21}}{a_{11}} + \frac{a_{12}}{a_{22}}}, \end{aligned} \tag{5.11}$$

where s_r is the relevant relaxation length which is the same for counter-propagating spin waves. In Fig. 5.8 (b) the non-reciprocity parameter β is presented. We find $\beta < 1/2$ ($\beta > 1/2$) for $H > 0$ ($H < 0$), respectively. The maximum (minimum) value amounts to 0.71 (0.35). The magnitude of the non-reciprocity β has been measured for strip line (SL) excitation [Dem09] and for asymmetric coplanar strip transmission line (ACPS) excitation. [Sek10] The authors find values of $\beta_\mathrm{SL} = 0.81 \pm 0.05$ and $\beta_\mathrm{ACPS} = 0.63$. The non-reciprocity does not depend on the propagation distances. [Sek10] This indicates that the reason for the non-reciprocity is based on

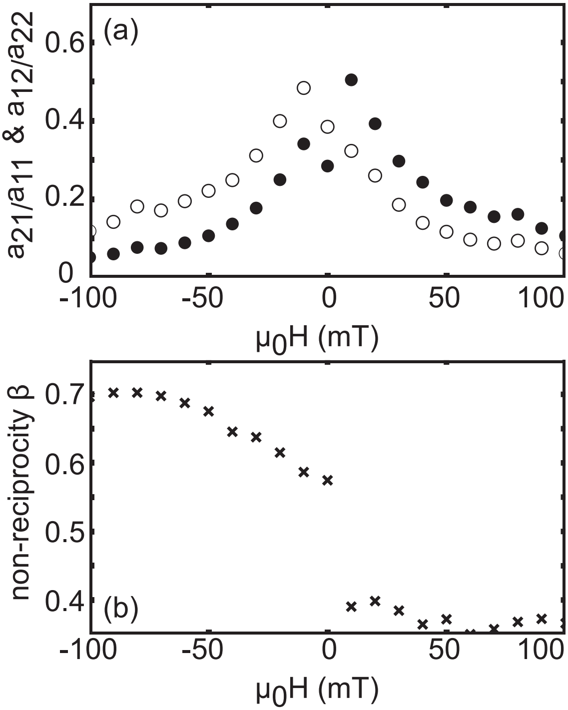

Figure 5.8: (a) a_{21}/a_{11} (filled circles) and a_{12}/a_{22} (open circles) is depicted (sample Pa_1). For $H < 0$ ($H > 0$) a_{12}/a_{22} (a_{21}/a_{11}) provides the larger signal. (b) Non-reciprocity factor β as a function of H. For a value of $\beta > 0.5$ ($\beta < 0.5$) the propagation of spin waves in positive (negative) x-direction is favored.

the excitation process. To explain the non-reciprocal characteristic of spin waves we consider both magnetic field components of the excitation field $\mathbf{h}$, i.e. the in-plane component h_y and the out-of-plane component h_z. [Dem09] In the excitation process, h_x first causes a deflection of the magnetization. Then, the out-of-plane component h_z is acting on the dynamic magnetization. On both sides of the CPW the out-of-plane component is pointing in opposite direction. Thus, on the one side the excitation field h_z is in-phase with the dynamic magnetization and amplifies the spin wave. In contrast on the other side, the excitation field h_z exhibits opposite phase with the dynamic magnetization and diminishes the amplitude. This results in an asymmetric, i.e. a non-reciprocal, spin wave generation in opposite direction. Demidov *et al.* calculated the relative amplitudes $\frac{a_{21}}{a_{11}}$ and $\frac{a_{12}}{a_{22}}$ (originally designated as $m_\pm$) of the opposite spin wave beams and found [Dem09]

$$m_\pm^\mathrm{n} \propto \frac{f_\mathrm{n}}{\gamma} \pm \frac{1}{M_\mathrm{s}}(H^2 - \frac{f_\mathrm{n}^2}{\gamma}^2), \tag{5.12}$$

here $n = 1, 2, 3...$ is the quantization of the mode, and f_n is the frequency of the corresponding mode. In Eqn. 5.12 the non-reciprocity depends on the saturation magnetization M_s (not considering an out-of-plane anisotropy). For low M_s a very high non-reciprocity is found, e.g. in YIG $\beta = 0.9$ [Bue00]. For Py the magnitude of β is measured experimentally to be $\beta = 0.77$. [Dem09]

Relaxation Length and Intrinsic Relaxation Time

An important dynamic property of SWs is the relaxation length s_r. We transform Eqn. 5.11 to $s_r = -s \cdot \ln(\frac{a_{21}/a_{11}}{\beta})$ and the relaxation length s_r is determined. We obtain $s_r = 6.7$ μm for $\mu_0 H = 100$ mT which is a typical value for plain film of Py. In literature we find for 40 nm thick Py thin films a relaxation length of $s_r = 6.4$ μm and $s_r = 5.3$ μm. [Bir12, Pir11] Large values of $s_r > 20$ μm are found at low magnetic field values $\mu_0 H < 20$ mT. (see also [Neu11a]). We attribute this non-physical values to the electromagnetic behavior of the AESWS setup.

The intrinsic relaxation time τ_0 is related to the group velocity and relaxation length by $s_r = v_g \cdot \tau_0$. [Sil99] Using the values from the preceding section an average value of $\tau_0 = 2$ ns is obtained. In literature a value of 1.6 ns [Bai03b] is found, which is slightly smaller by 20 %. The intrinsic relaxation time allows to deduce the damping parameter α. The damping parameter α is calculated according to [Sta09] from

$$\frac{1}{\tau_0} = \alpha\mu_0\gamma(H + M_\mathrm{s}/2). \tag{5.13}$$

This yields a damping parameter of $\alpha = 0.006$. This value for α is in good agreement with values reported in literature. [Pat75, Wol09]

5.4 Conclusion

Generally, we have used AESWS as a powerful technique for investigation of the spin wave dispersion. Analyzing propagating spin waves a dynamical analysis is possible, which helps to discover unforeseen effects. Two techniques, i.e., TR-AESWS and FR-AESWS, stand out for thier complementary abilities.

The high temporal resolution of TR-AESWS allows the propagating spin waves to be discriminated from the electromagnetic crosstalk and therefore the group velocity can be determined. Furthermore, the temporal evolution of the spin wave packet includes information about the excitation width δ of the CPW. A restriction of TR-AESWS is the simultaneous excitation of different modes, that cannot be distinguished. In principle, a Fast Fourier transformation of the dataset to distinguish the modes is possible, however, the resulting dataset lacks a phase resolution.

The complementary technique FR-AESWS, with a high frequency resolution, allows to investigate complicated band structures, e.g. different spin wave modes separated in frequency. Even different ferromagnetic structures vicinal to a single CPW can be measured at once, as long as the resonance frequencies are separated. We also analyzed propagating spin waves. The drawback of this technique is the simultaneous measurement of propagating spin waves and the electromagnetic crosstalk. A discrimination of these two contributions is required.

We conclude, that both techniques are useful and necessary for a comprehensive study. While FR-AESWS has evolved to be the primarily used technique due to its high sensitivity and low requested time for measurement, we stress that in particular for unknown samples the TR-AESWS technique is indispensable to further substantiate the propagation of a spin wave.

6 A One-dimensional Magnonic Crystal with Easy Axis Magnetization

Of special interest in magnonics is a one-dimensional magnonic crystal (1D MC) consisting of an array of bistable nanowires due to the capability to reprogram the magnetic state by the magnetic history. [Top10, Tac10c] The bistable property of nanowires is based on the rectangular shape and the lateral dimension in the sub-micrometer regime. This yields an easy axis (EA) (see Sec. 2.2) parallel to the nanowire axis and appropriately leads to a bistable magnetization. In the following we will revisit the capability to reprogram the magnetic configurations of a 1D MC, which has been reported in literature [Top10, Gub10, Tac10c, Top11a, Din11b]. A detailed analysis of the spin wave propagation in a 1D MC has not been adressed. Consequently, we investigate spin wave propagation in a 1D MC by TR-AESWS and FR-AESWS, as introduced in Secs. 3.2.3 and 3.2.2, and describe the measurements by simulations obtained by PWM, see Sec. 2.5. We show a novel magnonic metamaterial behavior in Sec. 6.3.3, i.e., a behavior that natural materials do not possess.

6.1 Magnetostatic Behavior

In this section the hysteresis curves and quasi-static magnetization profiles, i.e., the local orientation of magnetic moments, are discussed. The reversal processes and the use of an injection pad for domain walls (IP), see Sec. 3.4, are addressed. The quasi-static magnetic state $\mathbf{M}(\mathbf{r})$ is known to significantly influence the spin wave eigenmodes. [Top10, Gub10, Tac10c, Top11a, Din11b, Din11a] For 1D MCs the magnetic state is controlled by the magnetic field *and* the magnetic field history. Therefore, it is necessary to discuss field dependent magnetic configurations $\mathbf{M}(\mathbf{r})$. A powerful method to study the magnetic state $\mathbf{M}(\mathbf{r})$ is magnetic force microscopy (MFM), where the stray field of individual nanowires is detected. However, the scan area of MFM is restricted. A complementary technique is magneto-optical Kerr effect (MOKE) microscopy. MOKE allows to scan larger areas with however smaller spatial resolution compared to MFM. In our setup, MOKE detects the integral magnetization $\mathbf{M}$ within an area of a few 10 μm^2 as a function of the applied field H. This allows for obtaining a hysteresis curve.

Magnetic Force Microscopy

We perform magnetic force microscopy (MFM)[1] on a reference sample which is nominally identical to RH_50, which will be studied with MOKE and AESWS later. The nanowire array is equipped with a large IP [c.f. Fig. 3.6 (c)]. The sample consists of an array of nanowires with the period $p =$ 300 nm. The edge-to-edge separation is 45 nm, the thickness of the evaporated permalloy is 30 nm, and the length of the nanowires is 300 μm. Neighboring nanowires are shifted by 5 μm in x direction. Each second nanowire is connected to the IP. We will show, that such an IP decreases the absolute value of the center field of a switching field distribution $\tilde{H}_{\rm sw}$. In Fig. 6.1 (a) MFM data is shown for $\mu_0 H_{\rm sat} = +100$ mT.[2] As vicinal nanowires are laterally shifted we observe two lines of light contrast, that indicate the poles at the ends of the nanowires. We identify this pattern as the magnetization of the nanowires pointing in positive x direction, i.e. we define the total magnetization $\mathbf{M}_{\rm tot} = \sum \mathbf{M}_{\rm nw} > 0$. In Fig. 6.1 (b) for $\mu_0 H_{\rm sat} = -100$ mT two lines of dark contrast are detected. We identify this as a reversed magnetization (pointing in negative x direction). The total magnetization $\mathbf{M}_{\rm tot} = \sum \mathbf{M}_{\rm nw} < 0$. MFM measurements were also performed for minor loops $\mu_0 H_{\rm ML}$. In a minor loop a sequence of fields is applied, i.e. $\pm H_{\rm sat} \rightarrow H = 0 \rightarrow \mp H_{\rm ML}$ (w.l.o.g. $H_{\rm ML}, H_{\rm sat} > 0$) before taking data and often addresses a non-saturated magnetic state. Such a minor loop measurement is depicted in Fig. 6.1 (c). For the nanowires with (without) IP a dark (light) contrast is detected. A full dark contrast for every second nanowire, and light contrast for

---

[1] For a detailed description of MFM the reader is referred to [Mar87, Rug90, Har99]

[2] MFM pictures were taken with a non-optimized tip after an already long measurement cycle.

the in-between nanowires indicate an antiparallel alignment of neighboring nanowires. Thus, by applying a tailored magnetic history we are capable to reprogram the magnetic state from fully saturated ferromagnetic order (FMO) to a ‘demagnetized’ state in an antiferromagnetic order (AFO).

Magneto-optical Kerr effect

We analyze the magnetization M_{MOKE} of sample RH_50 by the magneto-optical Kerr effect [3]. The laser spot of the MOKE setup has a diameter of about 6 μm, thus the MOKE signal contains information from about 20 nanowires. The magnetization M_{MOKE} is measured for $\mathbf{H} \parallel EA$ (Fig. 6.2 (a)). To start, a maximum field of $|\mu_0 H| = 32$ mT for saturation of the magnetization is applied. The branch with $\mu_0 H_{\mathrm{sat}} = +32$ mT exhibits three regimes with $\frac{\partial M_{\mathrm{MOKE}}}{\partial H} \simeq 0$, i.e. for $\mu_0 H > -6.5$ mT (I), -27.5 mT $< \mu_0 H < -6.5$ mT (II), and $\mu_0 H < -27.5$ mT (III). Regimes I and II (II and III) are separated by jumps of M_{MOKE}, i.e. $\frac{\partial M_{\mathrm{MOKE}}}{\partial H} \gg 0$, with a width of $\Sigma_H = 5$ mT ($\Sigma_H = 6$ mT).
The branch starting from $\mu_0 H_{\mathrm{sat}} = -32$ mT also exhibits regime I and an equivalent switching behavior separating regime I and II. In particular, at $|\mu_0 H| \simeq 10 \pm 3$ mT the averaged magnetization is near $M_{\mathrm{MOKE}} = 0$ for both directions. However, regime II and regime III are not separated, rather a continuous transition with $\frac{\partial M_{\mathrm{MOKE}}}{\partial H} > 0$ is detected.

Reversal Mechanism

We identify the characteristic magnetic state of Fig. 6.1 (c) with regime II in MOKE measurements. This magnetic state, where neighboring nanowires exhibit opposite magnetization, is denoted as the antiferromagnetic order (AFO) configuration. [Top10, Top11a] In contrast, the magnetic state in Figs. 6.1 (a) and (b) is called ferromagnetic order (FMO) configuration, which we identify by regime I and III in MOKE measurements. We focus on the microscopic origin

---

[3] For a detailed description of MOKE the reader is referred to [Arg55, Qiu00, Pol08]

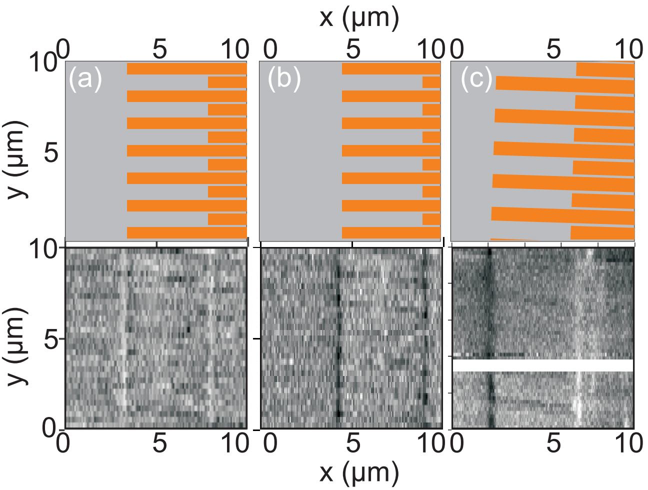

Figure 6.1: Magnetic Force Microscope images in remanence and corresponding sketches for different magnetic histories as described in the text. The nanowires are oriented horizontally and neighoring nanowires are shifted by 5 μm in x-direction. The two perpendicular lines with light or dark contrast are a measure of the magnetization of the nanowires. (a) for $\mu_0 H_{\text{sat}} = +100$ mT a light contrast is observed due to positive magnetization direction, (b) $\mu_0 H_{\text{sat}} = -100$ mT a dark contrast is observed due to negative magnetization direction, (c) $H_{\text{sat}} \rightarrow \quad - H_{\text{ML}}$ dark (left) and light (right) contrast is detected, which indicates an antiparallel magnetization of neighboring nanowires.

of the hysteresis curve depicted in Fig. 6.2 (a). It is instructive to consider the total magnetization $\mathbf{M}_{\mathrm{tot}}$ of the array of nanowires to consist of single, independent nanowires with a bistable magnetization $\mathbf{M}_{\mathrm{nw}} = \pm M_{\mathrm{nw}}\mathbf{e}_x$. The magnetization of the i^{th} nanowire $\mathbf{M}_{\mathrm{nw,i}}$ is able to switch independently from $\mathbf{M}_{\mathrm{nw,i+1}}$. The switching field distribution can be modeled by a Néel-Brown model for a single particle, which describes the switching probability by the nucleation of a domain wall. [OBr12] A potential barrier is introduced to describe the reversal of a nanowire that yields a switching field distribution. The switching field distribution is described by a mean switching field $\tilde{H}_{\mathrm{sw}}$ and a width of the switching field distribution Σ_H. [Wer97] In particular, the nucleation of domain walls is the relevant process for switching. This yields bistable nanowires, that are characterized by a square-shaped hysteresis loop for a single nanowire, that are defined by an abrupt reversal of the magnetization between two stable remanent states. [Lar07] This reversal process is influenced by an IP, as a domain wall is nucleated more easily there compared to the nanowire. Thus, we are able to control the magnetic state by an additional IP and a tailored magnetic history.

6.2 Spin Wave Modes in a 1D MC

In this section the dynamic response of arrays of nanowires is investigated, which depends on the magnetization configuration $\mathbf{M}(\mathbf{r})$ and the applied field H. For AESWS two CPWs are integrated on top of the nanowire array. We focus on two samples: sample RH_50 described in Sec. 6.1 (edge-to-edge separation of 45 nm, thickness of 30 nm), and sample RH_63, which differs from sample RH_50 in the edge-to-edge separation (25 nm) and thickness (35 nm). In contrast to sample RH_50, an IP is not included on RH_63, thus the AFO configuration is not well defined and disordered. [Din11b] Therefore we will not address the AFO state in this case.

6.2.1 Phenomenology

FR-AESWS allows the mapping of spin wave modes over a wide field and frequency spectrum. We compare a full field scan starting from a positively saturated state and ending in a negatively saturated state

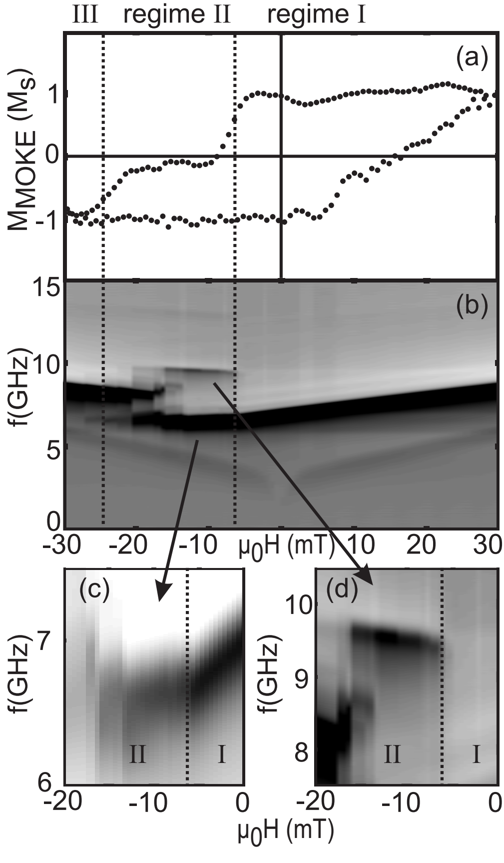

Figure 6.2: (a) Hysteresis curve measured by MOKE of sample RH_50 which is equipped with an IP. Three regimes are distinguished: $\mu_0 H > -6.5$ mT (regime I), -27.5 mT$<\mu_0 H < -6.5$ mT (regime II), and $\mu_0 H < -27.5$ mT (regime III). (b) $\Im(a_{11})$ is subdivided in corresponding regimes (dotted lines). For $f > 6$ GHz we observe one strong resonance in regime I and III, whereas there are further modes in regime II. For $f < 5$ GHz the additional resonance from the IP is observed. (c) and (d) are magnifications of (b) and focus on the behavior of the main and the higher order mode, respectively. (d) The higher order mode at $f_{\mathrm{res}} = 9.6$ GHz exhibits maximum signal strength at -13 mT$<\mu_0 H < -11$ mT.

with the magnetostatic behavior. We show abrupt changes of the modes, which we attribute to reversal processes of the magnetization of nanowires found in Sec. 6.1.

In Fig. 6.2 (b) $\Im(a_{11})$ is presented, which exhibits several spin wave resonances at different frequencies. The field values in FR-AESWS, where the spectra are changing significantly coincide with the field values for reversal processes measured by MOKE. This is marked by perpendicular dotted lines in Fig. 6.2. We have found FMO configuration for regimes I and III in Sec. 6.1. Analyzing FR-AESWS data for this configuration we find three spin wave resonances. A dominant mode is detected for $6 < f_{\mathrm{res}} < 9$ GHz. In regime I the mode exhibits $\frac{\partial f_{\mathrm{res}}}{\partial H} > 0$, and in regime III we find $\frac{\partial f_{\mathrm{res}}}{\partial H} < 0$, both with a high signal strength. Two higher modes are observed at $12 < f_{\mathrm{res}} < 14$ GHz with a smaller signal strength. These two higher modes run parallel to the main mode and are separated by 0.6 GHz. The modes are found to be non-symmetric with respect to $H = 0$, and show a hysteresis (other direction not shown). We identify the main mode and the higher modes with the characteristic FMO modes consistent with [Top11a]. The mode structure is analyzed in more detail later (see Sec. 6.2.2).

In regime II we find a mode at $6 < f_{\mathrm{res}} < 8$ GHz, where abrupt changes of the resonance frequency are observed. Its resonance frequency f_{res} exhibits a kink at $\mu_0 H = -6.5$ mT. The signal strength of the main mode in regime II is weaker compared to regime I [Fig. 6.2 (c)]. For a further decrease of the field to -13.0 mT slight variations of f_{res} are observed. Importantly a continuous change of slope $\frac{\partial f_{\mathrm{res}}}{\partial H}$ is detected. The lowest resonance frequency is found at $\mu_0 H = -13.0$ mT. At lower field values $\mu_0 H \leq -13.5$ mT abrupt jumps are observed which result in an increased resonance frequency.

In Fig. 6.2 (d) a magnification of the frequency regime $7.5 < f_{\mathrm{res}} < 10.5$ GHz is depicted. There, further modes appear abruptly at $\mu_0 H = -6.5$ mT with $f_{\mathrm{res}} = 9.6$ GHz and $f_{\mathrm{res}} = 13.3$ GHz, both indicating $\frac{\partial f_{\mathrm{res}}}{\partial H} < 0$. Decreasing the field to -13.0 mT several small abrupt changes are observed, each yielding an increased signal strength for the mode at $f_{\mathrm{res}} = 9.6$ GHz [Fig. 6.2 (d)]. At lower field values $\mu_0 H \leq -13.5$ mT severe kinks and jumps are observed which even result in additional modes. Furthermore, the mode at $f_{\mathrm{res}} = 9.6$ GHz exhibits a lower signal strength.

Kinks and jumps are expected to be provoked by spontaneous changes of the magnetic state, i.e., switching events of single nanowires or clusters of nanowires. [Din11b] The magnetic configuration, and in particular the magnetic disorder, in 1D MCs is crucial for the spin wave eigenmodes. Here, *magnetic disorder* is defined by the deviation from a perfectly periodic magnetic order. Improved magnetic order (i.e. smaller magnetic disorder) decreases the resonance frequency in AFO configuration. [Din11b]

In the following we focus on regime II. We find the first pronounced kink at $\mu_0 H = -6.5$ mT, where the slope $\frac{\partial f_{\text{res}}}{\partial H}$ changes. A similar kink has been observed in Fig. 1 of [Din11b], which has been attributed to the reversal of the magnetization of several nanowires. This is in agreement with the magnetostatic investigation [Sec. 6.1], which suggests an induced switching of nanowires that are connected to the IP. Due to the statistical nature of the reversal process, [OBr12] there remain nanowires connected to the IP without reversal of the magnetization. A further decrease of the magnetic field favors a reversal of the magnetization of these nanowires. Switching of these nanowires improves the magnetic order of the AFO configuration. Consistent with [Din11b], the improved magnetic order yields a decreasing resonance frequency till $\mu_0 H = -13.0$ mT. Concluding, we assume the MC to exhibit an partly disordered AFO configuration, with the highest magnetic order formed at $\mu_0 H = -13.0$ mT.

At the same time, the higher mode with $f_{\text{res}} = 9.6$ GHz is an indication for the AFO configuration. [Top10, Gub10, Tac10c] Several abrupt changes of the signal strength of the mode at $f_{\text{res}} = 9.6$ GHz for $-13.0 \text{ mT} < \mu_0 H < -6.5$ mT indicate reversal processes of the magnetization of single nanowires or clusters of nanowires. The relative signal strength of main and higher mode amounts to 20% at $\mu_0 H < -6.5$ mT, and increases to 44% at $\mu_0 H < -13.0$ mT. Before, we have extracted the highest degree of order of AFO at $\mu_0 H = -13$ mT by analyzing the main mode behavior. Thus, we take the relatively large signal strength of the higher mode compared to the main mode as a further signature for a high degree of magnetic order.

The mode at $f_{\text{res}} = 9.6$ GHz exhibits a resonance frequency of 2.9 GHz higher compared to the main mode. The obtained frequency difference of 2.9 GHz is consistent with [Top11a], where the frequency difference of the two lowest modes for AFO is calculated to be 2.0 GHz for a nanowire array with slightly larger period of 442 nm. In conclusion, we find the typical mode behavior of the FMO configuration in regime I and III. At the same time, we observe the characteristic modes and field dependencies for the AFO configuration as expected from magnetostatic measurements in regime II. [Top10, Top11a, Din11b] We have found a relatively larger signal strength of the higher mode compared to the main mode to be a signature for a higher degree of order.

For seek of completeness, we focus on the mode with $f_{\mathrm{res}} < 5$ GHz that is almost symmetric with respect to $\mu_0 H = 0$ mT. We find $\frac{\partial f_{\mathrm{res}}}{\partial H} > 0$ ($\frac{\partial f_{\mathrm{res}}}{\partial H} < 0$) for the branch $H > 0$ ($H < 0$). In particular, the two branches follow a $\sqrt{|H|}$ behavior, which is typical for spin wave modes in plain films, see Sec. 5.3.1. We attribute this mode to the IP. The IP mode can be used as a reference to determine the parameters of the unpatterned thin-film material.

6.2.2 FMO and AFO

In the following we focus on FMO and AFO configurations. The mode behavior is analyzed and the results are described by PWM. First, the FMO configuration is investigated, where the sample is saturated at $\mu_0 H_{\mathrm{sat,x}} = -100$ mT, then $\mu_0 H_{\mathrm{ML}} = 5$ mT is applied. In this scenario, an ordered FMO state with the nanowires remaining saturated is achieved. In Fig. 6.3 (a) $Mag(a_{22})$ of sample RH_50 in FMO is presented. For this minor loop a monotonical decrease of the resonance frequency with applied magnetic field is observed. The resonance frequency starts at a value of $f_{\mathrm{res}} = 7.0$ GHz for $\mu_0 H_{\mathrm{ML}} = 5$ mT. This is the characteristic behavior of the mode $n = 0$ as presented in Fig. 2 (c) from [Top11a]. The parameter n counts the number of nodal lines of the spin-precessional amplitude being along the long axis of the nanowires. Also a further mode is detected at an elevated frequency of about 12 GHz which we identify as the $n = 2$ mode[4]. [Tac10c] Focusing on the $n = 2$ mode one can observe two resonances separated by 0.6 GHz. Such a mode

---

[4] Odd modes are not detected due to symmetry reasons of the measurement technique

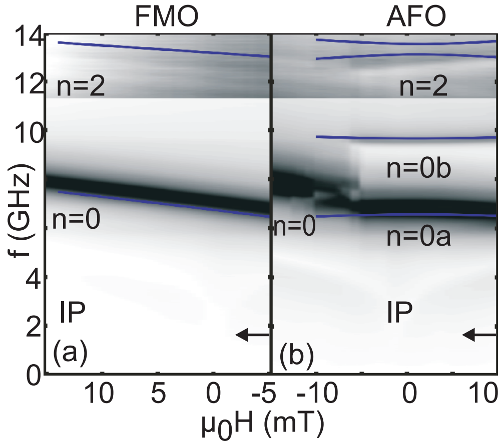

Figure 6.3: $Mag(a_{22})$ obtained for minor loops with (a) $H_{\mathrm{ML}} =$ 5 mT (FMO) and (b) $H_{\mathrm{ML}} = 10$ mT (AFO) obtained on sample RH_50. In (a) the $n = 0$ mode of FMO is observed. In (b) two modes $n = 0$a and $n = 0$b are observed for $\mu_0 H > -6$ mT (AFO) state. For $\mu_0 H < -6$ mT we find a disordered state, and for $\mu_0 H < -13$ mT FMO configuration is recovered. For $f > 11$ GHz the contrast is enhaned to observe the further modes at 12 GHz identified as $n = 2$ in AFO and FMO. Blue lines in (a) and (b) are calculated by PWM. The $n = 0$, $n = 0$a, and $n = 0$b modes are modeled well. There remain discrepancies for the $n = 2$ modes in FMO. In AFO, the $n = 2$a and $n = 2$b modes from PWM are not resolved in measured data. Horizontal arrows indicate the sweep direction.

separation has been presented for a 1D MC with nanowires with alternating width. [Top11a] Though in our case all nanowires exhibit the same width, we assume, that the magnetic parameters are not absolutely equal, as the nanowire array was fabricated in two separate preparation steps.

Second, we discuss 1D MCs where the magnetic history induced the reversal of selected nanowires. Thereby, we intended to create the antiferromagnetic alignment of neighboring nanowires provoking a modified band structure in one-and-the-same MC [Top10, Tac10c]. In Fig. 6.3 (b), $Mag(a_{11})$ is presented where the starting field $\mu_0 H_{\mathrm{ML}} = +10$ mT is chosen such that about 50 % of the nanowires are reversed with respect to the initially saturated state at -100 mT, see Sec. 6.1. The total magnetization is $\mathbf{M}_{\mathrm{tot}} = 0$ for a perfect AFO state. The branches are now subdivided into three regimes as was observed in Refs. [Top10, Din11b]. For -6 mT $< \mu_0 H <$ $+10$ mT, we observe a prominent branch (black) near 6.9 GHz which exhibits a different slope compared to the branch found for the FMO state in Fig. 6.3 (a) which we denote as the acoustic $n = 0$a branch. Such a branch of negative curvature was recently attributed to the AFO state.[Top10] For -13 mT $< \mu_0 H < -6$ mT, we observe stepwise changes (kinks) in the resonance frequency reflecting the reversal of nanowires becoming realigned with the negative field direction. For $\mu_0 H < -13$ mT, the FMO branch of Fig. 6.3 (a) is recovered. We find the same behavior at the further CPW being located 12 μm apart on the same MC (not shown). The $n = 2$ mode is also observed at $f_{\mathrm{res}} = 12.8$ GHz. Moreover, a further mode at $f_{\mathrm{res}} = 9.5$ GHz is detected. Following Ref. [Top10] this mode is identified to be the optical branch $n = 0$b.

We have identified the mode spectrum of the FMO configuration and the AFO configuration. The far-reaching peculiarity of such 1D MC is the unique capability of reprogramming the magnetic configuration from FMO and AFO in one-and-the-same geometric structure. [Top10, Top11a, Tac10c, Gub10] We will exploit this ability in the following sections.

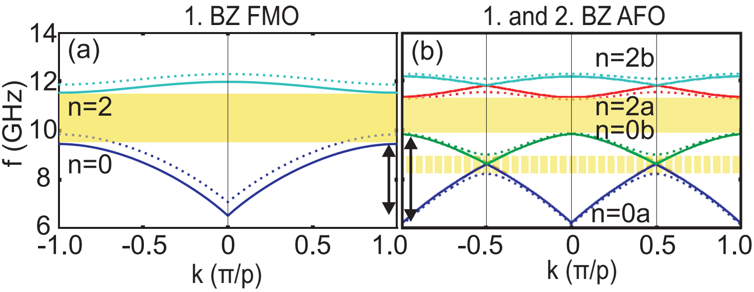

Figure 6.4: PWM data for sample RH_50 in (a) FMO and (b) AFO for $\mu_0 H = 0$ mT (solid) and $\mu_0 H = 10$ mT (dotted). The higher modes n are color coded. For FMO the first Brillouin zone, for the AFO mode the first $\pi/(2p)$ and second $\pi/(p)$ Brillouin zone is depicted. The zeroth and second order modes in (a) and (b) are separated by a band gap (yellow). Strikingly, a further band gap (yellow stripes) appears between $n = 0$a and $n = 0$b in (b) for $H \neq 0$. The band gap is vanishing for $H = 0$. The zeroth order mode band width for $H = 0$ amounts to (a) 2.9 GHz and (b) 3.5 GHz (perpendicular arrows).

6.2.3 Plane Wave Method

To get an insight into the band structure of 1D MCs PWM calculations (see Sec. 2.5) are performed by Dr. M. Krawczyk at Adam Mickiewicz University in Poznán, Poland. PWM provides the dispersion relation depending on the applied field H. In particular, also backfolded modes are addressed. Thus, the measured data in the preceding section is modeled by PWM. The parameters are $M_\mathrm{s} = 1.03$ T, exchange constant $A = 1 \cdot 10^{-11}$ J/m, surface anisotropy $K_\perp = 11.0 \cdot 10^{-4}$ J/m^2, period $p = 300$ nm, and thickness $t = 28$ nm.

Blue lines in Fig. 6.3 (a) and (b) are calculated by PWM. The $n = 0$, $n = 0$a, and $n = 0$b modes are modeled well by the used parameter set. Frequency positions of these modes are described perfectly. There remain discrepancies for the $n = 2$ modes in FMO and AFO. The calculated modes are too high by about 1 GHz. In AFO the two higher modes $n = 2$a and $n = 2$b calculated by PWM are not resolved by AESWS, where only one mode is observed. The relatively larger discrepancies for the higher modes can be explained by taking the fundamental characteristics of these modes into account. For higher order modes $n \neq 0$, the nodal lines introduce phase shifts within the nanowires, that reduce the stray field. [Top11a] Therefore, the stray field interaction is smaller compared to the main mode. Imperfections due to the lithography, e.g. edge roughness, gain influence on higher order modes $n \neq 0$.

The underlying dispersion relations for FMO and AFO are presented in Fig. 6.4 (a) and (b), respectively. Data of the $n = 0$ and $n = 2$ modes are depicted for two field values: $H = 0$ (solid) and $\mu_0 H = 10$ mT (dotted). In (a) the first Brillouin zone (BZ) with Brillouin zone boundary at $\pi/p = 1.05 \cdot 10^7$ rad/μm is shown. A band gap between $n = 0$ and $n = 2$ of 2 GHz is observed. f_res increases for $\mu_0 H = 10$ mT. In (b) also the backfolded modes due to a changed magnetic period, which is $2p$, are included. We depict the first BZ (1. BZ) and the second BZ (2. BZ). The low-lying modes are $n = 0$a, $n = 0$b, $n = 2$a, and $n = 2$b. An additional band gap between $n = 0$a and $n = 0$b can be controlled by H. For $H = 0$ the band gap does not exist. [Top10] In this case the main mode of AFO (1. BZ $n = 0$a and 2. BZ $n = 0$b) and FMO (1. BZ

$n = 0$) dispersion relations are similar. However, the zeroth order mode in AFO ($H = 0$) exhibits a higher bandwidth of 3.5 GHz in comparison to 2.9 GHz in the FMO configuration for the main mode. The magnonic band bandwidth is determined by the dynamic dipolar stray field coupling. [Gub10] Thus, we suggest a higher dynamic dipolar coupling in AFO configuration compared to FMO configuration, which we will discuss in the following.

The higher bandwidth of the AFO configuration is caused by the precessional motion of neighboring nanowires in opposite sense of the magnetization [Top10]: For a *right-handed* oscillation of a nanowire with $+M$, the two neighboring nanowires with $-M$ oscillate *left-handed* ($k = 0$). For an in-phase motion of the in-plane component m_{y} of the neighboring nanowires, the out-of-plane component m_{z} oscillates out-of-phase. Thus, for AFO both components, m_{y} and m_{z}, exhibit an attractive stray field interaction. In contrast, for FMO only m_{y} acts attractively, while m_{z} has a repulsive property. The additional attractive potential of the AFO configuration in contrast to the FMO configuration causes a stronger dynamic dipolar interaction which implies a higher bandwidth.

A second effect caused by the stronger dynamic dipolar interaction is a reduced out-of-plane demagnetizing field at $k = 0$ for AFO compared to FMO. This is consistent with the lower f_{res} for AFO compared to FMO at the Γ point. Along with the stronger dynamic coupling we find a higher f_{res} for AFO at $k = \pi/p$. There, the demagnetizing field in AFO is increased compared to FMO as neighboring nanowires are precessing in-phase in AFO.

In summary, we find PWM to be a well applicable theoretical method that yields results with very good agreement.

6.3 Spin Wave Propagation in a 1D MC

6.3.1 Spin Wave Propagation across Air Gaps

In the following we study spin wave transmission through the 1D MC. To propagate through the 1D MC spin waves have to overcome several air gaps. We emphasize, that a spin wave is only defined *within* ferromagnetic material. By TR-AESWS we can show that spin waves anyway travel across air gaps and discuss the relevant mechanism for this effect. Therefore, we analyze TR-AESWS first in reflection and afterwards in transmission geometry. It is instructive to begin the discussion with data where spin wave eigenmodes of a 1D MC have been detected in the time domain to extract relevant parameters. In a small field regime we are able to investigate the MC without a superposition with a spin wave signal from the IP, though the CPWs are running over the IP. All field values in this section are chosen to minimize the signal contribution of the IP. In Fig. 6.5 (a) we address the FMO state at $\mu_0 H = 2$ mT, and in (b) the AFO state at $H = 0$. The AFO state is achieved by an opposing field H_{ML}, see Sec. 6.1. The excited spin systems exhibit damped sinusoidal oscillations. Importantly, both states provoke similar amplitudes of the voltage signals t_{11}. We analyze the temporal evolution $t_{11}(t)$ in detail by fitting the data by a decaying sinusoidal oscillation [c.f. Eqn. 5.3]. The fitting parameters are the effective relaxation time τ_{eff}, the eigenfrequency f_0, the amplitude $\tilde{C}$, and a constant phase $\tilde{\Phi}$. Best fits using Eqn. 5.3 (red line) are achieved for $f_{0,\mathrm{FMO}} = 7.0 \pm 0.1$ GHz and $\tilde{C} = 2.0 \cdot 10^{-2}$ V, and $f_{0,\mathrm{AFO}} = 6.9 \pm 0.1$ GHz and $\tilde{C} = 2.0 \cdot 10^{-2}$ V for the FMO and AFO configuration, respectively. The spin waves are equally excited in FMO and AFO. The effective relaxation times τ_{eff} amount to $\tau_{\mathrm{eff,FMO}} = 0.62 \pm 0.03$ ns and $\tau_{\mathrm{eff,AFO}} = 0.57 \pm 0.03$ ns, respectively.

We evaluated t_{11} at different fields H. In the field regime $-5 < \mu_0 H < 3$ mT the effective relaxation times for FMO and AFO are nearly constant. $\tau_{\mathrm{eff,AFO}}$ is systematically smaller than $\tau_{\mathrm{eff,FMO}}$. The values of $\tau_{\mathrm{eff,AFO}}$ compared to $\tau_{\mathrm{eff,FMO}}$ differ by about 10%. This might be explained by a contribution from the $n = 0\mathrm{b}$ mode. A similar increase has been evidenced for a superposition of spin wave contributions of the MC and the IP (not shown). There, a clear beating pattern is measured.

In the following we analyze TR-AESWS data in transmission geometry by modeling of spin wave packets.

Figures 6.6 (a) and (b) show the time-dependent transmission signals t_{21} for FMO and AFO, respectively. The oscillation frequencies coincide with the frequencies in reflection geometry. Even at long times, up to 4.5 ns, we detect a magnetic ringing. Thus, the spin wave propagates across a large series of air gaps. In particular,

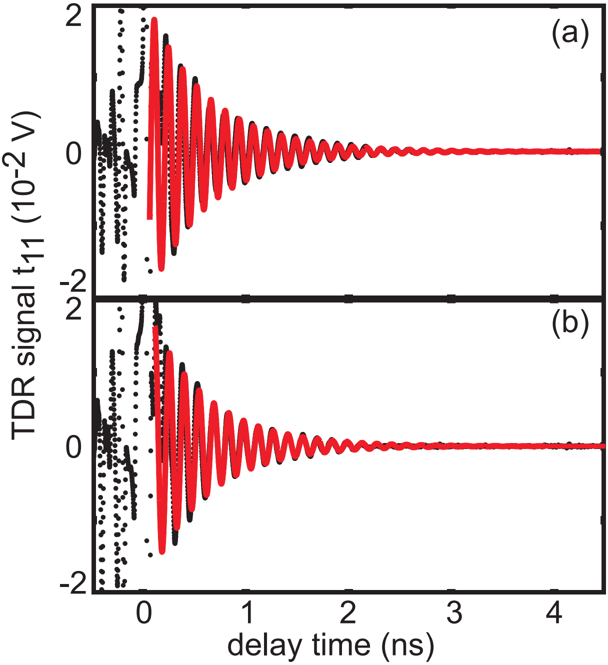

Figure 6.5: TR-AESWS data t_{11} (circles) taken for (a) FMO at $\mu_0 H = 2$ mT and (b) AFO at $H = 0$ on sample RH_50. Both data sets are fitted by a damped sinusoidal oscillation (line) using Eqn. 5.3 for $t \geq 0.5$ ns. The fitting parameters are: (a) effective relaxation time $\tau_{\text{eff,FMO}} = 0.62 \pm 0.03$ ns with an eigenfrequency $f_{0,\text{FMO}} = 7.0 \pm 0.1$ GHz and (b) $\tau_{\text{eff,AFO}} = 0.57 \pm 0.03$ ns with $f_{0,\text{AFO}} = 6.9 \pm 0.1$ GHz.

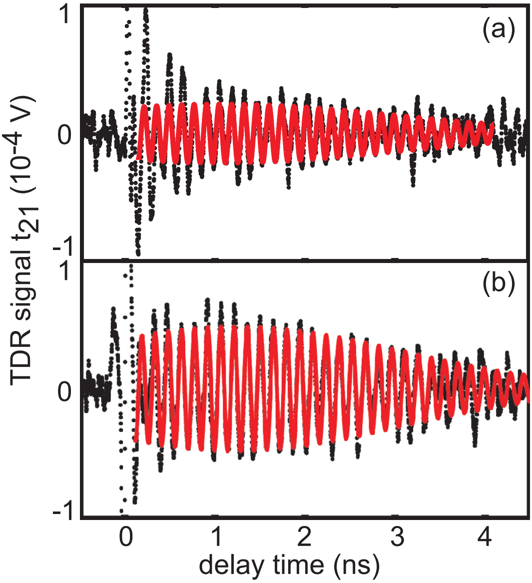

Figure 6.6: TR-AESWS data t_{21} (sample RH_50) taken at the detector CPW in transmission geometry for (a) FMO at $\mu_0 H = 2$ mT and (b) AFO at $H = 0$. We observe ringing up to 4.5 ns, even longer than in Fig. 5.2 on the unpatterned film. The relevant eigenfrequencies are $f_{0,\mathrm{FMO}} = 7.0 \pm 0.1$ GHz and $f_{0,\mathrm{FMO}} = 6.9 \pm 0.1$ GHz when using Eq. 5.4 to fit the data (lines) for $t > 0.5$ ns. Importantly, AFO provokes a transmission signal which is a factor of 1.6 larger than FMO. The determine group velocities for FMO and AFO are equal within the error at $v_\mathrm{g} = 4.0 \pm 0.5$ km/s and $\tau_0 = 1.2 \pm 0.2$ ns.

a significantly higher amplitude is observed in AFO configuration $C_{\mathrm{AFO}} = 5 \cdot 10^{-15}$ V compared to FMO $C_{\mathrm{FMO}} = 3 \cdot 10^{-15}$ V. The transmitted amplitude t_{21} of AFO is larger by a factor of 1.6 if compared to FMO. This is striking as in reflection geometry the excitation amplitudes t_{11} are of the same level.

For a quantitative analysis we consider Eqn. 5.4, which we use to model the transmission signals in AFO and FMO state. f_0 is determined in reflection [c.f. Fig. 6.5], and $k_0 = 0.5\ \frac{rad}{\mu\mathrm{m}}$ is used. Best fitting is obtained for an excitation width of $\delta = 0.38 \cdot 10^{-5}$ m. $\tilde{\Phi}$ is determined in a separate fitting step, as it is an independent parameter. Then we obtain the group velocities $v_{\mathrm{g,FMO}} = v_{\mathrm{g,AFO}} = 4.0 \pm 0.5$ km/s, and the relaxation times $\tau_{0,\mathrm{FMO}} = \tau_{0,\mathrm{AFO}} = 1.2$ ns. The measurement technique allows to extract group velocities for both magnetic configurations, i.e. FMO and AFO. We show SW propagation across about 40 air gaps. Summing up all gaps a distance without magnetic material of 1.8 μm is bridged. In literature this effect is often called *tunneling of spin waves.* Tunneling of spin waves across air gaps has recently been studied in YIG [Sch10], Co-TaZr [Koz09b], and Py [Lan11]. In YIG the propagation of spin waves across a gap with a width of up to 118 μm has been verified. [Sch10] Kozhanov *et al.* found spin waves tunneling across an air gap with a width of 1.2 μm and observed a non-exponential decay of the transmitted spin waves. [Koz09b] Both experiments were performed in BVMSW geometry. In DE geometry, spin wave tunneling has been investigated in dependence on the gap width from 80 nm to 510 nm. [Lan11] The authors found an effective spin wave tunneling for the area between the excitation antenna and the gap forming a resonator for spin waves. In case, that the wavelength is exactly twice of the resonator width, the quantization effect in the resonator increases the excitation efficiency. However strong pinning effects at the gap boundary oppress the precession of magnetic moments and therefore inhibit a SW transmission. Best transmission is found close to a wavelength twice of the resonator width, where the excitation efficiency is still high, but pinning effects are decreased.

These dependencies suggest, that the tunneling is transmitted via the dynamic stray field interaction. The stray field at the gap is caused by the amplitude of the spin wave at the edge. Guslienko *et al.* [Gus02] showed a non-zero amplitude at the edges, though the quantization effect in nanowires was expected to pin magnetic moments at the edges and minimize the precessional amplitudes. For nanowires the nodes of the oscillation are outside the nanowire. This counterintuitive property allows an efficient coupling between nanowires.

6.3.2 Spin Wave Propagation Properties

Verified that spin wave propagation across air gaps is possible, we are now interested in configuration dependent dynamical properties, e.g., the group velocity. Furthermore, we compare the measurement data with PWM data. The three presented samples RH_63, RH_50, and RH_3P differ in edge-to-edge separation: large edge-to-edge separation in sample RH_3P, medium edge-to-edge separation in RH_50, and small edge-to-edge separation in sample RH_63.
In Fig. 6.7 (a) $\Im(a_{21})$ measured on sample RH_50 in the FMO state is presented. Following Sec. 5.3.2 white-black-white contrast is attributed to a SW propagation signal. Propagating SWs are detected for the main mode $n = 0$. An additional signal is found at a frequency about 1.1 GHz higher than the $n = 0$ mode, which we attribute to the higher CPW mode k_1 [c.f. Sec. 3.5]. In Fig. 6.7 (b), $\Im(a_{21})$ measured on sample RH_50 in the AFO state is presented. We detect a transmission signal for the $n = 0$a and the $n = 0$b modes. The IP mode for $f_{\text{res}} < 5$ GHz exhibits a pronounced black-white-black-white contrast (i.e. an oscillatory behavior), which is an indication for a strong SW propagation signal. In contrast, the propagation signal for the MC modes of zeroth order in FMO and AFO exhibit a less pronounced oscillatory behavior, which we attribute to the contribution of the electromagnetic crosstalk. Therefore, we choose the evaluation method for the group velocity v_{g} exploiting the higher modes of the CPW for a systematical evaluation. We use the main mode k_0 and first mode k_1 of the CPW. The data is summarized in Fig. 6.7 (c). We find the maximum group velocity $v_{\text{g}} = 3.8 \pm 0.3$ km/s for RH_63 at $\mu_0 H = -1.5$ mT and decreases for decreasing magnetic. Group velocities of RH_50 for AFO and FMO are included, which amount to $v_{\text{g,FMO}} = 3.0 \pm 0.3$ km/s and $v_{\text{g,AFO}} = 3.3 \pm 0.3$ km/s. Strikingly, v_{g} in AFO is higher than in

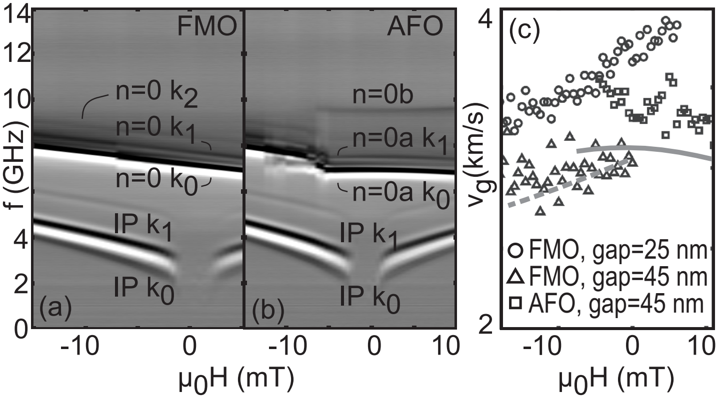

Figure 6.7: $\Im(a_{21})$ measured on sample RH_50 in (a) FMO and (b) AFO. The black-white-black contrast is attributed to propagating spin waves. In (a) the $n = 0$ mode of the 1D MC is observed (and further resonances of the CPW excitation spectrum) for $6 < f < 8$ GHz. In (b) for $6 < f < 8$ GHz the $n = 0$a mode, and at $f \simeq 10$ GHz the $n = 0$b mode is detected. In (a) and (b) for $f < 5$ GHz the charactersitic mode of the IP is detected. (c) Group velocities of samples RH_50 in FMO (crosses) and AFO (squares), and RH_63 (circles) in FMO. Lines indicate calculations by PWM for AFO (solid) and FMO (dashed) for sample RH_50.

FMO. The group velocities are found to differ by 10 %. This reflects the higher bandwidth of AFO due to increased dynamical coupling.

For an edge-to-edge separation of 80 nm in RH_3P no oscillatory transmission signal was observed. From the intensity of SW signal we estimate the group velocity by evaluating the relaxation length ($s_\mathrm{r} = 2.9\ \mu$m) and assuming a constant relaxation time obtained from the attached IP ($\tau_0 = 1.8$ ns). This yields a group velocity of $v_\mathrm{g} = s_\mathrm{r}/\tau_0 \simeq 1.6 \pm 0.6\ \frac{\mathrm{km}}{\mathrm{s}}$.

We conclude, that the edge-to-edge separation has big influence on the group velocities in 1D MCs. We have shown a large group ve-

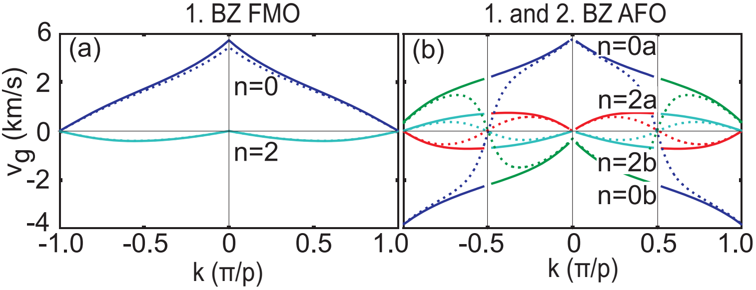

Figure 6.8: PWM data for sample RH_50 in (a) FMO and (b) AFO for $\mu_0 H = 0$ mT (solid) and $\mu_0 H = 10$ mT (dotted). The group velocities for (a) FMO and (b) AFO are shown. The largest group velocity for FMO (AFO) is $v_g = 3.7$ km/s ($v_g = 3.8$ km/s). The calculated group velocity at the 1. BZ boundary in (b) is $v_g = 0$.

locity for a small edge-to-edge separation, and vice versa. A smaller edge-to-edge separation increases the dynamical stray field coupling. There are a few investigations that are directly studying propagation of SWs in magnonic waveguides. We find slightly higher values of the group velocity in 2D MC of $3 < v_\mathrm{g} < 5$ km/s. [Neu11a] Spin wave propagation in zig-zag magnetized nanowires is reported to $v_\mathrm{g} \simeq 2.5$ km/s. [Due12] Thus, nanostructuring provokes a decrease of the group velocity in comparison to plain films (at constant frequency).

PWM Data

Following the band structure calculations by PWM (see Sec. 2.5) from Dr. M. Krawczyk at Adam Mickiewicz University in Poznán, Poland, presented in Fig. 6.4, the relevant group velocities are extracted. From Fig. 6.4 (a) and (b) we evaluate group velocities by Eqn. 2.41. The results are depicted in Fig. 6.8 (a) for FMO and (b) for AFO. The highest group velocity for FMO (AFO) is $v_g = 3.7$ km/s ($v_g = 3.8$ km/s). This finding corresponds to the higher bandwidth in AFO compared to the FMO state. The higher group velocities in the AFO state compared to the FMO state are reproduced as depicted in Fig. 6.7 (c) by gray lines. Note, that there the group velocity is determined by using the eigenfrequencies for $k_0 = 0.5\frac{1}{\mu\mathrm{m}}$ and $k_1 = 1.75\frac{1}{\mu\mathrm{m}}$ consistent with the measurements. We find a maximum group velocity in the AFO state at zero field. The already mentioned control of bandwidth by H in AFO influences the group velocity near the first Brillouin zone boundary characteristically. For $H = 0$ and $k \to \pi/(2p)$ the group velocity amounts to 2.2 km/s. For $H \neq 0$ and $k \to \pi/(2p)$ the group velocity approaches zero.

The group velocities of the presented samples at $H = 0$ are summarized in Fig. 6.9. The dependence of the group velocity on the edge-to-edge separation is calculated by PWM and included in Fig. 6.9. A maximum group velocity is reached for zero edge-to-edge separation and amounts to $v_\mathrm{g} = 5.9\ \frac{\mathrm{km}}{\mathrm{s}}$. Compared to a plain film, the group velocity is smaller by almost a factor of 2.

6.3.3 Reciprocal Damon-Eshbach-type Spin Wave Excitation in a Magnonic Crystal due to a tunable magnetic symmetry

We now investigate the reciprocity of the spin wave excitation. Suprisingly, we find a field-tunable reciprocal excitation in AFO configuration. In plain films the excitation of Damon-Eshbach-type spin waves is found to be non-reciprocal (c.f. Sec. 5.3.2). This depends on the ellipticity of the precessing magnetization. In the following reciprocal excitation of Damon-Eshbach-type spin waves in 1D MCs is presented. This section contains previously published work. [Hub13a] The propagation loss $\frac{a_{21}}{a_{11}}$ of spin waves $k_{21} = -k_{0,\mathrm{CPW}}$ propagating from CPW 1 to CPW 2, and respectively $\frac{a_{12}}{a_{22}}$ of counterpropagating spin waves $k_{12} = +k_{0,\mathrm{CPW}}$ is presented in Fig. 6.10 (a). In the FMO state with $\mu_0 H_\mathrm{sat} = -100$ mT, $\frac{a_{21}}{a_{11}}$ $(\frac{a_{12}}{a_{22}})$ decreases with increasing field with a maximum value of 0.07 (0.04). The FMO state with $\mu_0 H_\mathrm{sat} = +100$ mT exhibits a propagation loss $\frac{a_{21}}{a_{11}}$ $(\frac{a_{12}}{a_{22}})$ of 0.03 (0.07). The values are thus interchanged. Interestingly, in the AFO state $\frac{a_{21}}{a_{11}} = \frac{a_{12}}{a_{22}}$ at $\mu_0 H = 2$ mT. Spin waves k_{21} and k_{12} are equally excited. This reciprocal behavior of spin wave excitation is novel for Damon-Eshbach-type modes. We define the non-reciprocity

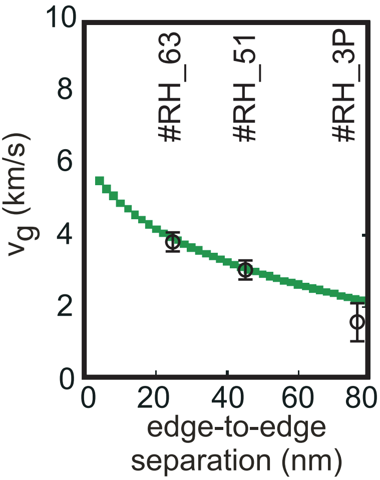

Figure 6.9: Measured group velocities (circles) are presented for different samples (see text). The group velocity of a 1D MC decreases with increasing edge-to-edge separation. The dependence of the group velocity on the edge-to-edge separation is calculated by PWM (squares). The period $p = 300$ nm and the applied field is H=0.

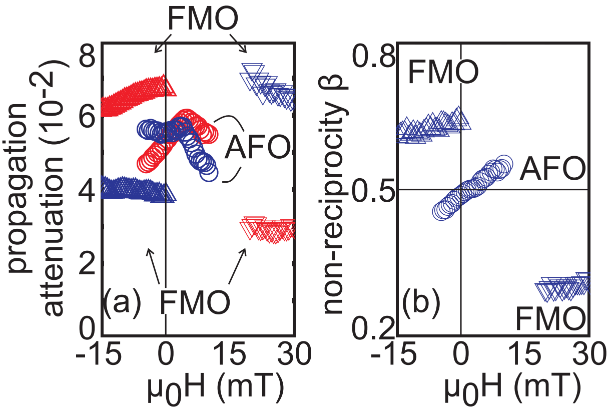

Figure 6.10: (a) Propagation attenuation for counter-propagating SWs in sample RH_50: $\frac{a_{21}}{a_{11}}$ (blue) and $\frac{a_{12}}{a_{22}}$ (red) (FMO with $\mu_0 H_{\rm sat} = -100$ mT: upward triangle, FMO with $\mu_0 H_{\rm sat} = 100$ mT: downward triangle, AFO: circle). (b) Non-reciprocity parameter β. FMO with $\mu_0 H_{\rm sat} = -100$ mT: upward triangle, FMO with $\mu_0 H_{\rm sat} = 100$ mT: downward triangle, AFO: circle. $\beta = 0.5$ indicates reciprocal excitation and is achieved in the AFO state. The field step is $\mu_0 \Delta H = 0.5$ mT.

parameter β by Eqn. 5.11

$$\begin{aligned} a_{21} &= \beta a_{11} \exp^{-\frac{s}{s_\mathrm{r}}} \\ a_{12} &= (1-\beta) a_{22} \exp^{-\frac{s}{s_\mathrm{r}}} \\ \Rightarrow \beta &= \frac{\frac{a_{21}}{a_{11}}}{\frac{a_{21}}{a_{11}} + \frac{a_{12}}{a_{22}}}. \end{aligned} \tag{6.1}$$

$\beta = 0.5$ indicates reciprocal characteristics. For FMO, Eqn. (5.11) yields $\beta_\mathrm{FMO} = 0.7$ for negative saturation and $\beta_\mathrm{FMO} = 0.3$ for positive saturation, i.e. $\beta \neq 0.5$ consistent with Refs. [Dem09, Fal12]. For AFO, however, $\beta_\mathrm{AFO} = 0.5$ at $\mu_0 H = 2$ mT. For both increasing and decreasing H β is found to deviate from 0.5. But values of β are still different from FMO data.

The non-reciprocal behavior for the FMO state can be explained following Demidov *et al.* [Dem09] who investigated counter-propagating DE modes in a homogeneous material with $\mathbf{M}_\mathrm{tot} = \mathbf{M}_\mathrm{s}$. The modes exhibited non-reciprocal characteristics because of partly counteracting components h_x and h_z of the rf magnetic field of the emitter antenna. Both components h_x and h_z provide torque contributions for SW excitation but have opposite phase relations at the opposite sides of the antenna. For in-phase (out-of-phase) relation the corresponding torques enhanced (reduced) the precessional amplitude for SWs propagating to one (the other) direction. For plain films, this antenna-induced non-reciprocity is expected to increase with decreasing $\mathbf{M}_\mathrm{tot} = \mathbf{M}_\mathrm{s}$. An artificially tailored material with $\mathbf{M}_\mathrm{tot} = 0$ such as a 1D MC in the AFO state has not yet been addressed. We observe that, strikingly, the non-reciprocity vanishes under such a condition ($\beta = 0.5$). We attribute this peculiar observation in the AFO state to a balanced configuration, i.e, the internal field in each nanowire is the same and amounts to $H_\mathrm{int} = 0$ [Top11a]. Considering the long wavelength of the SWs ($\lambda \gg p$), an equal number of positively and negatively magnetized nanowires are excited such that in-phase and out-of-phase torques through h_x and h_z average out in the relevant unit cells of the MC. Excitation on both sides of the CPW becomes similar. As the long wavelength limit turns out to be crucial, we denote the reciprocal property as a metamaterial property for spin waves. For the ideal 1D MC, $H_\mathrm{int} = 0$ is valid for $H = 0$. For real 1D MCs, it was reported that residual stray fields needed to be considered and compensated via a small H [Top10, Din11a]. Consistently, we observe $\beta = 0.5$ at $\mu_0 H = 2$ mT. For other H, the AFO state is not balanced and H_{int} is known to vary periodically throughout the MC [Top11a]. Then, the excitation of the two nanowires in the unit cell is no longer fully symmetric [Top11b, Top11a]. Fig. 6.10 (b) shows that the non-reciprocity is recovered for such unbalanced AFO states, allowing for a precise field control of the artificially-created reciprocal SW excitation.

6.3.4 Spin Wave Relaxation

Transforming Eqn. 5.11 we determine the relaxation length

$$s_r = -s/ln(\frac{a_{21}}{a_{11}\beta}).$$

In Fig. 6.11 (a) the calculated s_{r} for the zeroth order modes are summarized for RH_50 in AFO and FMO. We observe a maximum $s_{\text{r}} = 5.3\ \mu$m for $H \simeq 0$ in FMO that is slightly decreasing for decreasing field. For AFO configuration we find a relaxation length of $s_{\text{r}} = 5.6\ \mu$m at $\mu_0 H = 4$ mT, which is larger compared to the FMO value. In particular s_{r} in the AFO state is nearly symmetric around $\mu_0 H = 4$ mT, i.e. $s_{\text{r}}(4 \text{ mT} - \mu_0\text{H}) = \text{s}_{\text{r}}(4 \text{ mT} + \mu_0\text{H})$. A reduction of 8% is observed while changing the field by 6 mT, which is large in contrast to less than 1% variation in the FMO configuration. In the reoriented state (FMO) for $\mu_0 H < -13$ mT s_{r} recovers the FMO state.

First we focus on the long relaxation lengths in AFO and FMO, both with $5.0\ \mu\text{m} < \text{s}_{\text{r}} < 5.6\ \mu\text{m}$. The relaxation length is governed by two fundamental parameters: the group velocity v_{g} and relaxation time τ_0. Using $s_{\text{r}} = v_{\text{g}}\tau_0$ [c.f. Eqn. 2.42], one can calculate τ_0. Therefore, we expect a longer s_{r} in AFO compared to FMO configuration due to the larger allowed miniband width and therefore v_{g} [Fig. 6.4]. We compare the obtained values with the plain film value $s_{\text{r,pf}} = 6.7\ \mu$m at $\mu_0 H = 100$ mT (see Sec. 5.3.2), where the group velocity is similar. For AFO (FMO) s_{r} is smaller by 16% (22%) compared to the plain film value. Therefore, we suppose that the intrinsic relaxation time τ_0 is smaller, i.e., the intrinsic damp-

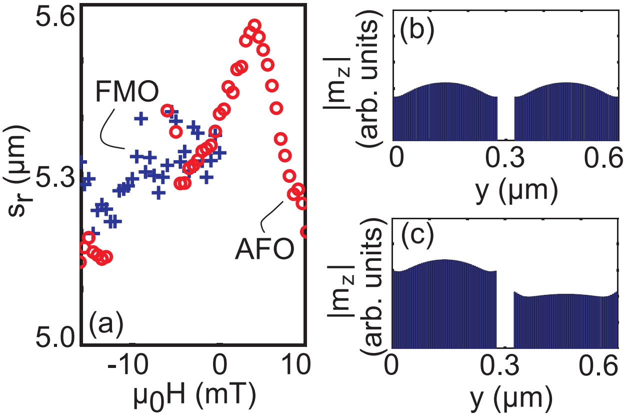

Figure 6.11: (a) Relaxation length s_r from sample RH_50 for FMO (crosses) and AFO (circles). FMO is found to exhibit a linear dependence, AFO exhibits a maximum at $\mu_0 H =$ 4 mT. (b) and (c) Spin wave amplitudes averaged over time $|m_z(y)|$ for FMO and AFO at $\mu_0 H = 10$ mT. $|m_z(y)|$ is symmetric (asymmetric) in FMO (AFO).

ing is larger. To damp spin waves, angular momentum needs to be transferred from the spin system to the lattice. In metallic ferromagnets two main contributions are distinguished, i.e., a direct and indirect contribution [Sta09, Ari99, Fae11]. First, we consider the direct contribution. Spin precession is argued to induce electron-hole pairs via intra- and interband transitions caused by the spin-orbit interaction. Scattered at e.g. defects and phonons, the electron-hole pairs transfer angular momentum to the lattice. At room temperature the electron scattering time is short, and interband transitions are believed to dominate the damping in permalloy [Fae11]. It is unlikely that our patterning on the few 100 nm length scale changes the electronic states being relevant for the direct damping. Changes have so far been discussed for nm-sized magnets [Koe07]. Second, we consider the indirect contribution due to magnon-magnon scattering. Here the SW spectrum is relevant. Due to our patterning, SWs with k transverse to the long axis experience forbidden frequency gaps. A discrete spectrum is expected to alter magnon-magnon scattering where both momentum and energy conservation are to be fulfilled. A similar argument was used to explain long relaxation times found in an individual nanomagnet [Sch08b]. For a 2D MC formed by an antidot lattice the scenario is different. The SW spectrum exhibits dispersive branches in the different lattice directions allowing to fulfil momentum and energy conservation in scattering events [Neu11b]. There, unintentional edge roughness introduced via nanopatterning might even favor magnon scattering. On an antidot lattice, small relaxation times were observed for distinct field orientations [Neu10]. Also in 1D MC unintentional edge roughness is suggested to favor magnon scattering, which yields a slightly smaller relaxation time compared to an unpatterned thin film.

In the following we discuss the field dependence of the relaxation length in AFO configuration. In contrast to FMO a pronounced field dependence of $s_{\mathrm{r}}(H)$ is detected, that is not explained by the variation of the group velocity. Following Eqn. 2.42 the relaxation length should be proportional to the measured group velocity shown in Fig. 6.7 (c), which is not observed. Micromagnetic simulations give an insight in this peculiar behavior. The spin wave amplitudes $|m_z(y)|$ for FMO and AFO configurations at $\mu_0 H = 10$ mT are depicted in Fig. 6.11 (b) and (c), respectively. In FMO, neighbor-

ing nanowires exhibit an equal spin precession amplitude. For AFO configuration, nanowires with positive and negative magnetization exhibit equal amplitudes only, when the internal field is equal. In an ideal system this is the case at 0 mT. For $H \neq 0$ the internal fields vary, which results in asymmetric amplitude profiles in AFO configuration, i.e. $|m_z(y)|$ from a nanowire with $M \uparrow\uparrow H$ decreases, whereas $|m_z(y)|$ from the nanowire with $M \uparrow\downarrow H$ increases.
A further possible scenario for the strong field dependence is the scattering of spin waves at inhomogeneities, e.g., single nanowires, where the magnetization points not in the direction as expected from a pure AFO configuration. Assuming such a non-ideal AFO configuration we suggest, that a non-periodic magnetization profile might change the transmission characteristic of the spin waves. Further measurements are necessary to get a deeper insight.

6.4 Conclusion

In conclusion, a 1D MC is an exciting partition of magnonics due to its unique capability to control the magnetic configuration by the magnetic history. In this chapter we have investigated two different magnetic configurations, the FMO and AFO configuration. By MFM and MOKE we have verified the magnetic configuration, and we have studied its complex magnetodynamic response. We have compared spin wave properties of the FMO configuration with the AFO configuration and have described the band structure by PWM data. Using TR-AESWS we have shown the propagation of spin waves across several air gaps. The stray field couples the single nanowires and supports the spin wave propagation even outside magnetic material. Furthermore, for the 1D MC in AFO configuration we have found exceptional properties. Analyzing of SW propagation, we discovered the reciprocal excitation of DE-type spin waves in the AFO configuration. We denote the reciprocal property as a metamaterial property for spin waves, as we identified the long wavelength limit to be crucial. The reciprocal SW excitation is promising for coherent control on the nanoscale and for devices where counterpropagating DE modes are manipulated, e.g. in a SW interferometer device. The MC in the balanced AFO state is considered as an optimum material

for a spin wave bus, where equal spin wave propagation is desired in both directions [Khi05].
Finally, we found an unexpected relaxation behavior in the AFO state that waits for a fundamental explanation.

7 A One-dimensional Magnonic Crystal with Canted Magnetization

In this chapter the magnetic field is applied *perpendicularly* to the nanowires, i.e., in y direction. Investigations on ferromagnetically ordered arrays of nanowires with a perpendicularly applied field have been reported in literature [Zig07, Tac09]. A theoretical study about oblique applied fields on 1D MC starting from a saturated state (FMO) has been published by Nguyen and Cottam. [Ngu07, Ngu11] A comparison of the spin wave modes in a ferromagnetically *and* antiferromagentically ordered array of nanowires with a perpendicularly applied field is so far missing. We investigate experimentally the saturated FMO state with an oblique, applied field. Additionally, we take one step further and also study the AFO state. The measurements are performed on sample RH_50 applying the field by $\eta = 90°$. The measured data are modeled by micromagnetic simulations to obtain a deeper insight. A magnetic field applied perpendicularly to the long axis of the nanowires is interesting as the static and dynamic magnetization is inhomogeneous across the nanowire array. [Ngu07]

7.1 Magnetostatic Behavior

For a magnetostatic analysis, micromagnetic simulations, see Sec. 2.6, are performed. The period and edge-to-edge separation from sample RH_50 are used as simulation parameters. We apply the saturation field of $\mu_0 H_{\mathrm{sat}} = +100$ mT parallel to the nanowires. Then, the field is decreased to $\mu_0 H = 0$ mT yielding the FMO state. For AFO the ground state was imposed by applying $\mu_0 H = -10$ mT. Starting from $\mu_0 H = 0$ mT the magnetic field was applied perpendicular to the nanowires, i.e., parallel to the y-axis.

For FMO, the in-plane orientation of $\mathbf{M}$ at characteristic field values is depicted in Figs. 7.1 (a)-(d). In Fig. 7.1 (a) $\mu_0 H = 3$ mT at $\eta =$

90° is applied, i.e., $\mu_0 H_\mathrm{y} = 3$ mT, and a homogeneous magnetization pointing in x direction is observed. In Fig. 7.1 (b) $\mu_0 H_y = 50$ mT is applied. The magnetization is inhomogeneously canted. The spins in the center region are already rotated by $\psi = 63°$. ψ is measured with respect to the long axis of a wire. In contrast, the spins at the nanowire's edge region are rotated by only $\psi = 41°$. Increasing the field to $\mu_0 H = 60$ mT the magnetic moments at the nanowire center are rotated to $\psi = 86°$, and the edge magnetization further rotates to $\psi = 60°$ [c.f. 7.1 (c)]. A homogeneous, canted $\mathbf{M}(\mathbf{r})$ ($\psi = 90°$) of the nanowires is achieved by an applied field of $\mu_0 H = 200$ mT [c.f. 7.1 (d)].

The magnetostatic behavior of AFO is depicted in Figs. 7.1 (e)-(h). The analysis is performed in the same manner as for FMO, in particular the field values are the same. We find a similar behavior for an equivalent applied field. However, the x-component of $\mathbf{M}$ in neighboring nanowire is antiparallel as shown in Figs. 7.1 (e)-(g). A homogeneous $\mathbf{M}(\mathbf{r})$ ($\psi = 90°$) is achieved for $\mu_0 H = 200$ mT [c.f. 6.1 (h)].

Canting Mechanism

The magnetization $\mathbf{M}(y)$ across the nanowire is observed to be inhomogeneous. A similar behavior has been evidenced for a single nanowire, i.e., without interaction with neighboring nanowires. [Top09, Due12, Ngu07] There, the field is also applied perpendicular to the nanowire. Two separate switching fields are found, one at lower field value where $\mathbf{M}$ in the center region of the nanowire follows the applied field. At a higher absolute field value $\mathbf{M}$ from the edge region reorients parallel to the applied field. This peculiar behavior allowed to form nanochannels with high spin wave propagation in Ref. [Due12].

For an array of nanowires the reorientation of $\mathbf{M}(y)$ is found to be similar. Due to the strong dipolar coupling within the nanowire array the switching events of center and edge region are more correlated in contrast to single nanowires, where the switching events of center and edge region are decoupled.

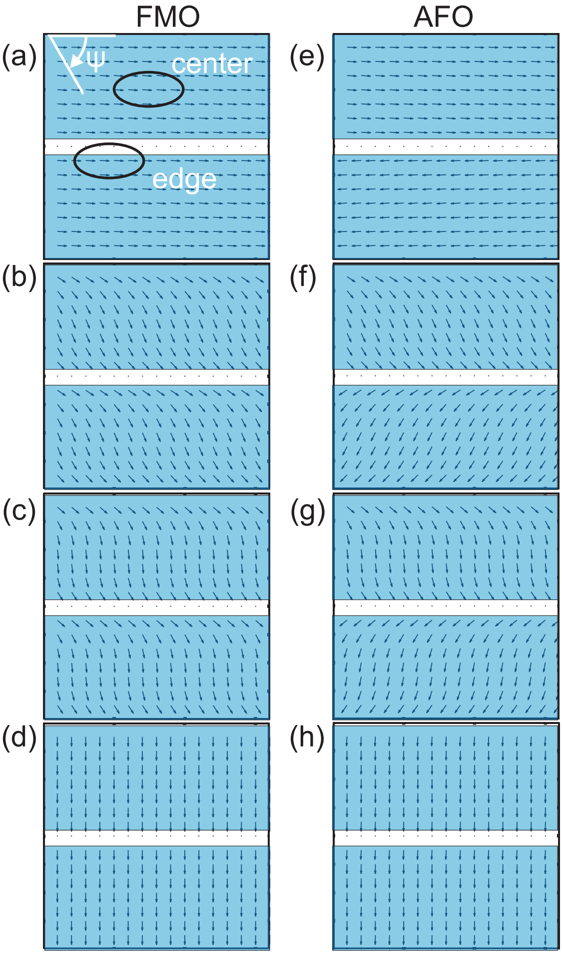

Figure 7.1: Micromagnetic simulation of two neighboring nanowires residing inside an array (blue). The orientation of magnetic moments (arrows) averaged over many simulation cells is shown for different field values with $\eta = 90°$ (a) $\mu_0 H = 3$ mT, (b) $\mu_0 H = 50$ mT, (c) $\mu_0 H = 60$ mT, and (d) $\mu_0 H = 200$ mT starting from the FMO ground state. Corresponding field values are shown in (e)-(h) for the AFO ground state. The angle ψ describes the angle of the magnetization with respect to the x axis. The *center* and *edge* regions are marked.

7.1.1 Experimental Results

In the following we perform FR-AESWS, see Sec. 3.2.2, in both magnetic states FMO and AFO. The field is applied in positive x direction to obtain a saturated state. For FMO we use $H_{\mathrm{ML}} = 0$, for AFO $H_{\mathrm{ML}} = -10$ mT and afterwards we reduce H to zero. Starting from $H = 0$ the field is increased up to $H = 100$ mT with $\eta = 90°$. In Fig. 7.2 $Mag(a_{11})$ is depicted for $\eta = 90°$ in two magnetic states, (a) FMO and (b) AFO. In the FMO state for $H = 0$ the $n = 0$ mode exhibits a resonance frequency of $f_{\mathrm{res,0}} = 7.0$ GHz. Two higher modes are detected at $f_{\mathrm{res}} = 12.0$ GHz and $f_{\mathrm{res}} = 12.5$ GHz. In the AFO state for $H = 0$ the $n = 0\mathrm{a}$ mode exhibits a resonance frequency of $f_{\mathrm{res,0a}} = 6.8$ GHz. An additional strong mode is detected at $f_{\mathrm{res,0b}} = 9.6$ GHz. Two higher frequency modes are detected, a weak one at $f_{\mathrm{res,2a}} = 12.0$ GHz and strong one at $f_{\mathrm{res,2b}} = 12.6$ GHz. For $\mu_0 H > 30$ mT a mode at higher frequency is detected in both magnetic states, which we attribute to the fourth order mode. A resonance at $f_{\mathrm{res}} = 8.1$ GHz is observed for both magnetic states, it is attributed to a higher wave vector excited by the CPW and not discussed in further detail here. For increasing field f_{res} decreases up to a critical field $H_{\mathrm{anis,n}}$, which depends on the mode number n. The lowest frequency $f_{\mathrm{res}} = 3.4$ GHz is obtained for the $n = 0$ mode. For increasing n the critical field value $H_{\mathrm{anis,n}}$ increases (dashed line in Fig. 7.2). The anisotropy fields for the FMO state are $\mu_0 H_{\mathrm{anis,0}} = 57$ mT, $\mu_0 H_{\mathrm{anis,2}} = 69$ mT, and $\mu_0 H_{\mathrm{anis,4}} = 75$ mT. The anisotropy fields for the AFO state are $\mu_0 H_{\mathrm{anis,0}} = 60$ mT, $\mu_0 H_{\mathrm{anis,2}} = 71$ mT, and $\mu_0 H_{\mathrm{anis,4}} = 80$ mT. For $H > H_{\mathrm{anis,n}}$ the resonance frequency f_{res} increases monothonically. Furthermore, a monothonically increasing mode over the whole magnetic field regime is detected. We attribute this mode to the backward volume magnetostatic mode of the IP, which is not discussed in detail.

Micromagnetic simulations are performed for $k = 0$. The out-of-plane component of $\mathbf{m}$ is analyzed. The in-plane component of $\mathbf{m}$ is also analyzed and exhibits equivalent behavior (not shown). In Fig. 7.3 spin wave resonances for various field values are depicted. In FMO four modes are observed, in AFO there are eight modes due to the backfolding at the magnetic period $2p$, where p is the geometric period. This is similar to Fig. 6.4 obtained by PWM in

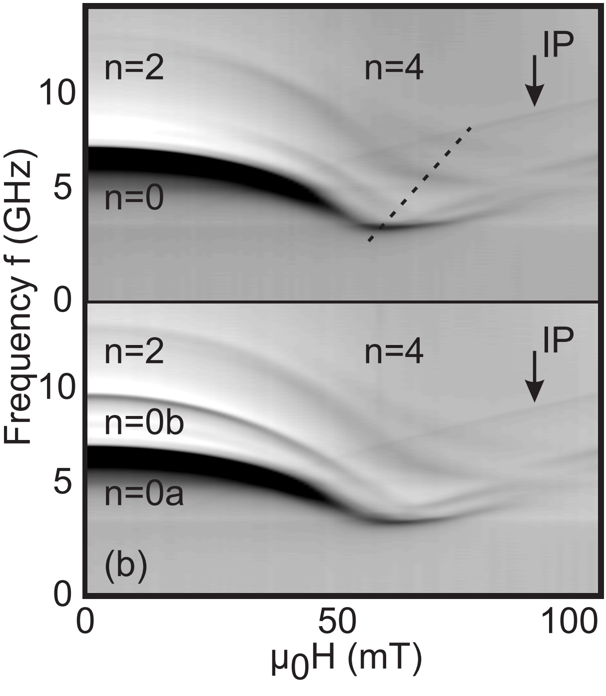

Figure 7.2: (a) The spin wave resonances measured via $Mag(a_{11})$ are depicted for $\eta = 90°$ for a MC in the FMO state. Several MC modes are detected, and also a Backward Volume Magnetostatic Mode from the IP is observed (arrow). The dashed line connects frequency minima. (b) The spin wave resonances in $Mag(a_{11})$ are depicted for $\eta = 90°$ for a MC in the AFO state.

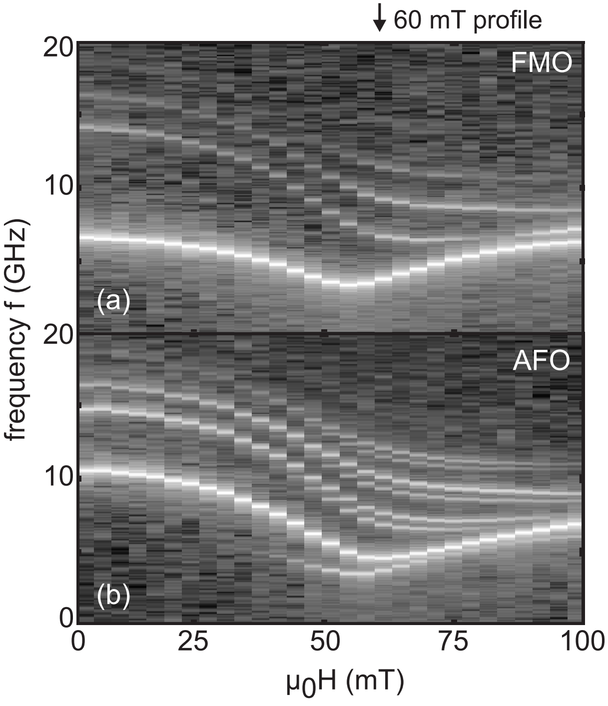

Figure 7.3: Corresponding micromagnetic simulations to Fig. 7.2. Spin wave resonances for (a) FMO state and (b) AFO state. The perpendicular arrow shows the analyzed spectrum for Fig. 7.4. Here, white color indicates a resonance.

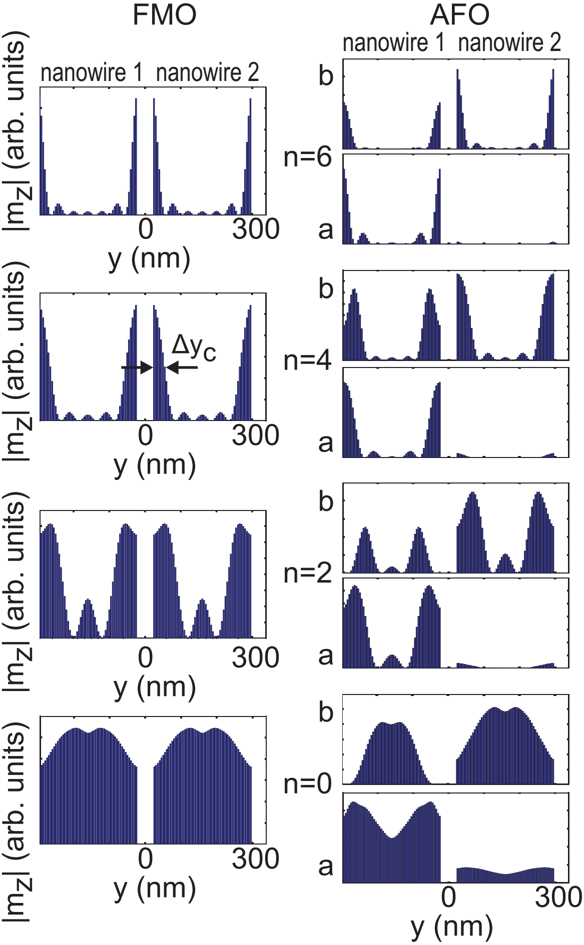

Figure 7.4: Micromagnetical simulations of the spin wave amplitudes averaged over time $|m_z(y)|$ across two nanowires with $\mu_0 H = 60$ mT corresponding to Figs. 7.1 (c) in FMO and (g) in AFO. In each figure two neighboring nanowires are plotted. The FMO eigenmodes $n = 0,\ 2,\ 4,$ and 6 and the corresponding pairs of AFO eigenmodes (a and b) are presented. Δy_{c} indicates the lateral confinement of the edge modes.

DE geometry, where the AFO state exhibits twice as many modes as in the FMO state. Similar behavior is found for pairs of modes for $\mu_0 H > 45$ mT. Micromagnetic simulation in FMO state shows good agreement with the measurement in Fig. 7.2. In the AFO state the low frequency mode is not observed for $\mu_0 H < 43$ mT. The backfolded mode $n = 0b$ is observed in measurement and is in agreement with the simulated data. However, in experiment we observe only one resonance at the higher frequency modes for $\mu_0 H > 30$ mT in contrast to the simulated data, where pairs of resonances are detected for the whole field regime. The overall characteristic, i.e. the field dependence of the modes, fits the measured data well for $\mu_0 H < 80$ mT. For $\mu_0 H > 80$ mT the measured field dependency of the modes differs from the simulated one in FMO state as well as in AFO state. While the mode of second order in the measurement is crossing with the zeroth order mode, in simulated data the second order mode stays above the main mode. For the similar sample geometry neither a mode crossing is found as depicted in Fig. 4 from [Ngu11].

The characteristic field values $H_{\mathrm{anis,n}}$ in simulation and experiment agree perfectly. In particular, the shift to higher absolute values of $H_{\mathrm{anis,n}}$ in the AFO compared to FMO state is reproduced. The good agreement allows us to explore the microscopic origin and analyze the spin wave mode profiles. At a field value of $\mu_0 H = 60$ mT [c.f. Fig. 7.1 (c)] the mode profiles, i.e. spin wave amplitudes, are depicted for the four most intense modes in FMO state and the eight most intense modes in AFO state. In FMO state we present the spin wave amplitudes averaged over time $|m_z(y)|$ of the modes with the corresponding resonance frequencies in Fig. 7.4 (a): $f_{0,n=0} = 4.2$ GHz, $f_{0,n=2} = 6.6$ GHz, $f_{0,n=4} = 9.1$ GHz, and $f_{0,n=6} = 11.2$ GHz. The eigenmode $n = 0$ exhibits a spin wave amplitude across the whole nanowire, with two symmetric maxima shifted with respect to the center by 33 nm. For the first higher mode $n = 2$ we observe a similar behavior, with two maxima symmterical with respect to the center at a distance of 98 nm. A different behavior is detected for the two higher modes $n = 4$ and $n = 6$. The maxima of the oscillation amplitudes are confined at the edges of the nanowire, whereas in the center of the nanowire, there is only little amplitude. We define the maximum position y_{m} and the position y_{hm}, where the amplitude has dropped to half of the maximum. Then, the lateral confinement $\Delta y_\mathrm{c} = y_\mathrm{m} - y_\mathrm{hm}$ amounts to $\Delta y_{\mathrm{c},6} = 14$ nm for $n = 6$ and $\Delta y_{\mathrm{c},4} = 28$ nm for $n = 4$.

In AFO state we present the spin wave amplitudes averaged over time $|m_z(y)|$ of all eight modes from Fig. 7.4 (b). The main difference between FMO state and AFO state is the non-symmetric amplitudes of neighboring nanowires in AFO state. This is similar to Fig. 6.11. While in FMO neighboring nanowires exhibit identical $|m_z(y)|$, in AFO one nanowire exhibits an increased $|m_z(y)|$ compared to the neighboring nanowire. Within one pair of eigenmodes (index a and b) a strong spin wave amplitude is found in one nanowire for each eigenmode a, and in the other nanowire for b. Similar to the FMO state the maximum of the spin wave amplitude concentrates at edge region of the nanowires for higher frequency modes. For $n = 6b$ the lateral confinement amounts to $\Delta y_{\mathrm{c},6\mathrm{b}} = 16$ nm.

A lateral confinement, also called pinning, has also been found by Nguyen and Cottam in a single Py stripe by Hamiltonian-based calculations. [Ngu07] They have presented the main mode exhibiting a strong lateral confinement, when a field $H \gg H_\mathrm{c}$ is applied. This is in agreement with our data at $H \gg H_\mathrm{c}$ (not shown). The pinning is attributed to significanlty inhomogeneous magnetization of edge and center region.

7.1.2 Mode Softening

The characteristic behaviour of the spin wave resonance frequency f_res that is decreasing initially with increasing H, passing through a minimum before increasing again at larger H, is known from ferromagnets exhibiting a shape anisotropy. The applied field exerts a torque on the magnetization. The magnetization is canted with respect to the edges. The demagnetizing field $\mathbf{H}_\mathrm{dem} = -\hat{\mathbf{N}}\mathbf{M}$ [c.f. Eqn. 2.10] is antiparallel with the applied field and reduces the effective field H_eff, which yields a smaller resonance frequency. This mode softening has been observed in single stripes [Bai03a, Top09, Due12]. There, experiments have been done with $k \parallel y$ and $H \perp y$. In contrast, we address k and H being perpendicular to the nanowire (i.e. $k \perp y$ and $H \perp y$). Importantly, this configuration improves the sensitivity for modes with $\mathbf{M}(\mathbf{r}) \parallel y$ due to a larger torque, which allows us even to observe the $n = 4$ mode. The field positions $H_{\mathrm{anis,n}}$ of the frequency minima increase with the order n of the spin wave mode [c.f. dashed line in 7.2], which is modeled by micromagnetic simulations. The effect is described theoretically by Nguyen and Cottam. [Ngu11] They attribute the increasing field value of the dip for higher frequency spin waves to the different reorientation of the magnetic moments at the nanowire edges in contrast to the center region.

7.1.3 Conclusion

Applying the magnetic field perpendicularly to the long axis of the 1D MC allows the investigation of the complex demagnetization and reorientation of the magnetic moments. In particular the setup geometry improves the sensitivity of higher-order modes. Our measurements and simulations verify the effects of reorientation of the magnetic moments on the spin wave modes found by Nguyen and Cottam. [Ngu07, Ngu11] In particular the strong lateral confinement of a few 10 nm is striking. In [Due12] a small angle of a few degrees canted with the y-axis forms a zig-zag magnetization in a nanowire, which yields spin wave channels with a lateral confinement of 60 nm width in the *center* region of the nanowire. Combining both effects, we suggest to control the lateral position of the resonant area within the nanowire by the applied magnetic field. Thereby, the coupling via in-plane and out-of-plane components of the nanowires can be controlled and investigated.

8 A Semitransparent Mirror for Spin Waves

The control of amplitudes and phases of propagating spin waves (SWs) is essential for magneto-logics using SWs. [Sch08a] Different local inhomogeneities of magnetic properties have been investigated, such as e.g. a geometric defect [Fil12], an interface [Neu11b], the core polarization in nanomagnet chains [Bar10], and a local magnetic field creating a potential barrier at which reflection, transmission, and tunneling of SWs occurred [Neu09a, Dem04]. At the same time, investigations on one-dimensional (1D) magnonic crystals (MCs) consisting of interacting nanostripes have shown artificially tailored SW band structures that depend on the magnetic state [Top10, Tac10c, Din11b, Hub13a]. For further advancements in magnonics [Kru10, Len11] one aims at controlling spin waves with individual nanoscopic magnets [Her04, Au12]. In this chapter we investigate the control of SW propagation using a deep *subwavelength* magnetic element.

This chapter contains previously published work. [Hub13b]

8.1 Experimental Results

In experiments on different MCs we detected reduced amplitudes of propagating SWs when individual nanowires switched from the parallel to the anti-parallel state. Indications for this effect have been already observed for SW propagation in MCs where the kink at $\mu_0 H = -7$ mT in Fig. 6.7 may be attributed to a single nanowire or several nanowires with anti-parallel magnetization in the propagation path of the SW. There is no corresponding sign in the reflection data in Fig. 6.3. To investigate this phenomenon in detail we prepared a specific sample which will be described in the following.

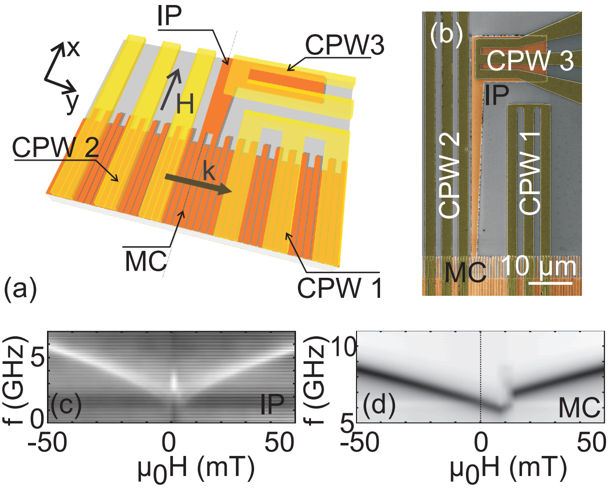

Figure 8.1: (a) Sketch of the sample design. It consists of a permalloy nanowire array with $p = 300$ nm and an edge-to-edge separation of 45 nm. Two of the nanowires are connected to an IP to decrease the switching field. On top three CPWs are integrated with a signal line width of 2.0 μm. (b) Scanning electron microscopy image of the sample, with two integrated CPWs for AESWS and a further one for detection of the magnetization switching of the IP. (c) Signal $Mag(a_{11})$ and (d) $Mag(a_{33})$ from CPW3 and CPW1 detecting the IP and the MC, respectively. The reversal of the MC (IP) is observed at $-12 \pm 1 < \mu_0 H < -8 \pm 1$ mT ($\mu_0 H = 1 \pm 1$ mT).

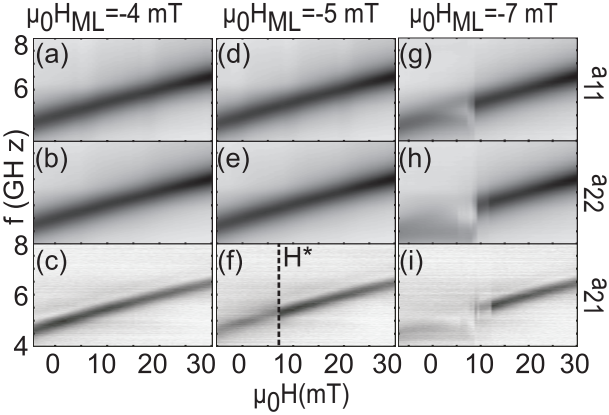

Figure 8.2: (a)-(c) AESWS spectra obtained in a minor loop with $\mu_0 H_{\mathrm{ML}} = -4$ mT addressing the FMO state: (a) $Mag(a_{11})$, (b) $Mag(a_{22})$, and (c) $Mag(a_{21})$. (d)-(f) Spectra obtained in a minor loop with $\mu_0 H_{\mathrm{ML}} = -5$ mT: (d) $Mag(a_{11})$, (e) $Mag(a_{22})$, and (f) $Mag(a_{21})$). In the transmission signal $Mag(a_{21})$, the signal strength varies abruptly at $\mu_0 H^* = 7.5$ mT, which is attributed to a change of the magnetic ground state $\mathbf{M}(\mathbf{r})$. In the reflection signal $Mag(a_{ii})$ no abrupt change is observed. (g)-(i) Spectra obtained in a minor loop with $\mu_0 H_{\mathrm{ML}} = -7$ mT addressing a disordered state: (g) $Mag(a_{11})$, (h) $Mag(a_{22})$, and (i) $Mag(a_{21})$. Abrupt changes are observed in all three graphs.

Experimental Setup

This sample contained an injection pad for domain walls attached to the nanostripes located intentionally between two CPWs. Thereby the propagation properties were directly addressed. The sample exhibited a period $p = 300$ nm, where the edge-to-edge separation (air gap width $\hat{\eta}$) was 45 nm, the thickness of 40 nm, and the length of the wires amounted to about 300 μm. The nanowires have been structured by electron beam lithography (see Sec. 4.2) and are made from of evaporated permalloy. Here, two selected nanostripes (next-nearest neighbors) are connected to an injection pad (IP) for domain walls in order to control their magnetic state independently from the remaining MC. The MC is isolated by 8 nm thick Al_2O_3 deposited by atomic layer deposition. On top three coplanar waveguides (CPW1 - CPW3) [Fig. 8.1 (b)] are integrated by electron beam lithography and evaporation of Cr and Au with a width of the signal and ground lines of 2 μm and a separation between ground and signal line of 1.3 μm. The distance between CPW1 and CPW2 amounts to $s_{21} = 16.5$ μm. CPW3 is integrated on top of the IP to detect its reversal via changes of its dynamic response. The nanowires connected to the injection pad are between the two CPWs [Fig. 8.1 (b)].

Phenomenology

We present AESWS spectra, see Sec. 3.2.2, showing SW resonances measured separately on the 1D MC and IP in Fig. 8.1 (c) and (d), respectively. The resonance frequencies f_{res} of the MC and IP differ overall by about 2 GHz. This difference is attributed to the different shape anisotropy. The monotonous behavior of the resonances (branches) is interrupted at switching fields H_{sw}. For the MC we define two values $\mu_0 H_{\mathrm{sw1}} = -8 \pm 1$ mT and $\mu_0 H_{\mathrm{sw2}} = -12 \pm 1$ mT reflecting the switching field distribution of the nanostripes. In the 1D MC, abrupt changes in f_{res} are either due to the reversal of an individual bistable nanostripe or a group of nanostripes.[Din11b] Between H_{sw1} and H_{sw2} the magnetic ground state $\mathbf{M}(\mathbf{r})$ thus differs from the saturated state polarized in either $+y$- or $-y$-direction depending on H. For the IP (CPW3), we find a single-valued switch-

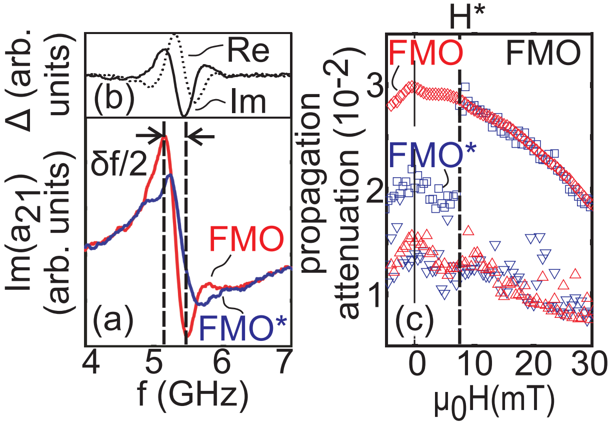

Figure 8.3: (a) Transmission signal $\Im(a_{21})$ of FMO and FMO*. A strong propagation signal (i.e. oscillations) is obtained for FMO. δf is a measure of the group velocity v_g. (b) $\Im(\Delta) = \Im(a_{21}(\text{FMO})) - \Im(a_{21}(\text{FMO}^*))$ (line) $[\Re(\Delta) = \Re(a_{21}(\text{FMO})) - \Re(a_{21}(\text{FMO}^*))$ (dotted)]. The oscillating behaviors indicate propagating SWs. (c) The propagation attenuation $\frac{a_{21}}{a_{11}}$ and $\frac{a_{12}}{a_{22}}$ for FMO (diamond and upward triangle) and FMO* (square and downward triangle). $\frac{a_{21}}{a_{11}}$ is suppressed up to $\mu_0 H = 7.5$ mT by a factor of 1.6. For $\mu_0 H > 7.5$ mT the FMO value is recovered.

ing field $\mu_0 H_{\mathrm{sw,IP}} = 1 \pm 1$ mT. For the 200 μm^2 large IP, we assume domain wall nucleation and movement as the relevant reversal mechanism. The IP is thus expected to inject domain walls into the attached nanostripes. If the injection occurred for $\mu_0 H_{\mathrm{sw1}} = -8$ mT $< \mu_0 H < 1$ mT, the attached nanostripes would have $\mathbf{M}$ anti-parallel to the otherwise saturated 1D MC.

We show $Mag(a_{11})$ measured in a minor loop (ML) on CPW1 in Fig. 8.2 (a). We saturated the sample at $\mu_0 H_{\mathrm{sat}} = +100$ mT before we applied $\mu_0 H_{\mathrm{ML}} = -4$ mT and measured for increasing H. As $\mu_0 H_{\mathrm{ML}} > \mu_0 H_{\mathrm{sw1}}$ the reversal of nanostripes without IP did not occur. In fact, in Fig. 8.2 (a) the resonance frequency increases with increasing H. This is the characteristic behavior of the mode $n = 0$ in the FMO state of a 1D MC, as presented in Sec. 6.2.1. Nanostripes are magnetized in parallel, and the 1D MC is in its saturated state. We detect the same behavior for $Mag(a_{22})$ on CPW2 [Fig. 8.2 (b)]. We do not observe any abrupt changes in f_{res}, substantiating the FMO state underneath CPW1 and CPW2. For $Mag(a_{21})$ in Fig. 8.2 (c), i.e., the signal transmitted between CPW1 and CPW2 in x-direction, we find a branch at the same field-dependent frequencies as observed in Fig. 8.2 (a) and (b). The transmission signal does not show abrupt changes either, neither in frequency f_{res} nor in signal strength. In Fig. 8.2 (d) and (e), $Mag(a_{11})$ and $Mag(a_{22})$ are shown for a slightly different ML reversal field of $\mu_0 H_{\mathrm{ML}} = -5$ mT. The branches are identical to Fig. 8.2 (a) and (b), respectively. No discrepancies are detected. The transmission signal $Mag(a_{21})$ for $\mu_0 H_{\mathrm{ML}} = -5$ mT shows however a strikingly different behavior. The data is depicted in Fig. 8.2 (f). $Mag(a_{21})$ exhibits an abrupt change of signal strength at $\mu_0 H^* = 7.5$ mT. For $\mu_0 H < 7.5$ mT ($\mu_0 H > 7.5$ mT) the detected signal is weak (strong). We attribute the abrupt change in $Mag(a_{21})$ to a field-induced variation of the magnetic ground state in that $\mathbf{M}(\mathbf{r})$ varies locally *between* CPW1 and CPW2, as the signal change is not detected in the reflection data a_{11} and a_{22}. When applying $\mu_0 H_{\mathrm{ML}} = -5$ mT, we expect domain-wall injection from IP to induce locally an anti-parallel magnetization with respect to the array's magnetization. The anti-parallel orientation of a nanostripe's magnetization $\mathbf{M}$ will be substantiated by the MFM in Sec. 8.2. We label the relevant state between $\mu_0 H_{\mathrm{ML}} = -5$ mT and $\mu_0 H^* = 7.5$ mT in Fig. 8.2 (f) as the 'ferromagnetically ordered state with a magnetic defect (FMO*)'. For minor loops with $\mu_0 H_{\mathrm{sw2}} < \mu_0 H_{\mathrm{ML}} \leq \mu_0 H_{\mathrm{sw1}}$, we observe several abrupt changes in both reflection and transmission data as expected from a stochastically disordered nanostripe array.[Din11b] In Figs. 8.2 (g)-(i) the corresponding data is shown for $\mu_0 H_{\mathrm{ML}} = -7$ mT. This is attributed to a disordered magnetic ground state of the whole MC.

In the following we study in detail the propagation properties of spin waves below and above H^* for the FMO and FMO* states. In Fig. 8.3 (a) a direct comparison of $\Im(a_{21})$ taken at $\mu_0 H = 7.0$ mT for FMO and FMO* is presented. Both states show a transmission signal near the resonance frequency $f_{\mathrm{res}} = 5.5$ GHz. The signals differ however in shape and amplitude. Note that the striking discrepancy in transmission is achieved at the same field H by varying $\mu_0 H_{\mathrm{ML}}$ by only 1 mT [c.f. Fig. 8.2 (c) to (f)]. In the FMO state, the curve is clearly oscillating which is known to indicate spin wave propagation between emitter and detector [c.f. Sec. 5.2.2]. In the FMO* state, a much weaker oscillatory contribution is detected. We now subtract the two curves to reduce the background. The detailed curve shapes in Fig. 8.2 (a) indicate that we have both a propagating spin wave signal and direct electromagnetic (em) crosstalk between CPW1 and CPW2 (step-like feature between 4 and 7 GHz). The difference signal Δ does not contain the em crosstalk. The difference signals $\Im(\Delta) = \Im(a_{21})(\mathrm{FMO}) - \Im(a_{21})(\mathrm{FMO}^*)$ (line) and $\Re(\Delta) = \Re(a_{21})(\mathrm{FMO}) - \Re(a_{21})(\mathrm{FMO}^*)$ (dotted) are shown in Fig. 8.3 (b). The phase-shifted oscillatory behaviors of $\Im(\Delta)$ and $\Re(\Delta)$ indicate a VNA-measured spin wave propagation signal in an ideal way, see Sec. 5.2.2. Following the subtraction, the transmission of SWs is larger for the FMO compared to the FMO* state. The group velocity extracted from δf amounts to $v_{\mathrm{g}} = \delta f \times s_{21} = 4.6$ km/s. In Fig. 8.3 (c), the field-dependent propagation attenuation $Mag(a_{21})/Mag(a_{11})$ as introduced in Sec. 5.3.2 is shown. For the FMO state, $Mag(a_{21})/Mag(a_{11})$ (open diamonds) decreases for increasing H starting from a value of about 0.03. Strikingly for the FMO* state, $Mag(a_{21})/Mag(a_{11})$ (open squares) starts at a low level of 0.02 and exhibits an abrupt jump to larger values at $\mu_0 H^*$. For $H > H^*$, $Mag(a_{21})/Mag(a_{11})$ of FMO* recovers the values of the FMO state perfectly. The propagation attenuation measured in the opposite direction is $Mag(a_{12})/Mag(a_{22})$. The data are depicted as open upward (FMO) and downward (FMO*) triangles. $Mag(a_{12})/Mag(a_{22})$ is found at much smaller values for both magnetic states compared to $Mag(a_{21})/Mag(a_{11})$. This is due to the non-reciprocal SW excitation in the 1D MC, see Secs. 5.3.2 and 6.3.3. The small $Mag(a_{12})/Mag(a_{22})$ does not allow one to resolve the discrepancy between FMO and FMO* states with the same signal-to-noise ratio.

8.2 Magnetic Force Microscopy

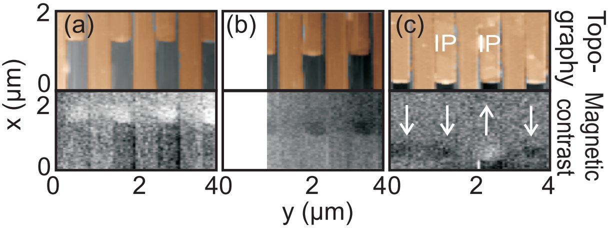

Figure 8.4: Topography (top) and stray-field contrast (bottom) of Magnetic Force Microscope images in remanence for different magnetic histories. The nanostripes are oriented vertically and neighoring nanostripes are shifted by 5 μm in x-direction. The phase contrast (bottom graph) with light or dark contrast is a measure of the magnetization of the nanostripes. (a) for $\mu_0 H_{\mathrm{sat}} = -100$ mT a light contrast is observed due to negative magnetization direction, (b) $\mu_0 H_{\mathrm{sat}} = +100$ mT a dark contrast is observed due to positive magnetization direction. (c) MFM image for the two nanostripes connected to the IP as indicated. One IP nanostripe is found in a reversed state (white end) for $\mu_0 H_{\mathrm{sw1}} < \mu_0 H_{\mathrm{ML}} < 0$.

In the following we investigate the magnetic ground state $\mathbf{M}(\mathbf{r})$ of the MC by an MFM [c.f. Sec. 6.1]. Reference MFM images with $\mu_0 H_{\mathrm{sat}} \approx -100$ mT ($\mu_0 H_{\mathrm{sat}} = +100$ mT) and $\mu_0 H_{\mathrm{ML}} = 0$ provided all white (black) contrast in the phase data in Fig. 8.4 (a) [Fig. 8.4 (b)] (bottom graph) at a given end of the nanostripes. We attributed the white (black) contrast in MFM images thus to a negative (positive) magnetization of a nanostripe. For each MFM data set we first saturated the MC at $\mu_0 H_{\mathrm{sat}}$ of about +100 mT. The field was passed through zero reaching $\mu_0 H_{\mathrm{ML}} < 0$ and then gradually increased. The MFM images were taken at remanence ($H = 0$). Applying $\mu_0 H_{\mathrm{sw1}} < \mu_0 H_{\mathrm{ML}} < 0$, we detected the reversal of one nanostripe (white) in Fig. 8.4 (c). The MFM setup was not calibrated with the same Hall sensors incorporated in the spectroscopy setup, and absolute field values H_{ML} therefore did not agree perfectly between the two setups. H_{sw1} is extracted at the MFM from the reversal of nanostripes *not connected* to the IP. Comparing with the topography image taken with the MFM (top graph), we substantiated that the reversed nanostripe was connected to the IP. We did not detect the white color for both nanostripes at the same time for $\mu_0 H_{\mathrm{sw1}} < \mu_0 H_{\mathrm{ML}} < 0$. There might have been a pinning potential along the second nanostripe connected to the IP preventing this particular nanostripe from a full reversal at such small $|H_{\mathrm{ML}}| < |H_{\mathrm{sw1}}|$. The FMO* state is thus argued to contain a single magnetic nanostripe of width $w = 255$ nm of opposite $\mathbf{M}$.

8.3 Micromagnetic Simulations

In Fig. 8.5 (a) to (c) we depict the outcome of the micromagnetic simulations, see Sec. 2.6, where we consider the propagation of SWs in FMO and FMO* states of a 1D MC. We simulated propagating spin waves after a pulsed excitation of a Gaussian-shaped excitation pulse of duration 0.1 ns. As simulation parameters we used a cell size $9.4 \times 9.4 \times 40$ nm^3 with open boundary conditions. The saturation magnetization 820 kA/m, exchange constant 1.3 10^{-6} erg/cm, damping constant 0.005. We simulate an array consisting of 256 nanostripes with a period $p = 300$ nm, air gap width $\hat{\eta} = 9.4$ nm, stripe width 291 nm, and a length of 4.8 μm each. The length is smaller than in the experiment due to restrictions existing with nowadays

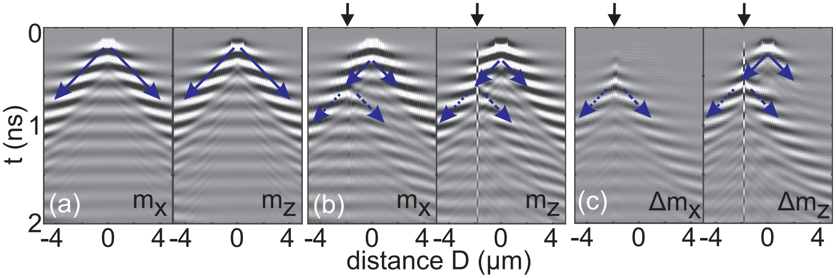

Figure 8.5: (a) In-plane m_{x} and out-of-plane m_{z} component of the dynamical magnetization obtained by micromagnetic simulations of an MC in FMO state. SWs propagate in both direction (solid arrows). Black and white contrast indicates positive and negative amplitude of $\mathbf{m}$, respectively. (b) m_{x} and m_{z} for FMO*. At -1.9 μm a nanostripe with anti-parallel $\mathbf{M}$ is introduced (vertical arrows). There, the incoming SW beam (solid arrow) is scattered. A reflected beam (dashed arrow) and a reduced transmitted beam (dotted arrow) are observed. m_{x} (m_{z}) of the MD oscillates in-phase (out-of-phase) with the MC. (c) Subtraction of (a) and (b) highlights the scattering of SWs. For Δm_{x} the initial beam cancels completely, for Δm_{z} the initial beam partly remains.

computational power. Though $\hat{\eta}$ differs between simulation and experiment, extracted velocities v_{g} are found to be nearly the same. Unintentional edge roughness in the real nanostripes might be the reason. [Kea13] Roughness is known to reduce the demagnetization effect and thereby enhances spin-precessional amplitudes right at the geometrical edges provoking a large v_{g} via enhanced dipolar coupling. The 1D MC is excited in its central region. We follow the spin wave flow to both sides. In Fig. 8.5 (a), we first show results for the FMO state at $H = 0$ which is homogeneous to both sides from the excited region. On the vertical axis from top to bottom we follow the temporal evolution of the spin-wave excitation *after* application of the pulse at $t = 0$. The x-axis shows the distance D measured to both sides from the excited nanostripes located at $D = 0$. The black and white contrast of the ringing pattern illustrates a phase shift of 180 deg, i.e., negative and positive spin-precessional amplitudes, respectively. Following the temporal evolution of the most prominent signal a spin-wave packet is observed while it moves to both sides of the 1D MC as highlighted by two arrows. The propagation is clearly resolved in the simulated x- and z-components m_{x} and m_{z}, respectively, of the dynamical magnetization $\mathbf{m}(\mathbf{x}, \mathbf{y}, \mathbf{t})$ of the nanostripes. To obtain a pronounced ringing pattern even at $D = 4\ \mu$m for both the FMO and FMO* state (where scattering is expected to take place) we consider a smaller air gap width $\hat{\eta}$ in the simulation compared to the experiment. We take $\hat{\eta} = 9$ nm providing us with a large dipolar coupling between neighboring nanostripes and, consequently, a large group velocity v_{g}. A large v_{g} is needed to obtain a large decay length $l_c = v_{\mathrm{g}} \times \tau$ and thereby a large signal-to-noise ratio at $D = 4\ \mu$m for illustrating the underlying physics clearly by Fig. 8.5 (for Py, the relaxation time τ is a few ns).

In Fig. 8.5 (b), simulation data for the FMO* state is displayed for $H = 0$ where at $D = -1.9\ \mu$m an MD is included. The MD consists of a single nanostripe with an anti-parallel magnetization $\mathbf{M}$. The spin wave beam (solid arrow) reaches the MD at $t \simeq 0.5$ ns. There, the SW is split into a reflected beam (dashed arrow) and a beam transmitted across the magnetic defect (dotted arrow) which has a smaller amplitude compared to Fig. 8.5 (a). This is in agreement with our experimental observation. The reflected beam is pronounced in m_{x} and m_{z}. To highlight the effect of the MD, the simulated traces for FMO and FMO* are subtracted. The difference signals Δm_x and Δm_z are depicted in Fig. 8.5 (c). For Δm_x only the transmitted and reflected SW beams are visible. They have almost the same spin-precessional amplitudes suggesting efficient SW reflection at the single magnetic nanoelement (about 50 %). The incoming SW beam is cancelled by the subtraction. At the same time, the MD shows a ringing pattern being *in-phase* with the spin waves. For Δm_z in Fig. 8.5 (c), the incoming beam is not fully cancelled. This might be counterintuitive at first sight, but can be explained by the dipolar interaction of the MD with the array. The dipolar interaction is far reaching and modifies the ellipticity $\frac{m_\mathrm{z}}{m_\mathrm{x}}$ (see also Eqn. 2.27) of the spin-precessional motion in several unit cells of the neighboring array. We find that the subtraction cancels the initial beam for $D > 3$ μm in Δm_z. There the intrinsic ellipticity of the MC without MD is recovered. The spatially dependent ellipticity is thus found to indicate the dipolar interaction length of a localized magnetic defect with an MC. Strikingly, in Δm_z of Fig. 8.5 (c) the ringing of the MD is *out-of-phase* with respect to the spin-precessional motion in the neighboring MC. We thus sum up that x-components of $\mathbf{m(x, y, t)}$ of the MD and MC precess in-phase, while z-components precess out-of-phase. This contrasting behavior of m_x and m_z is consistent with Ref. [Top10] where the spin-precessional motion for an antiferromagnetically ordered MC was analyzed.

8.4 Discussion

A closer look is necessary to explain the scattering of SWs at the MD formed by a single magnetic nanoelement. It is instructive to analyze the excitation of the MD by the spin-precessional motion of neighboring nanostripes. In the following, the magnetization $\mathbf{M}$ of a nanostripe is subdivided into a static component aligned with the $+y$-direction and a dynamic component precessing in the x, z-plane following $\mathbf{M} = \mathbf{M}_y + \mathbf{m}_\mathrm{x,z}$. It is reasonable to assume $m_{x,z} \ll M_y$ for the amplitude of precession. The dynamic demagnetizing field, see Sec. 2.2, is calculated from $\mathbf{m}_\mathrm{x,z}$ according to $\mathbf{h}_\mathrm{d}(\mathbf{r}) = \int_V \hat{G}(\mathbf{r}, \mathbf{r}')\mathbf{m}(\mathbf{r}')d\mathbf{r}'$, where $\hat{G}$ is the tensorial magnetostatic

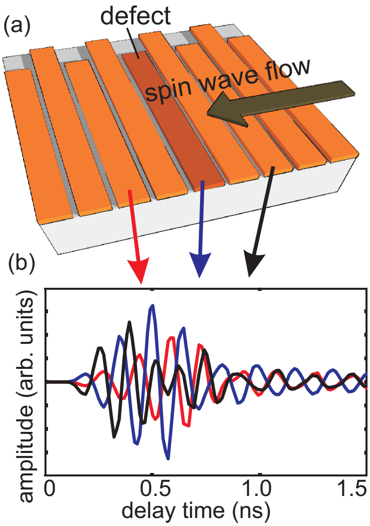

Figure 8.6: (a) Sketch of the structure, where the MD is marked. The SW is approaching from the right side towards the MD. (b) $m_z(t)$ of three nanostripes is displayed: the next-nearest nanostripe before the magnetic defect (black), the magnetic defect itself (blue), and the next-nearest nanostripe after the magnetic defect (red). The blue (red) curve exhibits a maximum at 0.5 ns (0.6 ns). The black curve exhibits two maxima at 0.4 ns and 0.7 ns, which indicates the incoming and the reflected beam. The m_z-component of the MD is out-of-phase with the precessional motion of the other nanostripes. The amplitude of the MD is larger compared to the other nanostripes.

Green's function and r, r' are position vectors inside and outside a nanostripe. The excitation field for the MD is given by the field $h_\mathrm{d} = h_{\mathrm{d},x} + i \cdot h_{\mathrm{d},z}$ generated by the surrounding nanostripes. Here, the imaginary prefactor of the z-component of $\mathbf{h}_\mathrm{d}$ provides a phase shift of $\pi/2$ compared to the x-component of $\mathbf{h}_\mathrm{d}$. The prefactor is caused by the phase difference of the corresponding components of the dynamic magnetization $\mathbf{m}$. In the following we discuss the two possible magnetic orientations of the MD separately. In the case of the FMO state, the nanostripe forming the MD later on is aligned with the MC ($+M_y$). The strong in-plane component $+h_{\mathrm{d},x}$ provokes a deflection $+m_{\mathrm{MD},x}$ of the MD. Following $d\mathbf{M}/dt \propto -\mathbf{M} \times \mathbf{h}_\mathrm{d}$, magnetization vectors of the MC and MD rotate in unison in a *right-handed* manner around the $+y$-direction towards the $-z$-direction. The m_z-components of neighboring nanostripes are nearly the same for $\lambda \gg p$. Consequently, $h_{\mathrm{d},z}$ counteracts the precessional motion of neighboring nanostripes. In contrast, in the FMO* state the antiparallel magnetization vector of the MD with $-M_y$ exhibits a *left-handed* precession with respect to the $+y$-direction defined by the magnetization direction of the MC. The strong in-plane component $+h_{\mathrm{d},x}$ of a neighboring nanostripe deflects $\mathbf{m}_\mathrm{MD}$ in $+x$-direction, similar to the FMO case. However, $\mathbf{m}_\mathrm{MD}$ rotates *left-handed* towards the $+z$-direction whereas the neighboring nanostripes precess towards the $-z$-direction at the same time. The m_z-component of the MD is thus out-of-phase with the precessional motion of the MC as shown in Fig. 8.6 (b). $h_{\mathrm{d},z}$ provides an attractive force enlarging the excitation for the MD (c.f. Fig. 8.6 (b)). As a result, in FMO* both components of $\mathbf{h}_\mathrm{d}$ of the surrounding MC act together in-phase on $\mathbf{m}_\mathrm{MD}$, which appears as a changed 'wave impedance' for the SW compared to the FMO state. This impedance mismatch provokes partial reflection and reduced transmission at the subwavelength-wide element ($w/\lambda \approx 0.02 - 0.03$). In further simulations we have considered different numbers q of selectively reversed nanostripes in an otherwise saturated 1D MC (we tested $q = 1, 2, 3, 4$). Thereby we find that the scattering of spin waves is robust against the exact number of the subwavelength magnetic defects. The reflected beam intensity does not depend crucially on q suggesting an 'interfacial' rather than a 'bulk-like' scattering effect. The control of SW transmission by an individual nanostripe as a switchable and semitransparent mirror in an MC is far-reaching. It has already been shown that **M** of a stripe can be reversed by a biasing current which moves back and forth an existing domain wall. [Yam04] By integration of leads, a three-terminal device can be created consisting of a 1D MC equipped with emitter and detector antennas where a central nanostripe is current-biased. Controlling the nanostripe's magnetization **M** by the current, the MC is 'gated', and the transmitted SW signal is switched on and off by current pulses [Tog11] in a transistor-like configuration. Using two of the mirrors in series, SW cavities in an MC [Fil12] become switchable. The 'on/off' ratio provided by the nanomagnets still needs to be optimized in future experiments.

We studied spin wave propagation in 1D MCs with a reprogrammable magnetic defect. The spin wave is scattered at the nanostripe with anti-parallel magnetization due to out-of-phase spin precession. The subwavelength magnetic nanoelement acts as a semitransparent SW mirror which is switched on and off by the magnetic history or a current. The findings are promising for spin wave control on the nanoscale.

9 Atomic Layer Deposition of Ferromagnetic Metals

Atomic layer deposition (ALD), originally called atomic layer epitaxy, was developed by T. Suntola in the 1970's. [Sun77] Atomic layer deposition stands out from other deposition techniques by the isotropic and homogeneous growth. [Sun92, Les02, Geo10] This allows the deposition on porous substrates without shadowing effects. Aspect ratios of more than 10^3 have been achieved. [Ela03, Kar10, Geo10] This high aspect ratio growth makes ALD suitable for the deposition of material in nanostructured templates. [Xio05, Dau07, Les11] It has been shown, that the deposition of material by ALD in nanoporous templates can be even spatially controlled. [Ela07] Also patterend ALD on planar substrates has been accomplished. [Yan01, Geo10] At the same time, the ALD of ferromagnetic metals has made rapid progress. [Dau07, Bac07, Lee09, Cho10, Cho11] Several processes for Fe, Ni, and Co, and their compounds have been developed. For Fe, Ni, and Co investigations on the magnetization configuration in ALD overgrown nanostructures have been performed. [Dau07, Bac07, Bac09] However, in a recent textbook about ALD it is stated: [Les11]

"Metal ALD is not yet mature. There is still a need for better processes for first row transition metals such as iron, cobalt, [and] nickel... There is a need to make progress in the development of ALD for these metals because of the possible 3D applications that may appear in the future."

In fact, there are a number of challenges on the way to ALD of high quality ferromagnetic material. The FMR is a key property, that depends on several material parameters, e.g. the saturation magnetization (see Sec. 2.4.2), and the magnetic damping, for optimizing the deposited material. Yet, the investigation of the FMR so far has not been addressed. ALD coating of prepatterned templates with low damping ferromagnetic material allows for creation of *second* *generation of nanomaterials* [Bae11], i.e. the homogeneous deposition of material onto nanospheres, nanowires, or nanomembranes. Intriguing physical phenomena are expected from such novel prototypes of ferromagnetic nanomaterials, e.g. large magnonic bandgaps. [Kra08, RV12] However, on the one side, physical restrictions have to be considered, e.g. the relatively high damping α of polycrystalline Ni and Fe. On the other side, the obstacles due to the complex deposition technology have to be overcome, e.g. entrapment of impurities in deposited films. Target of this thesis is ALD of a thin film with a small roughness exhibiting a low magnetic damping, and the application of the developed processes to nanotemplates, such as nanowires or nanostructured samples.

9.1 Technology

ALD is a chemical vapor deposition (CVD) technology. In contrast to conventional CVD, ALD supplies the reactants separately and sequentially. This leads to surface chemistry dominated processes. Each of the gaseous precursors reacts with the surface of a sample in a self-terminating way. Going into detail, the first precursor is injected into a reaction chamber and is adsorbed (via chemi- or physisorption) on the surface of a substrate till the surface is saturated. Then the reaction chamber is purged. After injection of the second precursor, it reacts chemically till all adsorbed molecules from the first precursor are consumed. This leads also to saturation, sometimes called self-terminated or self-limiting process. Thereafter the reaction chamber is purged, and the whole process can be repeated. Comprehensive reviews on ALD in general can be found elsewhere. [LB03, Puu05, KM07, Geo10, Les11]

We define the durations for the four relevant pulses as t_1,t_2,t_3, and t_4. The process is then defined by [Mar11]

$$C \times [(t_1|t_2) + (t_3|t_4)], \tag{9.1}$$

where t_1 and t_3 are the precursor exposure times, and t_2 and t_4 are the corresponding purge times (C is the number of cycles). These durations are characteristic for an optimized ALD cycle and will be

listed for all presented processes. That way the desired material is deposited monolayer by monolayer. This leads to conformal growth. The thin film thickness is controlled by the number of cycles.
The dominant processes contributing to the reaction:

- Diffusion of the precursor to surface
- Adsorption of the precursor
- Desorption of the reaction products
- Diffusion of the reaction products from the surface

Typically, the diffusion processes are not crucial, as these are controlled by the process parameter. In Sec. 9.2 the critical problem of chemisorption of the precursors is discussed. There exists a processing window for an ideal growth of monolayers, i.e., a characteristic temperature range. This processing window is called ALD window, where the growth rate does not depend on the temperature due to the self-limiting deposition process. [Les02, Geo10] This window is advantegeous, as temperature drift or inhomogenities do not influence the deposition. In Fig. 9.1 (a) the temperature dependence of an ALD process is sketched where the ALD window is situated between the regions of non-conformal growth. For a lower temperature, either the growth rate decreases due to inhibited nucleation, or a strong physisorption increases the growth rate due to precursor condensation. For a higher temperature, either decomposition of the precursor yields a higher growth rate, or a higher desorption rate decreases the growth rate. [Geo10] The ALD process is also influenced by the duration of the precursor pulses t_1 and t_3. A full adsorption has to be achieved. However, too long exposure times t_1 and t_3 lead to desorption or decomposition effects. The purge times t_2 and t_4 are also important. They have to last long enough to inhibit gas phase interactions. The reactor design and the chemical and physical properties of the precursors are dominating the growth behavior. The precursor materials are key for the self-limiting deposition. They need to fulfil certain requirements:

- Enough vapor pressure
- Good adsorption properties and high reactivity
- Adequate thermal stability
- A limiting character of the surface reaction.

From a chemistry point of view, precursors can be classified in anorganic and organic molecules. The anorganic percursors provide the deposition of a lot of elements. Metallic as well as non-metallic elements form heat-resistive chlorides. They react with water, but have some drawbacks, such as etching of the reaction product. For ALD of Si e.g. the precursors SiH_2Cl_2 and hydrogen radicals are used, whereby corrosive HCl is formed. In recent years the development of organic precursors made large progress. There are a lot of alkyles, amides, and cyclopentanoids, that were used successfully. [LB03, Les11] In particular the alkyles are adequate for ALD processes, such as Trimethylaluminum (TMA), that is used for Al_2O_3 deposition. [Gro04, Geo10] Another important group are the cyclopentanoids. They provide metals (i.e. Pt, Ru), that were not available with the alkyles. [Aal03, Kno09] Furthermore, cyclopentanoids have been recently used succesfully to fabricate transition metals, e.g. Fe, Ni, and Co. [Dau07, Bac07, KM07]

We use TMA for Al_2O_3 deposition, and ferrocene [$Fe(C_5H_5)_2$ or $FeCp_2$] and nickelocene [$Ni(C_5H_5)_2$ or $NiCp_2$] for Fe and Ni deposition. $FeCp_2$ and $NiCp_2$ belong to the group of metallocenes and are therefore chemically similar. An atomic model of such metallocenes is depicted in Fig. 9.1 (b). Two pentan rings are sandwiching a metal ion. The higher reactivity of $NiCp_2$ in comparison to $FeCp_2$ is caused by the number of valence electrons. Fe^{2+} has 6 electrons in the d-shell, where all electrons are involved in the bond to the cyclopentan rings. In contrast, Ni^{2+} contains 8 electrons in the d-shell. Two electrons thereof are antibonding. Therefore, $NiCp_2$ is very reactive and sensitive to oxygen. [Pug99]

Nickelocene is used for CVD to produce Ni thin films and the mechanisms have been thoroughly investigated. [Bri99c, Bri99a, Bri99b, Bri00] Similar analysis on reaction paths of ferrocene was done by Russel *et al.* [Rus96]. ALD processes using metallocenes are already documented in literature [Dau07, Bac07, Lu08, Bac09, Bac11, Mar11].

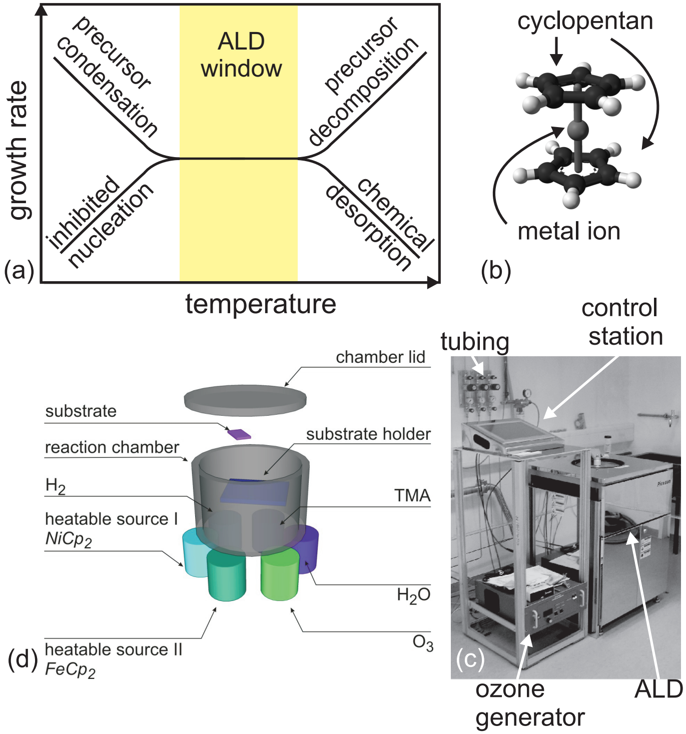

Figure 9.1: (a) Temperature dependence of an ALD process exhibits a so called ALD window, where the growth rate is constant. For a temperature outside the ALD window the growth rate is varying with the temperature. (b) Model of a metallocene molecule: [Mil09] A metal ion is sandwiched between cyclopentadienyl rings. (c) PicoSun Sunale ALD reactor with control station, tubing of N_2, O_2, and H_2, and the ozone generator. (d) Sketch of the ALD machine. The precursor lines under the reactor are connected by (heated) tubes with the reactor. There are six precursors: TMA (Trimethylaluminum), H_2O, $NiCp_2$ (Nickelocene), $FeCp_2$ (Ferrocene), ozone O_3, and molecular hydrogen H_2. The sample is put on a substrate holder into the reactor, which is heatable up to 500 °C.

9.2 State of Research

In this work the ALD of ferromagnetic material was achieved by oxidation of metallocenes, i.e., $NiCp_2$ and $FeCp_2$. The used process is based on chemisorption of the metallocenes, and a subsequent oxidation by O_3. To obtain metallic ferromagnetic material a reduction step is necessary, which is performed either after the deposition process, or layer-by-layer. Therefore, we separate the discussion into a deposition process, without intermediate reduction step, that in the following is called *oxidic process*, and a second deposition process, where hydrogen is present during the deposition process, that we call *reductive process*. In the following we present the relevant state of research for both processes, in particular its subprocesses. Additionally, the state of research of alloy formation by ALD is summarized.

9.2.1 Adsorption of $NiCp_2$ and $FeCp_2$ Without the Presence of H_2

The surface reaction mechanism of $FeCp_2$ and O_3 has been investigated by Martinson *et al.* [Mar11]. The chemical mechanisms for deposition of Fe_2O_3 using $FeCp_2$ and O_3 were elucidated by analyzing the chemical products. After the $FeCp_2$ pulse the molecules cyclopentadiene (C_5H_6) and cyclopentadienone (C_5H_4O) were formed. This indicated surface reactions that fragmentized the adsorbed $FeCp_2$. [Mar11]

The adsorption of $NiCp_2$ on Ni and NiO has been studied in detail by Pugmire *et al.* [Pug99]. On both, the reactive NiO and the highly reactive Ni surface, $NiCp_2$ molecules adsorbed and decomposed to C_xH_y fragments. This chemical process was considered also with CVD. There, the molecule C_5H_6 was formed by a surface reaction involving two adsorbed $NiCp_2$ molecules [Bri99b]

$$\begin{aligned} &2\mathrm{Ni(C_5H_5)_2(ads)} \rightarrow \\ &\rightarrow Ni(C_5H_5)(ads) + \quad (C_5H_5)Ni(C_5H_4)(ads) + C_5H_6(g) \end{aligned} \tag{9.2}$$

where (ads) indicates an adsorbed species, and (g) indicates the gaseous state. Offering ozone led to combustion, i.e. burning of remaining surface-bound hydrocarbon-based ligands. Due to the high reactivity of ozone, all hydrocarbon was expected to be oxidized.

[Mar11]
Following the mentioned investigations, we adapt these considerations on the ALD of NiO (FeO) by $NiCp_2$ ($FeCp_2$) and O_3. A scheme for the process is presented in Fig. 9.2. We suggest the surface being oxidic when $NiCp_2$ ($FeCp_2$) adsorbs. Thus, we can assume a partial decomposition of $NiCp_2$ ($FeCp_2$). After the injection of O_3 combustion is expected. Furthermore, adsorbed Fe and Ni is oxidized. A similar reaction scheme was presented for ALD of Ruthenium by $RuCp_2$ and O_2. [Aal03]
Residues of the decomposed and adsorbed C_xH_y fragments might react with Fe and Ni and form stable carbides. This leads to impurities in the ferromagnetic thin films. [Bri99a] The oxidic ALD processes (for NiO and Fe_2O_3) and the related ex situ reduced metallic thin films have been reported. [Dau07, Bac07] The deposited material is ferromagnetic and conducting. Also binary and ternary oxides, e.g. FeNiO, have been produced [Cho10, Cho11]. Magnetodynamic investigations have not been conducted till now.

9.2.2 Adsorption of $NiCp_2$ and $FeCp_2$ In Presence of H_2

An improvement of the thin film quality in terms of homogeneous growth has been reported by Knoops *et al.* and Hämäläinen *et al.*. They investigated an ALD process of Pt and Ir with metallorganic percursors and ozone, that is similar to ALD using $NiCp_2$ or $FeCp_2$, and ozone as precursors. They introduced an additional hydrogen step after each ozone pulse. [Kno09, Ham09, Ham11] Thus, they could decrease the process temperature, and deposited thin films with smaller roughness. In a similar way, we used the discussed process in Sec. 9.2.1 and introduced an additional hydrogen step after each ozone pulse. In the following we discuss the chemistry of $NiCp_2$ and $FeCp_2$ in presence of H_2. As the chemistry of CVD and ALD is similar in some aspects, it is instructive to discuss the surface chemistry of the CVD process in order to get a deeper insight. [Les11] A detailed analysis on $NiCp_2$ reaction paths in presence of H_2 has been provided for CVD. [Bri99c, Bri99a, Bri99b, Bri00, JHP01]. In the presence of H_2 from an earlier pulse the reaction of $NiCp_2$ is

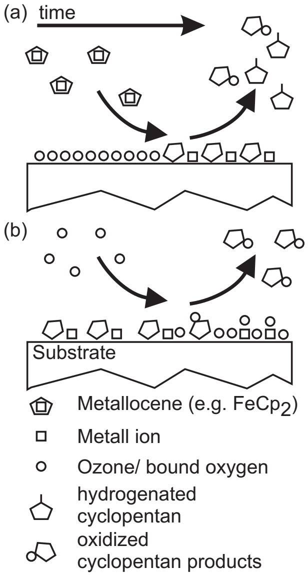

Figure 9.2: (a) Injected metallocene molecules react with an oxidized surface by fragmentization. The fragments are the metall ions, cyclopentan molecules and fragments thereof that are adsorbed at the surface. Oxidized and hydrogenated cyclopentan is produced. (b) Injected ozone reacts with the adsorbed species. Oxidized cyclopentan and oxidized fragments (e.g. CO_2) are produced. The surface becomes oxidic again.

different from Sec. 9.2.1: [Bri99b]

$$\mathrm{Ni(C_5H_5)_2 + 1/2H_2 \rightarrow Ni(C_5H_5) + C_5H_6}. \qquad (9.3)$$

Here, $NiCp_2$ is dissociated and the carbide source C_5H_4 is not formed. Though, the presented reaction is valid for CVD conditions, adsorbed hydrogen molecules dissociate on the surface of Ni. [Chr74] Adsorbed H atoms are highly reactive, [Vre92] and therefore the formation of C_5H_6 as presented in Eqn. 9.3 is reasonable. In summary, we expect an adsorption of Ni and remaining hydrocarbons, while C_5H_6 is released. The ozone pulse is needed as a cleaning process that combusts and releases the hydrocarbons and forms metaloxides. Concluding the investigations, we suggest a reaction process for the presented ALD process in Fig. 9.3.

It is interesting to compare the Ni deposition in presence of H_2 with the equivalent Fe deposition. $FeCp_2$ and $NiCp_2$ react very similar with ozone, as ozone is a strong oxidizing agent and combusts the molecule. [Cho10] In contrast, the hydrogenation of the two metallorganic molecules, which is relevant when the introduced metallorganic molecules react with adsorbed hydrogen, yields molecules with different properties. After hydrogenation of $NiCp_2$, the resulting $NiCp_2H$ is not stable and leads to $[Cp_3Ni2]^+$ [Den99] or NiCp [Par08]. The hydrogenation of $FeCp_2$ results in the stable molecule $[FeCp_2H]^+$. [ML00] Thus, the H terminated surface reduces the adsorption of $FeCp_2$ in subsequent pulses.

9.2.3 Alloy Processes

The deposition of doped or mixed oxidic materials by ALD has been reported in literature. One of the first examples is an antimony-doped tin dioxide thin film [Vii94]. Oxides of magnetic material, such as FeNiO have been realized [Cho10, Cho11]. A recent challenge in research is the deposition of metallic alloys. The initial study was done by Christensen *et al.* [Chr10], who presented the deposition of Ir and Pt forming a metallic alloy. Also the deposition of the ferromagnetic alloy CoW was demonstrated. [Shi11] For alloy formation it is necessary that the surface chemistry of the different precursors is mutually compatible and the deposition conditions are

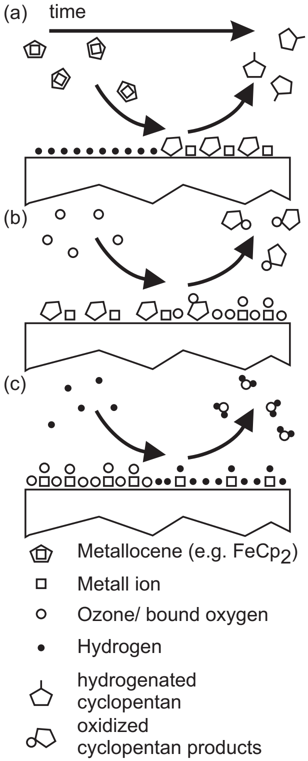

Figure 9.3: (a) Injected metallocene molecules react with an hydrogenated surface by splitting off a hydrogenated cyclopentan molecule. The remaining molecule or parts thereof adsorb at the surface. (b) Injected ozone reacts with the adsorbed species. Oxidized cyclopentan and oxidized fragments (e.g. CO_2) are produced. The surface oxidizes. (c) Hydrogen reduces the oxidized metall ions by production of water. The surface becomes hydrogenated again.

similar. Additionally, inhibited nucleation or etching processes of components are possible. For an appropriate set of precursors the growth and properties of mixed thin films can be predicted using simple rule-of-mixture formulas. This rule is based on the precursor ratio that is employed during the deposition. This assumes that the growth of each component is unaffected by the presence of the other components in the film. [Chr10]

The reduction process of oxidized FeNi alloys has been investigated by Vreeburg *et al.* [Vre92]. The reduction of ultrathin, oxidized FeNi thin films by hydrogen was performed at 350°C. The reduction of a NiO thin film at such conditions is a fast process and a Ni thin film remains where oxygen is removed. In contrast, after the reduction of FeO at such conditions oxygen in the thin film remains. For an ideal FeNi alloy the composition is defined as $\mathrm{X} = \mathrm{c}_{\mathrm{Fe}}/(\mathrm{c}_{\mathrm{Fe}} + \mathrm{c}_{\mathrm{Ni}})$, where c_{E} is the measured concentration of the element $\mathrm{E} = \mathrm{Fe}, \mathrm{Ni}$. A reduction of a FeNi alloy is found to be possible for $\mathrm{X} \leq 0.5$ considering similar parameters like in this thesis. [Vre92] It is assumed that the Ni acts as a catalyst for the overall reduction process, in that Ni bounds oxygen from Fe, and then Ni is reduced by hdyrogen.

9.3 Reaction Chambers

9.3.1 PicoSun ALD Reactor

We use a multisource ALD SunAle reactor[1]. The machine is a hot wall ALD reactor with a modified shower head geometry. The maximum temperature of the reactor and substrate holder is 500 °C. Ultrahigh purity nitrogen (99.999%) continuously passes through the reactor, where a pressure of 1 to 10 hPa is stabilized. In all supply lines the flow rates are regulated seperately. The precursor gases detailed below are introduced into the flow of nitrogen. The reaction chamber is designed for 4-inch wafers. We have special inlets to use flow-through materials, where the gas flow is led through a porous sample. In the framework of this thesis, we use six precursor materials: TMA (Trimethylaluminum), H_2O, $NiCp_2$ (Nickelocene), $FeCp_2$ (Ferroocene), ozone O_3, and molecular hydrogen H_2. Ozone is cre-

---

[1] PicoSun, Espoo, Finland

ated by an ozone generator AC 2025[2], which needs ultrahigh purity $O_2/0.5\%N_2$[3] flowing through the generator. The ozone concentration is as high as 5 to 10 %. Hydrogen is supplied also as ultrahigh purity gas. $FeCp_2$ and $NiCp_2$ are in steel bubblers which are heated between 110 and 160 °C. The feedthrough is indirectly heated by the hot chamber, which always has to be hotter than the bubbler to prevent condensation. The TMA and H_20 are provided from cooled stainless steel bottles to decrease the vapour pressure. Strongly reducing and oxidizing agents are available through the gases H_2 and O_3, respectively.

9.3.2 Reduction Chamber

An high-vacuum chamber with a DownStream [4] microwave source at 2.45 GHz and a power of 50 Watt was used for reduction processes operated by Dr. Paul Berberich. The forming gas was Ar/H_2 90/10 or an Ar/H^+ plasma at a flux of 10 sccm and a chamber pressure of 10^{-3} hPa. At this pressure a stable plasma was obtained. At the same time the scattering length of H^+ is long enough to reach the sample. By an electrical heater we heat the sample holder up to 450°C. The temperature was measured at the substrate holder by a Chrome/Alumel thermocouple. Metallic wires contacting the sample surface allowed us to monitor the electrical resistance during the reduction process. Thereby, the process parameters could be optimized. A typical reduction process takes 2 h at a temperature of about 400°C in an Ar/H^+ 90/10 atmosphere.

9.4 Methodology and Analysis

In the course of this thesis over 100 atomic layer deposition processes were conducted. We used 8×8 mm^2 large Si, MgO and glass substrates. We cleaned all samples using acetone and isopropyl alcohol before putting several samples (typically about 5) into the hot ALD reactor. Also the used precursor bottles are heated. A cleaning pulse

---

[2] IN USA Inc., Norwood, USA

[3] all gases: Linde AG, Pullach, Germany

[4] ASTeX DPC Downstream Plasma Applicator

of O_3 is applied. On each sample a seed layer of 5 nm thick Al_2O_3 is deposited. Then the desired ALD process is started, where typically 800 cycles are performed. After the process in case of metallic thin films it is necessary to cool down the reactor in order to inhibit oxidation in air before getting the samples out. For oxidic thin films we get the samples out at high temperature. For a further reduction the samples are put into the reduction chamber, see Sec. 9.3.2.

Different methods of chemical and physical analysis were applied to the deposited thin films. Samples were analyzed in terms of topography and homogeneity, electrical conductivity, and static and dynamic magnetic behavior. We used high resolution scanning electron microscopes (SEM) and transmission electron microscopes (TEM) to investigate the surface of the thin films. We investigated the resistivity of reduced FeO and NiO systematically. The resistivity is measured by a four point probe to avoid contact resistance. The composition of the alloy samples is analyzed by electron dispersive X-ray spectroscopy (EDX), electron energy loss spectroscopy (EELS) and inductively coupled plasma atom-emissions-spectroscopy (ICP-AES). The static magnetic behavior is investigated by a magneto-optical Kerr effect (MOKE) setup. The FMR is studied by a VNA-FMR measurement setup (see. Sec. 3). Key parameter for improvement of the thin films is the ferromagnetic damping parameter α, see Eqn. 5.13. We get access to the ferromagnetic damping by studying the linewidth of the FMR and the effective magnetization (see Sec. 2.4). The presented values of the linewidth are obtained from the accessible magnitude data. The linewidth value of the imaginary part of the susceptibility is smaller by $\sqrt{3}$ compared to the magnitude data. It has been reported that defects contribute significantly to the damping, e.g. the topography as well as impurities. [Sta09, Ari99, Fae11]

In the following sections, we compare obtained values on ALD samples with values from reference samples that are fabricated by physical vapor deposition.

9.5 ALD of Metallic Ferromagnets by Ex Situ Reduction

In the following ALD of FeO and NiO with an ex situ reduction process is presented. We present the process parameters and analyze ferromagnetic properties by measuring MOKE and FMR. The process is similar to processes presented in literature. [Dau07, Bac07, Bac09, Bac11]

9.5.1 Process Parameters

As metal-ion containing precursor materials we use $FeCp_2$ and $NiCp_2$, which are oxidized by O_3 and finally reduced in a separate vacuum chamber by hydrogen (or hydrogen plasma). The reaction scheme is presented in Sec. 9.2.1. The ALD reaction chamber is stabilized at a temperature between 200 °C to 350 °C. The solid precursor $FeCp_2$ ($NiCp_2$) is heated to a temperature of $130 - 160\,^\circ\mathrm{C}$ ($100 - 150\,^\circ\mathrm{C}$). The process flow [c.f. Eqn. 9.1] of the process is equal for both precursors $FeCp_2$ and $NiCp_2$

$$C \times (0.8\ \mathrm{s}|4\ \mathrm{s} + 10.0\ \mathrm{s}|10.0\ \mathrm{s}), \tag{9.4}$$

to obtain a thin film. The thickness of the obtained reddish colored FeO (grayish colored NiO) thin film is measured by ellipsometry. The growth rate amounts to 0.6 Å/cycle (0.6 Å/cycle).
Performing processes at different substrate temperatures ranging from 200 °C up to 350 °C we found an ALD window at 300 °C.
We reduced the non-ferromagnetic oxides FeO and NiO to metallic, ferromagnetic Fe and Ni by an ex situ reduction. The reduction processes were performed in a reduction chamber as described in Sec. 9.3.2. The relevant temperatures for FeO (NiO) were $400 - 600\,^\circ\mathrm{C}$ ($230 - 480\,^\circ\mathrm{C}$) in an Ar/H_2 or Ar/H^+ atmosphere as a reducing agent.
A set of NiO samples are reduced at different temperatures, different periods, and pressures of H_2 or H^+ in order to optimize the magnetization dynamics, i.e., reduce the magnetic damping.

9.5.2 Thin Film Properties

Electrical Properties

After reduction the thin films are metallic and conducting. The temperature profile and square resistance of a typical reduction process are shown in Fig. 9.4 (a). A rapid decrease of the resistance is observed when introducing the reduction agent. The lowest measured resistivity for Ni (Fe) grown by an optimized ALD process amounts to 10 $\mu\Omega$cm (150 $\mu\Omega$cm) at room temperature. The measured values are compared to the literature values for Ni (Fe) of 7 $\mu\Omega$cm (9.8 $\mu\Omega$cm). [Bri99a, Rub88] The resistivity of Ni is about 28% higher compared to the literature value for CVD grown Ni. There are three main contributions for an enhanced resistance in chemically deposited thin films: [Bri99a]

- topography, e.g. porous thin film structure
- oxygen content in the thin film
- carbon content, i.e., carbon contents of 5 – 15 % typically increase the resistivity by an order of magnitude.

The lowest resistivity of Fe is still higher by one order of magnitude compared to the literature value. We attribute this to the higher stability of FeO compared to NiO against hydrogen, and therefore remaining oxygen in the Fe thin film.

MOKE

All metallic thin films grown by ALD showed a hysteretic behavior. Exemplarily for all following sections, a typical MOKE measurement of a Ni thin film with ex situ reduction is shown in Fig. 9.4 (b). The Ni thin film on a silicon substrate exhibits the typical ferromagnetic behavior with a hysteretic reversal behavior as has been reported in literature. [Dau07, Bac07, Bac09] The field was applied in the plane of the thin film. The coercive field in this case amounts to 10.5 mT.

SEM and EDX

By EDX the composition of NiO is measured to be Ni:O = 60:40, which is near the expected stochiometry $Ni_{50}O_{50}$. Conformal growth

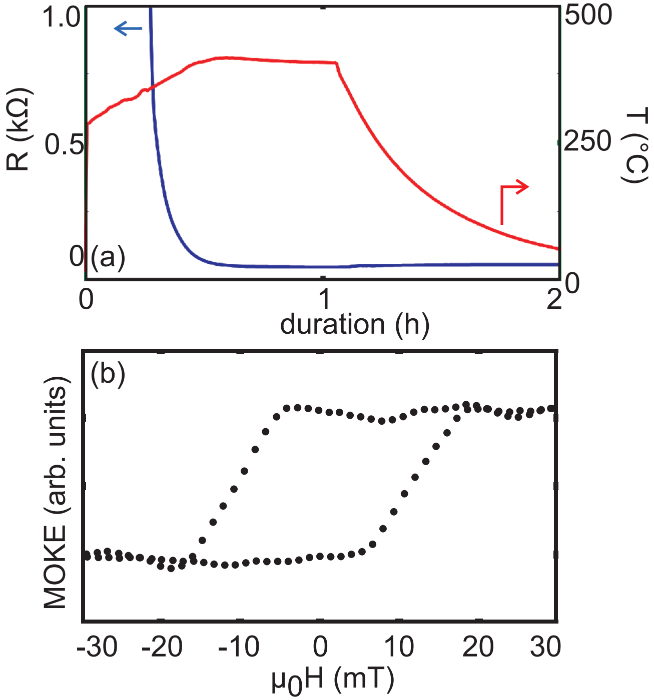

Figure 9.4: (a) Resistance measurements during a typical reduction process of FeO (sample FH_FeO_20120921) at a temperature of 400°C in an Ar/H^+ 90/10 atmosphere. The dark line indicates the measured resistance. The red line shows the temperature during the reduction process. The sheet resistance stabilizes at a value of 57 Ω. (b) Typical MOKE measurement of a metallic ALD grown Ni thin film on a silicon substrate showing a ferromagnetic hysteresis. The field was applied in the plane of the thin film. The coercive field amounts to 10.5 mT.

over the edges of a micro-pillar, see Fig. 9.5 (a). However, the coating is not homogeneous, holes are observed. Reduction processes at elevated temperatures, often yield a non-homogeneous thin film, as shown in Fig. 9.5 (b). We attribute this to the so called Ostwalt ripening. [Wag61, Hil65] At a high temperature small grains shrink, while big grains grow. Therefore, elevated temperatures that are higher than the deposition temperature are not desired for reduction, as they increase the roughness. A typical example is observed in Fig. 9.5 (c) - (e) (sample RH_SOI_021_20110304). There, NiO is conformally deposited in holes with a diameter of 150 nm going through a Si membrane[5] [see Fig. 9.5 (c)]. Due to conformal growth NiO is deposited into the hole which decreases the diameter of the hole by 110 nm as shown in Fig. 9.5 (d). The grain size of NiO is smaller than 40 nm. After the reduction process the surface looks smooth, however the thin film is no longer homogeneous, as shown in Fig. 9.5 (e). Material has moved and formed areas without material on the substrate and coated areas, which results from the Ostwalt ripening.

Ferromagnetic Resonance Measurements

VNA-FMR measurements, see Sec. 5.1, were performed on all ex situ reduced Ni thin films. We present obtained data from a typical sample, i.e. sample RH_113_Ni_20111215. The reduction process temperature of this sample has been optimized, i.e., for this sample a reduction process at a temperature of 440 °C in H_2 atmosphere was conducted. The process was optimized in that the damping parameter α was reduced. The signal-to-noise ratio of the spectra is large enough to analyze the linewidth and the field dependence of the FMR. Firstly, we focus on the linewidth: An FMR spectrum of the sample RH_113_Ni_20111215 is shown in Fig. 9.6 (a). The presented spectrum is performed at $\mu_0 H = 80$ mT. We observe a linewidth of $\Delta f = 1.5$ GHz at a resonance frequency of $f_0 = 5.4$ GHz. Secondly, the field dependent FMR measurement is investigated (see Fig. 9.6

---

[5] Fabrication of membranes in [Bra10]

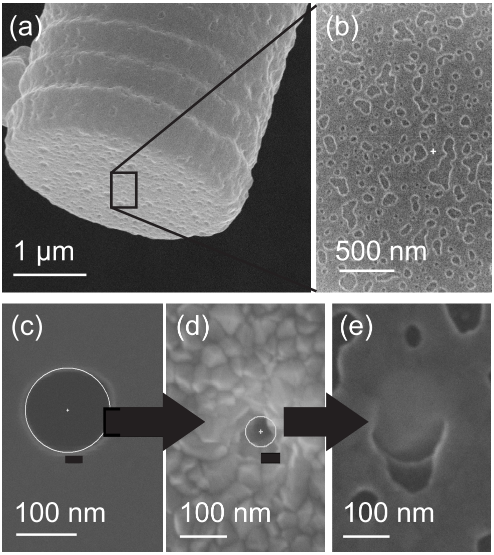

Figure 9.5: (a) Growth test verifying a conformal growth of reduced NiO over the edges of a micro-pillar produced by Anna Dalmau and Prof. Dr. Anna Fontcuberta i Morral (École Polytechnique Fédérale de Lausanne, Lausanne, Switzerland). (b) Top-surface of the micro-pillar shows a grainy surface with areas without material on the substrate and coated areas. (c) Hole with a diameter of 150 nm going through a Si membrane (sample RH_SOI_021_20110304), (d) after NiO deposition, and (e) after reduction. The grainy structure in (b) and (e) is attributed to the Ostwalt ripening.

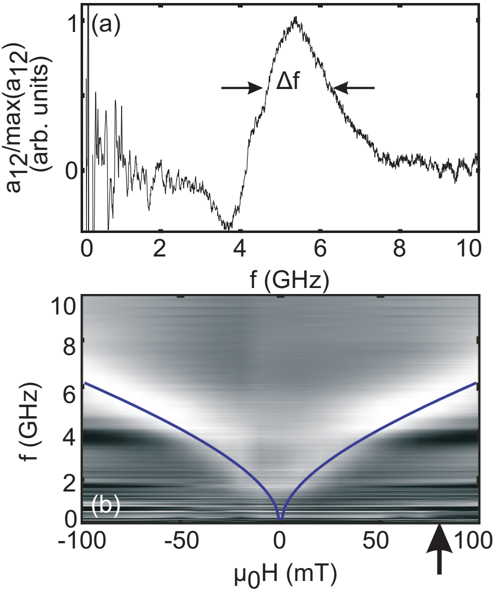

Figure 9.6: (a) VNA-FMR spectra at $\mu_0 H = 80$ mT of an ALD grown NiO sample that is reduced at 440 °C in H_2 atmosphere (sample RH_113_Ni_20111215). The linewidth amounts to $\Delta f = 1.5$ GHz at a resonance frequency of $f_0 = 5.4$ GHz. (b) Field dependent FMR. The blue line is a fit by the Kittel equation that yields an effective magnetization of $M_{\mathrm{eff}} = 380 \pm 50$ kA/m. The perpendicular arrow at $\mu_0 H = 80$ mT indicates the position of the spectra in (a).

(b)). We use Eqn. 5.2

$$f_{\mathrm{res}} = \frac{\gamma}{2\pi}\mu_0 \sqrt{H \cdot (H + M_{\mathrm{eff}})}$$

to explain the field dependence. An effective magnetization of $M_{\mathrm{eff}} = 380 \pm 50$ kA/m (assuming a thin film without an in-plane anisotropy) is obtained.

Now, we compare both values, the linewidth and the effective magnetization, with an evaporated reference sample (by physical vapour deposition). The linewidth of a reference sample with evaporated Ni is $\Delta f = 1.1$ GHz at $f_0 = 6.1$ GHz. The effective magnetization of the evaporated reference sample amounts to $M_{\mathrm{eff}} = 480 \pm 50$ kA/m. Thus, we find a smaller linewidth and a smaller effective magnetization of the ALD-grown sample compared to the reference sample. Using Eqns. 2.33 and 5.13 these values correspond to a damping parameter $\alpha = \frac{\Delta\omega}{2\mu_0\gamma(H+M/2)}$. Thus, we obtain $\alpha_{\mathrm{Ni,op}} = 0.10 \pm 0.01$ for the *oxidic process* compared to a damping parameter for the evaporated Ni of $\alpha_{\mathrm{Ni,evap}} = 0.06 \pm 0.01$. The effective magnetization of different ALD-grown films varies from $M_{\mathrm{eff}} = 300$ kA/m to $M_{\mathrm{eff}} = 400$ kA/m.

In Fig. 9.7 a FMR spectrum in out-of-plane geometry ($H\perp$ film) is presented (sample RH_Ni_20121113). The measurements were performed by Ioannis Stasinopoulos. The spectrum exhibits a pronounced FMR. The resonance frequency increases with increasing field starting at $\mu_0 H = 0.3$ T. The linewidth at $f_{\mathrm{res}} = 11$ GHz amounts to $\Delta f = 1.2$ GHz. In Fig. 9.7 (b) the resonances (light) are depicted in a gray scale plot for a wide field range. The field dependence is analyzed using Eqn. 2.40. Thus, the slope of the resonance frequencies amounts to $\gamma/2\pi = 28.5$ GHz/T, which is the gyromagnetic ratio.

FMR measurements with the field in-plane on an ex situ reduced FeO thin film show a weak signal at 12 GHz for $\mu_0 H = 100$ mT (not shown). This corresponds to a large effective magnetization of $M_{\mathrm{eff}} = 1400 \pm 100$ kA/m.

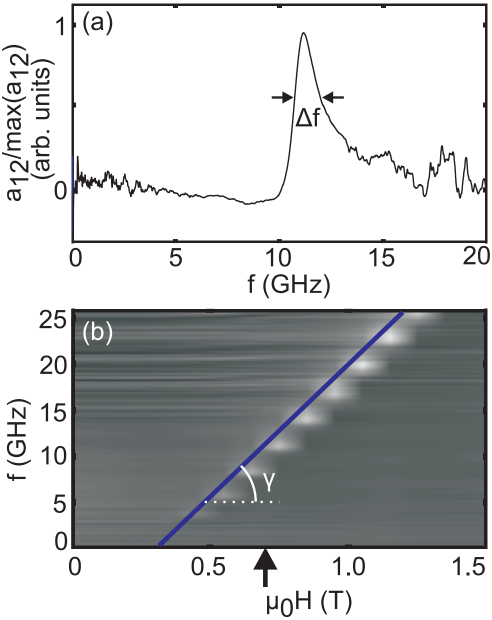

Figure 9.7: (a) An FMR spectrum in out-of-plane geometry ($H\perp$ film) of sample RH_Ni_20121113. The spectrum shows a pronounced FMR with a linewidth of $\Delta f = 1.2$ GHz at $f_{\mathrm{res}} = 11$ GHz. (b) Gray scale plot of the resonances (light) for the full field range. The slope $\gamma/2\pi$ of the field dependent resonances (line) is determined to be $\gamma/2\pi = 28.5$ GHz/T and is identified as the gyromagnetic ratio. The arrow indicates the field position of (a).

9.5.3 Conclusion

We investigated ALD-grown metallic ferromagnets fabricated by the *oxidic process* that has been reported in literature. We focused on the magnetic properties, in particular the magnetic damping, that has not been studied until now. ALD of metal oxides, i.e., FeO and NiO, is an elaborated process. Optimized metallic thin films are obtained by varying the reduction parameters. We find best results, i.e., lowest magnetic damping, when the reduction process of the metal oxides is performed in a reduction chamber at a temperature of 440,° C. The thin films after reduction are often not homogeneous, i.e. holes are formed. We attribute this to the Ostwalt ripening during the reduction process. Necessarily, the reduction process is performed at a high temperature in order to obtain thin films with a low oxygen content. This favors the Ostwalt ripening.

The obtained thin films exhibit a slightly larger electrical resistivity compared to the literature value. They are ferromagnetic and also exhibit an FMR. However, the damping parameter α obtained from in-plane measurements is somewhat larger compared to evaporated Ni thin films by 40%. We attribute the larger values to oxygen and carbon impurities (see Sec. 9.2.1) in the thin films and to the surface roughness. This is also supported by the larger damping parameter α of ALD of Ni compared to evaporated Ni by 40%.

In conclusion, ALD of metallic ferromagnets by the *oxidic process* allows for deposition of ferromagnetic thin films with a relatively low damping. However, the process requires high temperatures during the reduction process. This favors an inhomogeneous growth. Thus, by this process the distinctive capability, the homogeneous growth of ALD is shortened, and the fabrication of nanomaterials becomes more difficult.

9.6 ALD of Ni With In Situ Reduction

The oxidic process with ex situ reduction has already shown satisfying results (see Sec. 9.5). For a further improvement an additional hydrogen step after each ozone step is included. The ALD reactor was specifically designed to offer in situ both, an oxidizing *and* a reducing agent in a sequential manner. As described in Sec. 9.2.2, the chemistry of the adsorption of $NiCp_2$ changes significantly in the presence of H_2 compared to the oxidic process in Sec. 9.2.1. Following Sec. 9.2.2 we expect a lower carbon content due to the hydrogenation of $NiCp_2$. Additionally, the process allows for a shorter or vanishing reduction step, and yields directly a Ni thin film. In the following we present an optimized process for direct ALD of Ni. This process was applied to overgrow prepatterned templates and arrays of nanowires, which were overgrown homogeneously and isotropically. In this thesis we present the capability of the process, verifying the feasibility of producing ferromagnetic nanomaterials.

9.6.1 Process Parameter

The reaction chamber is heated to 300 °C. The solid precursor $NiCp_2$ is heated to a temperature of $100 - 150\,^\circ\mathrm{C}$. Due to the included hydrogen step the process flow [c.f. Eqn. 9.1] reads:

$$\begin{aligned} &C \times [(t_1|t_2 + t_3|t_4) + t_5|t_6] = \\ &C \times (0.8\ \mathrm{s}|4\ \mathrm{s} + 10\ \mathrm{s}|10.0\ \mathrm{s} + 16\ \mathrm{s}|20\ \mathrm{s}), \end{aligned} \tag{9.5}$$

where t_5 and t_6 define the hydrogen pulse duration and the subsequent purge time, respectively. We increased the purging times to inhibit the mixture of H_2 and O_3 in the pumping line (explosion danger). A further exsitu reduction step improved the thin film in some cases even further.

9.6.2 Thin Film Properties

Electrical Properties

The obtained thin films are metallic and conducting. The lowest value of the resistivity is of the order 10 $\mu\Omega$cm and increases by an order of magnitude for lower quality films. The lowest achieved resistivity is similar to the ex situ reduced films (Sec. 9.5). We attribute the higher resistivity compared to the literature value to remaining oxygen or carbon impurities.

A detailed investigation of anisotropic magnetoresistance, see Sec. 3.3, is summarized in the Bachelor thesis of Tobias Stückler. [Stu11]

There, a grooved structure and a flat area are both overgrown by ALD of 40 nm thick Ni (sample TSt_Grooved_Ni), lithographically patterned and physically etched, see Fig. 9.8 (a) and (b). The structured Hall-bar geometry allowed to measure the field dependence of the sheet resistance, i.e. anisotropic magnetoresistance (AMR). An AMR value of 0.4% is detected at the switching field value of 34 mT at a temperature of 4.2 K, see Fig. 9.8 (c). In particular, the homogeneous deposition of Ni in the flanks of the grooves is verified by the comparison of the absolute values of resistance.

Sophisticated AMR measurements were performed on Ni overgrown GaAs nanowires fabricated by Daniel Rüffer, Anna Dalmau, and Prof. Dr. Anna Fontcuberta i Morral (École Polytechnique Fédérale de Lausanne, Lausanne, Switzerland). Single Ni nanotubes were contacted lithographically and the magnetoresistance was measured. [Rue12] The AMR effect was found to be 0.3%. The magnetic configuration was analyzed in detail by magnetoresistance measurements and cantilever magnetometry. [Web12] For a detailed discussion the reader is referred to [Rue12, Rue14].

SEM and TEM Analysis

SEM images of the grooved Hall bar structure (preceding section) show a material in the perpendicular flanks [see Fig. 9.8 (b)], which is supported by the electrical measurements. In Fig. 9.9 the surface of a structured thin film is shown by SEM. The grain size (indicated by arrows in Fig. 9.9) is smaller than 50 nm and the surface is homogeneous, i.e. no holes are detected. This is in contrast to the ex situ reduced thin films, where a grainy structure with holes is observed [c.f. Fig. 9.5]. Transmission electron microscopy and EELS were performed on the Ni overgrown nanowires as depicted in Fig. 9.10 (a) by Prof. Dr. Jordi Arbiol (Institut de Ciència de Materials de Barcelona, Universitat Autònoma de Barcelona, Spain). The grain size is evaluated to be 50 nm. The Ni coating is homogeneous with shallow, distributed holes. By EELS the composition is evaluated to be Ni with Ga and As impurities presented in Fig. 9.10 (b) - (e). An atomic weight of Ni of 80.1 %, O of 13.8 %, and Al of 6.16 % is obtained. Assuming a pure Al_2O_3 stoichiometry this yields an oxygen

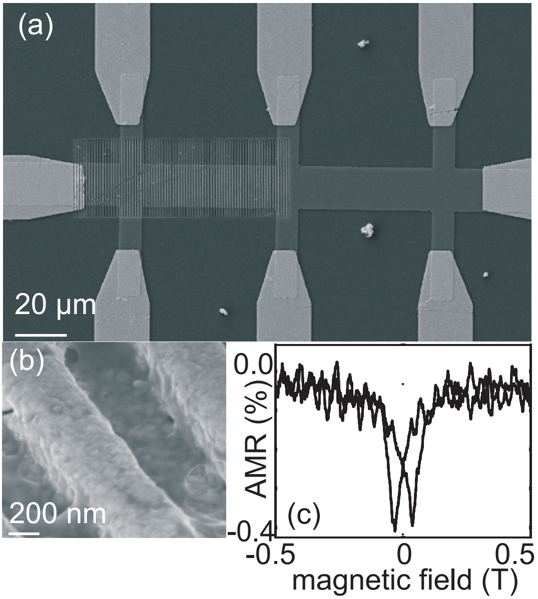

Figure 9.8: (a) SEM image of a Hallbar geometry with one part (sample TSt_Grooved_Ni). A grooved Si template with a period of 4 μm is overgrown by ALD of Ni. The Ni thin film is structured by optical lithography and physical etching. The light areas are contact pads from Au. (b) SEM image of the Ni overgrown grooves. Ni is deposited into the perpendicular areas. (c) Resistance measurement of the grooved structure. An anisotropic magnetoresistance effect of 0.4 % at a temperature of 4.2 K is detected at the switching field value of 34 mT.

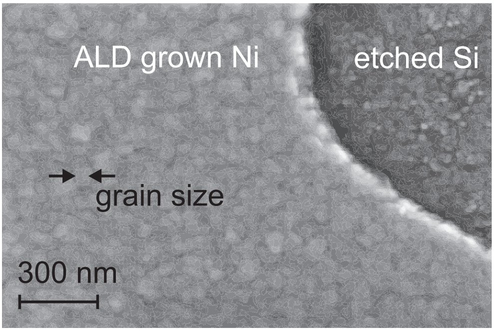

Figure 9.9: (a) SEM image of a structured ALD Ni thin film (sample TSt_Grooved_Ni). The grain size is as small as 50 nm. A homogeneous thin film without holes is observed.

content in the Ni coating of 5.6 %. The determined oxygen content is lower than reported by Bachmann *et al.* [Bac11] for Ni(O) films. They obtained 12% (as grown) and 26% for Ni(O) films oxidized at air.

Ferromagnetic Resonance Measurement

VNA-FMR measurements, see Sec. 5.1, were performed on the in situ reduced Ni thin films (sample RH_114_Ni_2011215), i.e., the reductive process. The signal-to-noise ratio is generally higher compared to ex situ reduced Ni samples. A typical FMR spectrum of an in situ reduced Ni thin film is shown in Fig. 9.11 (a). The presented spectrum is performed at $\mu_0 H = 80$ mT. We observe a linewidth of $\Delta f = 1.2$ GHz at a resonance frequency of $f_0 = 5.4$ GHz. The field dependent FMR measurement is shown in Fig. 9.11 (b). We use Eqn. 5.2 to explain the field dependence. An effective magnetization of $M_{\text{eff}} = 370 \pm 50$ kA/m (assuming a thin film without an in-plane anisotropy) is obtained.

Using Eqns. 2.33 and 5.13 these values correspond to a damping parameter $\alpha = \frac{\Delta\omega}{2\mu_0\gamma(H+M/2)}$. Thus, we obtain $\alpha_{\text{Ni,rp}} = 0.08 \pm 0.01$ for the *reductive process*. Now, we compare both values, the linewidth

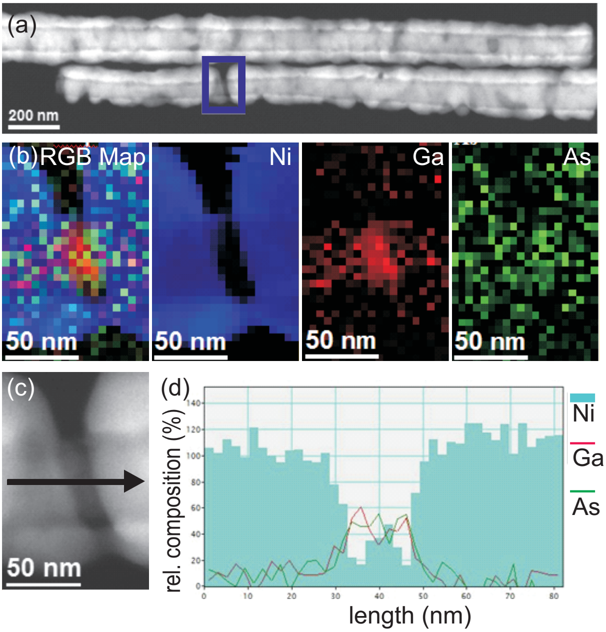

Figure 9.10: (a) TEM image of Ni overgrown GaAs nanowires from EPF Lausanne (group of A. Fontcuberta i Morral). The light areas indicate the Ni shell in contrast to the dark GaAs core. The frame indicates the position of the EELS measurement in (b). Ni, Ga, and As is detected and combined to an RGB map. (c) A cut across the gap (arrow) shows in (d) a high Ni content outside the gap, and a high Ga and As content in the gap.

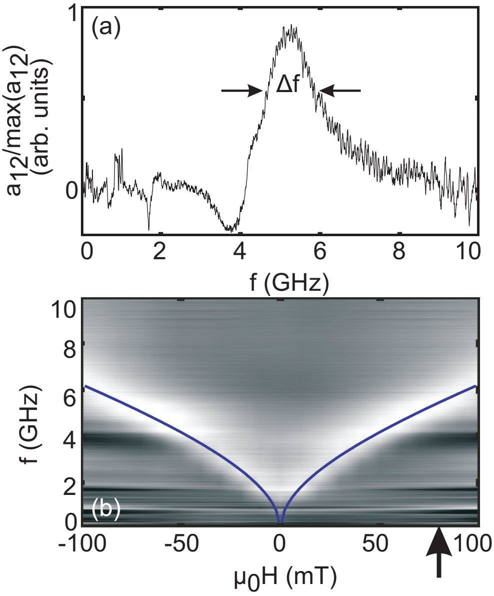

Figure 9.11: (a) VNA-FMR spectra at $\mu_0 H = 80$ mT of an ALD grown Ni with in situ reduction (sample RH_114_Ni_2011215). The signal-to-noise ratio is larger and the linewidth is smaller compared to FMR measurements performed on exsitu reduced thin films, i.e., $\Delta f = 1.2$ GHz. (b) Field dependent FMR measured. The blue line is a fit by the Kittel equation that yields an effective magnetization of $M_{\mathrm{eff}} = 370 \pm 50$ kA/m. The perpendicular arrow at $\mu_0 H = 80$ mT indicates the position of the spectra in (a)

and the effective magnetization, with the ex situ reduced sample, and an evaporated reference sample (by physical vapour deposition). Typical effective magnetizations from different samples fabricated by the reductive process are between $M_{\mathrm{eff}} = 300$ kA/m and $M_{\mathrm{eff}} = 400$ kA/m. This is similar to the oxidic process, and smaller compared to the reference sample. As reported above the damping parameter for the ex situ (evaporated) Ni sample is $\alpha_{\mathrm{Ni,op}} = 0.10 \pm 0.01$ ($\alpha_{\mathrm{Ni,evap}} = 0.06 \pm 0.01$). Thus, we find a reduced damping α for the novel process with in situ reduction compared to the conventional oxidic process, which is still larger by 33% compared to the reference sample.

9.6.3 Conclusion

In summary, we show the direct ALD of Ni by a novel process, i.e. a *reductive process*, where the reduction step is included into the ALD cycle. We focused on the electrical and magnetic properties. The obtained thin films exhibit a slightly larger electrical resistivity compared to the literature value. The high quality of the thin films allows to investigate the AMR effect in a grooved structure and in a ferromagnetic nanotube. Also the magnetic states in Ni overgrown nanowires are studied by magnetoresistance measurements. The thin films are ferromagnetic and also exhibit an FMR. The damping parameter α obtained from in-plane measurements is somewhat larger compared to evaporated Ni thin films by 33%. We attribute the larger values compared to the literature values to oxygen and carbon impurities (see Sec. 9.2.2) in the thin films. In particular, the thin films are homogeneous, i.e., no holes are observed, and show a grain size smaller than 50 nm. We attribute the higher quality of the thin films to the shorter or vanishing ex situ reduction step, which avoids the Ostwalt ripening. In conclusion, ALD of metallic ferromagnets by the *reductive process* allows for deposition of ferromagnetic thin films with a relatively low damping. Additionally, the process is capable of a homogeneous deposition of ferromagnetic material. The fabrication of nanomaterials becomes feasible. Focusing on ferromagnetic nanomaterials, the damping still might be too large.

9.7 ALD of FeNi With In Situ Reduction

The alloy $Ni_{80}Fe_{20}$ (permalloy) is known to be a low damping metallic ferromagnet ($\alpha \sim 0.005$). [Twi03] In order to further improve the magnetic damping observed on the ALD-grown thin films, we established a novel process, where we deposit mixed metallic ferromagnetic thin films, that contain Ni and Fe. Following Sec. 9.2.3 the already presented precursors $FeCp_2$ and $NiCp_2$ are promising candidates for an alloy process. Both precursors exhibit similar stability (decomposition at about 180 °C), they are both oxidized by ozone, and ALD works best at the same temperature of 300 °C. One obstacle is the different reactivities of hydrogen with Ni and hydrogen with Fe (c.f. Sec. 9.2.3). We take this difference into account by applying a process with in situ reduction as presented in Sec. 9.6. The applied *reductive* process ensures a continuous reduction of the two elements. Following Sec. 9.2.3, the catalytic property of Ni is exploited to reduce the stable FeO bond.

In this section we investigate a novel ALD process that allows to deposit mixed ferrmagnetic thin films. We show evidences, that the obtained FeNi thin films form alloys.

9.7.1 Process Parameter

For ALD of mixed FeNi thin films we adapt the process introduced in Sec. 9.6. Additionally, we impose a supercycle on the process of Sec. 9.6. This allows us to control the deposited amount of Fe and Ni. We developed the process:

$$C \times [(m \times (\mathrm{NiCp_2} + \mathrm{O_3}) + k \times \mathrm{H_2}) + n \times (\mathrm{FeCp_2} + \mathrm{O_3}) + l \times \mathrm{H_2})]. \quad (9.6)$$

Here, the purge steps are not listed. The purge steps are equal to Sec. 9.6. The values m, n define the number of employed precursor pulses, the numbers k, l define the reduction steps.

We performed over 40 processes and varied the parameters m, k, n, and l. Deposition processes with swapped places of $FeCp_2$ and $NiCp_2$ are performed. The results are discussed in the following section.

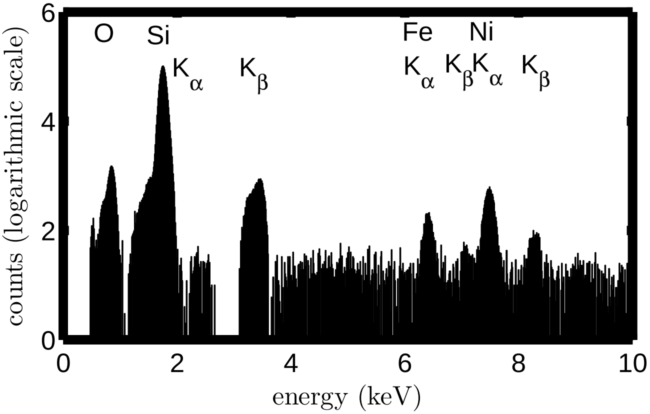

Figure 9.12: EDX data measured on sample NiFe_20120302. The K_α and K_β lines of the detected elements are marked. Fe and Ni peaks are observed. The composition is determined to be X = 16%. Pronounced substrate peaks of Si are detected.

9.7.2 Thin Film Properties

Electrical Properties

Metallic thin films are obtained only in the regime of composition $X = c_{Fe}/(c_{Fe} + c_{Ni}) < 0.5$. The obtained metallic thin films exhibit a resistivity of 100 $\mu\Omega$cm. A further reduction step improved the resistivity in some cases even further. The resistivity is larger compared to the ALD grown pure Ni thin films. The literature value for 10 nm thick thin films is clearly smaller and amounts to 31 $\mu\Omega$cm. [May74] We attribute the larger resistivity to incorporated impurities.

Composition Analysis

The composition is crucial for this process and is investigated by different techniques: ICP-AES[6] and EDX[7] measure the concentrations $c_{\mathrm{Fe,Ni}}$ of Fe or Ni, respectively. The chemical analysis ICP-AES is highly sensitive on metals, but not on oxygen, nitrogen or carbon. ICP-AES verified the existence of Fe and Ni in the thin film. We analyzed the same samples by EDX, that is (besides Fe and Ni) sensitive on oxygen. $c_{\mathrm{Fe,Ni}}$ are detected equivalently to ICP-AES.

As already mentioned, we fabricated several samples with varying parameters m, k, n, and l. A major influence exhibited the parameters m and n. The larger the nominal composition $n/(n+m)$, the larger the final composition X of the thin film. We find discrepancies between nominal and measured composition, in that the nominal value is always larger compared to the measured X. We find X ranging from 0% to 50%. The discrepancy between $n/(n+m)$ and X is increasing for increasing values of X. Exemplarily, for X = 50% the nominal composition was $n/(n+m) = 0.88$.

A second important impact have the parameters k and l. We varied the performed deposition steps m and n per reduction step, i.e. we performed several deposition cycles per reduction step. We found an improved film quality in terms of conductivity and signal-to-noise ratio of the FMR with an increasing number of reduction steps. Exemplarily, we show data from a sample with the nominal composition

---

[6] Mikroanalytischer Labor Pascher, Remagen, Germany

[7] Anwenderzentrum Material- und Umweltforschung (AMU), Augsburg, Germany

$n/(n+m) = 0.66$ that is near the desired FeNi ratio of permalloy (data from sample NiFe_20120302). The process was as follows:

$$400 \times [(2 \times (\mathrm{FeCp_2} + \mathrm{O_3}) + 1 \times \mathrm{H_2}) + 1 \times (\mathrm{NiCp_2} + \mathrm{O_3}) + 1 \times \mathrm{H_2})]. \quad (9.7)$$

Here, in total 1200 injections of metallocene precoursers are performed. We show EDX data obtained on sample NiFe_20120302 in Fig. 9.12. There, the K_α and K_β lines of the detected elements are shown. Also Fe and Ni peaks are observed. The composition is determined to be X = 16%. We attribute the relatively low Fe content in contrast to the nominal composition $n/(n+m) = 0.66$ to technical deficiencies of the process, e.g. a stable precursor supply over 10 h was not ensured. Additionally, a full adsorption of $\mathrm{FeCp_2}$ may be inhibited (see Sec. 9.2.3). Also oxygen is detected. It has a relative content of 18% to 27%. This amount of oxygen is partly attributed to the native oxide on Si and to the 5 nm thick seed layer of $\mathrm{Al_2O_3}$. A detailed study of oxygen and carbon impurities has to been done insitu and was not available throughout this thesis.

Ferromagnetic Resonance Measurement

VNA-FMR measurements, see Sec. 5.1, were performed on all FeNi thin films. We present results obtained on sample TS_FeNi3366. FeNi thin films show a larger signal-to-noise ratio of the FMR measurements compared to data obtained by the processes in Secs. 9.5 and 9.6. In Fig. 9.13 (a) a typical FMR behavior of the sample with a nominal composition of $n/(n+m) = 0.33$ is presented. The measurement is performed at $\mu_0 H = 70$ mT. As described in Sec. 5.1 we extract the resonance frequency f_0, and the linewidth Δf marked in Fig. 9.13 (a). The linewidth amounts to $\Delta f = 0.67$ GHz at a resonance frequency of $f_0 = 6.2$ GHz. A typical field dependent measurement is shown in Fig. 9.13 (b). Using Eqn. 5.2 the effective magnetization M_eff is determined. The effective magnetization amounts to $M_\mathrm{eff} = 620 \pm 50$ kA/m. The determined effective magnetization is larger in comparison to the values obtained on Ni thin films, see Secs. 9.5 and 9.6. We attribute this to the Fe content. Comparing to Sec. 5.1, where evaporated Py is investigated we find a lower value of the effective magnetization in ALD grown thin films

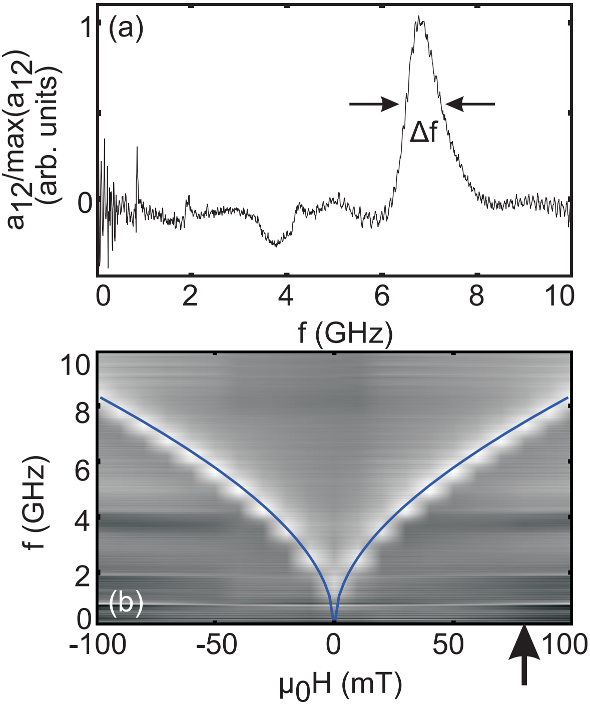

Figure 9.13: (a) Broadband VNA-FMR measurement at $\mu_0 H = 70$ mT on sample TS_FeNi3366. The resonance frequency is $f = 6.2$ GHz and the linewidth $\Delta f = 0.67$ GHz. (b) Field dependent measurement with marked (cross) maximum positions. The blue line is a fit by the Kittel equation that yields an effective magnetization of $M_{\mathrm{eff}} = 620 \pm 50$ kA/m. The perpendicular arrow at $\mu_0 H = 70$ mT indicates the position of the spectra in (a)

by about 20 %. Using Eqns. 2.33 and 5.13 these values correspond to a damping parameter $\alpha_{\mathrm{FeNi}} = \frac{\Delta\omega}{2\mu_0\gamma(H+M/2)} = 0.03 \pm 0.01$. This is lower by a factor of almost 3 compared to ALD grown Ni samples. We also performed measurements with the applied field being constant at $\mu_0 H = 100$ mT, and the angle η is rotating. This provides information about in-plane anisotropies. No ALD grown sample exhibits an angular dependence of the resonance frequency, i.e., they exhibit a constant resonance frequency when rotating η (not shown). We attribute this to a magnetically isotropic thin film without an in-plane anisotropy. This is caused by the isotropical growth of ALD.

Data obtained on the sample TS_FeNi3366 for the magnetic field applied perpendicular to the thin film (out-of-plane) is presented in Fig. 9.14. The measurements were performed by Thomas Schwarze. A resonance is detected at $f_{\mathrm{res}} = 10.2$ GHz for a magnetic field $\mu_0 H = 0.9$ T [c.f. Fig. 9.14 (a)]. The linewidth amounts to $\Delta f = 2.1$ GHz. In Fig. 9.14 (b) the field dependence is presented. We use Eqn. 2.40 to analyze the data. The slope of the field dependence of the resonances yields γ. At a magnetic field $\mu_0 H > 1.4$ T the gyromagnetic ratio is determined to $\gamma/2\pi = 28.5$ GHz/T. We find a point of strongly changing slope $f_{\mathrm{res}}(H)$ at $\mu_0 H \simeq 0.8 \pm 0.1$ T. This value is a measure of the effective magnetization $M_{\mathrm{eff}} = 0.64 \pm 0.08$ kA/m, which supports the value obtained above. As the measurements lacks in the typical minimum behavior, [Col11] this is an indication for surface corrugation.

9.7.3 Effective Magnetization of ALD Grown Alloy Thin Films

In the following we analyse the data obtained in the subsections Composition analysis and Ferromagnetic Resonance Measurement. In Fig. 9.15 the effective magnetization of different samples is plotted versus its composition X. The horizontal errorbars account for the accuracy of the measurement techniques for X, i.e. EDX and ICP-AES. The perpendicular errorbars account for the accuracy of the M_{eff} determination by FMR. In the regime X > 0.5 ALD of FeNi was not possible. The effective magnetization increases with increasing X. Strikingly, a nearly linear dependence of the effective magnetization and composition X is observed. The saturation magnetization of alloys typically depends on their composition. [DB86, Jil88, Nic02]

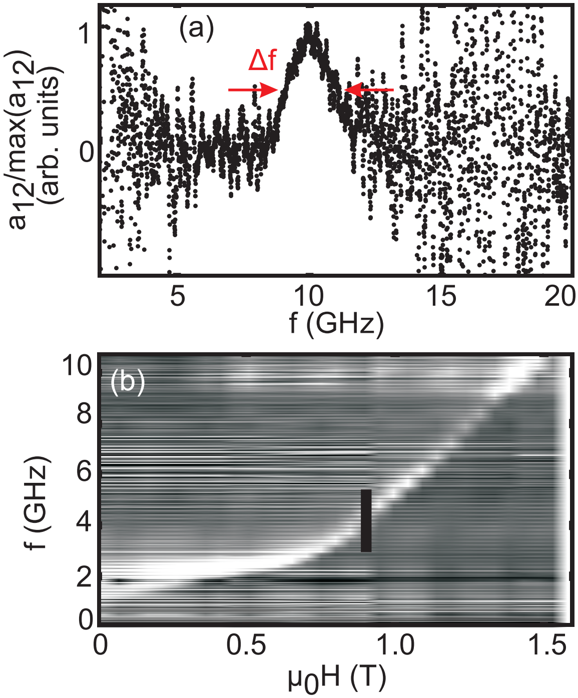

Figure 9.14: (a) VNA-FMR of sample TS_FeNi3366 at $f_{\mathrm{res}} = 10.2$ GHz for a magnetic field $\mu_0 H = 0.9$ T is applied out-of-plane. The linewidth amounts to $\Delta f = 2.1$ GHz. (b) The field dependence exhibits a change of slope at $\mu_0 H \simeq 0.8$ T. The black perpendicular line indicates the position of the spectrum from (a).

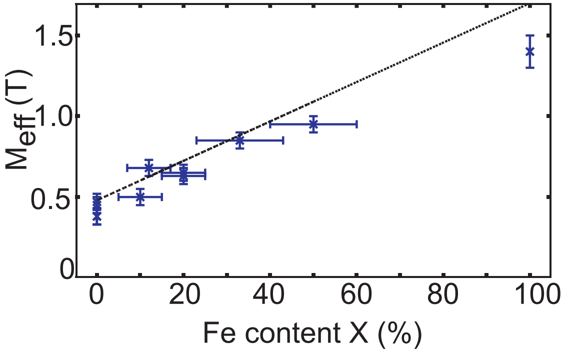

Figure 9.15: The dependence of the effective magnetization of different samples on the measured, relative Fe content X is shown. X is measured by EDX and ICP-AES, where the errorbars account for the accuracy of the measurement techniques. The dotted line is the literature value. The perpendicular errorbars account for the accuracy of the determination of M_{eff}.

In case of an FeNi alloy a linear dependence of the saturation magnetization versus the composition X has been reported, i.e., M_{s} of Ni rises almost monotonically upon the addition of Fe. [DB86] Additionally, the FMR of all deposited layers exhibited only one FMR. In contrast, from a multilayered or segregated ferromagnetic thin film from two different elements, two separated ferromagnetic resonances are expected. This allows to propose the alloy formation of Fe and Ni in the ALD grown thin films.

9.7.4 Conclusion

In summary, we show the ALD of FeNi alloy thin films by a novel process. Key is an included reduction step after the ozone injection in the ALD cycle. We focused on the composition of the films and its magnetic properties. The obtained thin films exhibit a larger signal-to-noise ratio of the FMR. The damping α is smaller compared to the oxidic and reductive processes of Ni deposition presented in Secs. 9.5 and 9.6 by over 50%. Studying the composition and the effective magnetization suggest the formation of the alloy FeNi. We attribute the smaller magnetic damping to the alloy formation. FeNi alloy is known to be a low damping ferromagnetic metal. The process is promising for the fabrication of ferromagnetic nanomaterials as it allows to conformally deposit a low damping ferromagnetic material onto a (prepatterned) nanotemplate. A further improvement is expected by decreasing the process temperature, to obtain even smoother thin films. In situ measurements of thin films, in particular impurity measurement of carbon and oxygen should be done to improve the knowledge about the thin film composition. However, the very long process durations ($\simeq$ 24 h) led to instabilities of the ALD regarding the precursor supply for several hours. An optimized precursor supply would improve the process significantly.

10 Summary and Outlook

In this thesis phenomena of spin waves in arrays of nanowires, so called one dimensional magnonic crystals (1D MCs), and atomic layer deposition grown ferromagnets have been investigated. Arrays of nanowires were fabricated by optical lithography and electron beam lithography. A subsequent lithography process with an accurate alignment was the key to obtain a high resolution in the nanometer regime. The samples were investigated by broadband spectroscopy in the GHz regime. The all-electrical spin wave spectroscopy (AESWS) technique was developed further. Primary focus was put on the control of the magnetic configuration in 1D MCs. By tailoring the samples and using a particular magnetic history we were able to control the magnetization of single nanowires. This enabled us to impose an artificial magnetic configuration upon the 1D MCs.

We analyzed propagating spin waves perpendicular to the nanowires, in particular across the air gaps. There, the focus was put on novel effects of propagating spin waves, such as the reciprocal excitation of Damon-Eshbach-like spin waves. Spin wave band structures were simulated by Plane Wave Method and micromagnetic simulations. The influence of a magnetic defect, that is a single antiparallel magnetized nanowire in a homogeneously magnetized environment, was investigated. By micromagnetic simulations the magnetic defect was found to act as a semitransparent mirror for spin waves, which is explained by the contributions due to the out-of-plane interaction of vicinal nanowires.

The control of the magnetic configuration, in particular of single nanowires, makes 1D MCs promising for future devices. The magnetization direction of a nanowire represents a bit and is therefore the basic module of storage of information. A promising next step is the control of the magnetic state of single nanowires by moving domain walls through the nanowire by an electrical current, similar to the racetrack memory. The large group velocities and the control of the output level by the magnetic state creates the prespective of logic devices based on the control of spin wave propagation.

Still for the excitation and detection of spin waves remains room for improvement. One issue is the relatively strong electromagnetic coupling between antennas. The antenna design has to be adapted to the relevant application, e.g. for TR-AESWS antennas can be positioned close to each other, as the electromagnetic crosstalk can be discriminated. In contrast, for FR-AESWS the distance and shielding between the structures is crucial. Here electromagnetic simulations and fast prototyping by electron beam lithography might help to improve the measurement setup. Recent, seminal work on spin-transfer oscillators gives hope for efficient spin wave excitation by an electrical current.

A second target of the thesis was the development and analysis of atomic layer deposition of ferromagnetic material. The investigation of the magnetostatic and magnetodynamic properties of atomic layer deposited ferromagnetic material was performed. By introducing a further hydrogen step into the ALD cycle and by using an alloy process for FeNi deposition, we were able to significantly reduce the magnetic damping. ALD coated prestructured templates, e.g. nanowires, showed intriguing physical results. A promising step for ALD of Ni and NiFe alloys is a reduction of the deposition temperature. This gives hope for smoother thin films and an improved damping. Furthermore, ALD of Ni and NiFe alloys on templates may be altered due to the corrugated surfaces. Here, deposition parameters have to be adapted in order to yield a homogeneous and isotropic coating. For further improvement it might be necessary to change the precursor materials for further applications.

List of Figures

Bibliography

[Aal03] T. Aaltonen, A. Rahtu, M. Ritala, and M. Leskelä: *Reaction Mechanism Studies on Atomic Layer Deposition of Ruthenium and Platinum*, Electrochem. Solid-State Lett. **6**, C130 (2003).

[Agi04] Agilent Technologies: *Network Analyzer Basics* (2004).

[Aha98] A. Aharoni: *Demagnetizing factors for rectangular ferromagnetic prisms*, J. Appl. Phys. **83**, 3432 (1998).

[And97] D. Anderson, L. Smith, and J. Gruszynski: *S-Parameter Techniques for Faster, More Accurate Network Design*, Hewlett Packard, application note 95-1 edn. (1997).

[Arg55] P. N. Argyres: *Theory of the Faraday and Kerr Effects in Ferromagnetics*, Phys. Rev. **97**, 334 (1955).

[Ari99] R. Arias, and D. L. Mills: *Extrinsic contributions to the ferromagnetic resonance response of ultrathin films*, Phys. Rev. B **60**, 7395 (1999).

[Au12] Y. Au, E. Ahmad, O. Dmytriiev, M. Dvornik, T. Davison, and V. V. Kruglyak: *Resonant microwave-to-spin-wave transducer*, Appl. Phys. Lett. **100**, 182404 (2012).

[Bue00] O. Büttner, M. Bauer, S. O. Demokritov, B. Hillebrands, Y. S. Kivshar, V. Grimalsky, Y. Rapoport, and A. N. Slavin: *Linear and nonlinear diffraction of dipolar spin waves in yttrium iron garnet films observed by space- and time-resolved Brillouin light scattering*, Phys. Rev. B **61**, 11576 (2000).

[Bab08] K. Baberschke: *Why are spin wave excitations all important in nanoscale magnetism?*, Phys. Status Solidi (b) **245**, 174 (2008).

[Bab11] K. Baberschke: *Ferromagnetic resonance in nanostructures, rediscovering its roots in paramagnetic resonance*, J. Phys.: Conf. Ser. **324**, 012011 (2011).

[Bac07] J. Bachmann, Jing, M. Knez, S. Barth, H. Shen, S. Mathur, U. Gösele, and K. Nielsch: *Ordered Iron Oxide Nanotube Arrays of Controlled Geometry and Tunable Magnetism by Atomic Layer Deposition*, J. Am. Chem. Soc. **129**, 9554 (2007).

[Bac09] J. Bachmann, J. Escrig, K. Pitzschel, J. M. M. Moreno, J. Jing, D. Görlitz, D. Altbir, and K. Nielsch: *Size effects in ordered arrays of magnetic nanotubes: Pick your reversal mode*, J. Appl. Phys. **105**, 07B521 (2009).

[Bac11] J. Bachmann, A. Zolotaryov, O. Albrecht, S. Goetze, A. Berger, D. Hesse, D. Novikov, and K. Nielsch: *Stoichiometry of Nickel Oxide Films Prepared by ALD*, Chem. Vap. Deposition **17**, 177 (2011).

[Bae11] C. Bae, H. Shin, and K. Nielsch: *Surface modification and fabrication of 3D nanostructures by atomic layer deposition*, MRS Bulletin **36**, 887 (2011).

[Bai03a] M. Bailleul, D. Olligs, and C. Fermon: *Micromagnetic Phase Transitions and Spin Wave Excitations in a Ferromagnetic Stripe*, Phys. Rev. Lett. **91**, 137204 (2003).

[Bai03b] M. Bailleul, D. Olligs, and C. Fermon: *Propagating spin wave spectroscopy in a permalloy film: A quantitative analysis*, Appl. Phys. Lett. **83**, 972 (2003).

[Bao08] M. Bao, K. Wong, A. Khitun, J. Lee, Z. Hao, K. L. Wang, D. W. Lee, and S. X. Wang: *Determining wave vector and material property from the phase-shift of spin-wave propagation*, Europhys. Lett. **84**, 27009 (2008).

[Bar10] S. Barman, A. Barman, and Y. Otani: *Controlled propagation of locally excited vortex dynamics in linear nanomagnet arrays*, J. Phys. D: Appl. Phys. **43**, 335001 (2010).

[Ber08] D. V. Berkov, and N. L. Gorn: *Micromagus - software for micromagnetic simulations*, http://www.micromagus.de (2008).

[Bil08] C. Bilzer: *Microwave susceptibility of thin ferromagnetic films: metrology and insight into magnetization dynamics*, Ph.D. thesis, Universite Paris-Sud 11 (2008).

[Bir12] D. R. Birt, K. An, M. Tsoi, S. Tamaru, D. Ricketts, K. L. Wong, P. K. Amiri, K. L. Wang, and X. Li: *Deviation from exponential decay for spin waves excited with a coplanar waveguide antenna*, Appl. Phys. Lett. **101**, 252409 (2012).

[Blu01] S. Blundell: *Magnetism in Condensed Matter*, Oxford University Press, Oxford, 2001.

[Boz68] R. M. Bozorth: *Ferromagnetism*, D. VAN Nostrand Comany, 1968.

[Bra10] F. Brandl: *Spin waves in antidot lattices on suspended membranes and temperature dependent effects in permalloy thin films*, Master's thesis, Technische Universität München (2010).

[Bri99a] L. Brissonneau, D. de Caro, D. Boursier, R. Madar, and C. Vahlas: *MOCVD-Processed Ni Films from Nickelocene. Part II: Carbon Content of the Deposits*, Chem. Vap. Deposition **5**, 143 (1999).

[Bri99b] L. Brissonneau, A. Reynes, and C. Vahlas: *MOCVD Processed Ni Films from Nickelocene. Part III: Gas Phase Study and Deposition Mechanisms*, Chem. Vap. Deposition **5**, 281 (1999).

[Bri99c] L. Brissonneau, and C. Vahlas: *MOCVD-Processed Ni Films from Nickelocene. Part I: Growth Rate and Morphology*, Chem. Vap. Deposition **5**, 135 (1999).

[Bri00] L. Brissonneau, R. Sahnoun, C. Mijoule, and C. Vahlas: *Investigation of Nickelocene Decomposition during Chemical Vapor Deposition of Nickel*, J. Electrochem. Soc. **147**, 1443 (2000).

[Chi97] S. Chikazumi: *Physics of Ferromagnetism*, Oxford Science Publications, 1997.

[Cho10] Y. T. Chong, E. M. Y. Yau, K. Nielsch, and J. Bachmann: *Direct Atomic Layer Deposition of Ternary Ferrites with Various Magnetic Properties*, Chem. Mat. **22**, 6506 (2010).

[Cho11] Y. T. Chong, M. Y. E. Yau, Y. Yang, M. Zacharias, D. Görlitz, K. Nielsch, and J. Bachmann: *Superparamagnetic behavior in cobalt iron oxide nanotube arrays by atomic layer deposition*, J. Appl. Phys. **110**, 043930 (2011).

[Chr74] K. Christmann, O. Schober, G. Ertl, and M. Neumann: *Adsorption of hydrogen on nickel single crystal surfaces*, J. Chem. Phys. **60**, 4528 (1974).

[Chr10] S. Christensen, and J. W. Elam: *Atomic Layer Deposition of Ir-Pt Alloy Films*, Chem. Mater. **22**, 2517 (2010).

[Col11] F. della Colletta: *Temperaturabhängige Sättigungsmagnetisierung und Oberflächenanistropie von dünnen Permalloy-Filmen mit und ohne Al-Schutzschicht*, Master's thesis, Technical University Munich (2011).

[Cou04] G. Counil, J.-V. Kim, T. Devolder, C. Chappert, K. Shigeto, and Y. Otani: *Spin wave contributions to the high-frequency magnetic response of thin films obtained with inductive methods*, J. Appl. Phys. **95**, 5646 (2004).

[Cov02] M. Covington, T. M. Crawford, and G. J. Parker: *Time-Resolved Measurement of Propagating Spin Waves in Ferromagnetic Thin Films*, Phys. Rev. Lett. **89**, 237202 (2002).

[Cov04] M. Covington, T. M. Crawford, and G. J. Parker: *Erratum: Time-Resolved Measurement of Propagating Spin Waves in Ferromagnetic Thin Films [Phys. Rev. Lett. 89, 237202 (2002)]*, Phys. Rev. Lett. **92**, 089903 (2004).

[Dam61] R. Damon, and J. Eshbach: *Magnetostatic modes of a ferrite slab*, J. Phys. Chem. Solids **19**, 308 (1961).

[Dau07] M. Daub, M. Knez, U. Gösele, and K. Nielsch: *Ferromagnetic nanotubes by atomic layer deposition in anodic alumina membranes*, 10th Joint MMM/Intermag Conference **101**, 09J111 (2007).

[DB86] H. W. D. Bonnenberg, K. A. Hempel: *1.2.1 Alloys between Fe, Co or Ni*, vol. 19a, SpringerMaterials - The Landolt-Börnstein Database, 1986.

[Dem01] S. Demokritov, B. Hillebrands, and A. Slavin: *Brillouin light scattering studies of confined spin waves: linear and nonlinear confinement*, Phys. Rep. **348**, 441 (2001).

[Dem04] S. O. Demokritov, A. A. Serga, A. André, V. E. Demidov, M. P. Kostylev, B. Hillebrands, and A. N. Slavin: *Tunneling of Dipolar Spin Waves through a Region of Inhomogeneous Magnetic Field*, Phys. Rev. Lett. **93**, 047201 (2004).

[Dem09] V. E. Demidov, M. P. Kostylev, K. Rott, P. Krzysteczko, G. Reiss, and S. O. Demokritov: *Excitation of microwaveguide modes by a stripe antenna*, Appl. Phys. Lett. **95**, 112509 (2009).

[Den99] M. Denk: *Inorganic Chemistry II: Organometallics*, Lecture (1999).

[Din11a] J. Ding, M. Kostylev, and A. O. Adeyeye: *Magnetic hysteresis of dynamic response of one-dimensional magnonic crystals consisting of homogenous and alternating width nanowires observed with broadband ferromagnetic resonance*, Phys. Rev. B **84**, 054425 (2011).

[Din11b] J. Ding, M. Kostylev, and A. O. Adeyeye: *Magnonic Crystal as a Medium with Tunable Disorder on a Periodical Lattice*, Phys. Rev. Lett. **107**, 047205 (2011).

[Due09] G. Dürr: *Spin Dynamics in Permalloy Antidot Lattices: from Standing to Propagating Spin Waves*, Master's thesis, Technische Universität München (2009).

[Due12] G. Duerr, K. Thurner, J. Topp, R. Huber, and D. Grundler: *Enhanced Transmission through Squeezed Modes in a Self-Cladding Magnonic Waveguide*, Phys. Rev. Lett. **108**, 227202 (2012).

[Ela03] J. W. Elam, D. Routkevitch, P. P. Mardilovich, and S. M. George: *Conformal Coating on Ultrahigh-Aspect-Ratio Nanopores of Anodic Alumina by Atomic Layer Deposition*, Chem. Mat. **15**, 3507 (2003).

[Ela07] J. W. Elam, J. A. Libera, M. J. Pellin, and P. C. Stair: *Spatially controlled atomic layer deposition in porous materials*, Appl. Phys. Lett. **91**, 243105 (2007).

[Fae11] M. Fähnle, and C. Illg: *Electron theory of fast and ultrafast dissipative magnetization dynamics*, J. Phys.: Condens. Matter **23**, 493201 (2011).

[Fal12] L. Fallarino, M. Madami, G. Duerr, D. Grundler, G. Gubbiotti, S. Tacchi , and G. Carlotti: *Propagation of spin waves excited in a Permalloy film by a finite-ground coplanar waveguide: a combined phase-sensitive micro-focused Brillouin light scattering and micromagnetic study*, IEEE Trans. Mag. (2012).

[Fil12] Y. Filimonov, E. Pavlov, S. Vystostkii, and S. Nikitov: *Magnetostatic surface wave propagation in a one-dimensional magnonic crystal with broken translational symmetry*, Appl. Phys. Lett. **101**, 242408 (2012).

[Geo10] S. M. George: *Atomic Layer Deposition: An Overview*, Chem. Rev. **110**, 19947596 (2010).

[Gie05] F. Giesen: *Magnetization Dynamics of Nanostructured Ferromagnetic Rings and Rectangular Elements*, Ph.D. thesis, Universität Hamburg (2005).

[Gil55] T. Gilbert: *A Lagrangian Formulation of the Gyromagnetic Equation of the Magnetization Field*, Phys. Rev. **100**, 1243 (1955).

[Gro04] M. D. Groner, F. H. Fabreguette, J. W. Elam, and S. M. George: *Low-Temperature Al_2O_3 Atomic Layer Deposition*, Chem. Mater. **16**, 639 (2004).

[Gub05] G. Gubbiotti, S. Tacchi, G. Carlotti, P. Vavassori, N. Singh, S. Goolaup, A. O. Adeyeye, A. Stashkevich, and M. Kostylev: *Magnetostatic interaction in arrays of nanometric permalloy wires: A magneto-optic Kerr effect and a Brillouin light scattering study*, Phys. Rev. B **72**, 224413 (2005).

[Gub07] G. Gubbiotti, S. Tacchi, G. Carlotti, N. Singh, S. Goolaup, A. O. Adeyeye , and M. Kostylev: *Collective spin modes in monodimensional magnonic crystals consisting of dipolarly coupled nanowires*, Appl. Phys. Lett. **90**, 092503 (2007).

[Gub10] G. Gubbiotti, S. Tacchi, M. Madami, G. Carlotti, A. O. Adeyeye, and M. Kostylev: *Brillouin light scattering studies of planar metallic magnonic crystals*, J. Phys. D **43**, 264003 (2010).

[Gur96] A. Gurevich, and G. Melkov: *Magnetization oscillations and waves*, CRC Press, Boca Raton, 1996.

[Gus02] K. Y. Guslienko, S. O. Demokritov, B. Hillebrands, and A. N. Slavin: *Effective dipolar boundary conditions for dynamic magnetization in thin magnetic stripes*, Phys. Rev. B **66**, 132402 (2002).

[Ham09] J. Hämäläinen, E. Puukilainen, M. Kemell, L. Costelle, M. Ritala, and M. Leskelä: *Atomic Layer Deposition of Iridium Thin Films by Consecutive Oxidation and Reduction Steps*, Chem. Mat. **21**, 4868 (2009).

[Ham11] J. Hämäläinen, T. Hatanpaa, E. Puukilainen, T. Sajavaara, M. Ritala, and M. Leskelä: *Iridium metal and* *iridium oxide thin films grown by atomic layer deposition at low temperatures*, J. Mater. Chem. **21**, 16488 (2011).

[Har99] U. Hartmann: *Magnetic Force Microscopy*, Annu. Rev. Mater. Sci. **29**, 53 (1999).

[Her04] R. Hertel, W. Wulfhekel, and J. Kirschner: *Domain-wall induced phase shifts in spin waves.*, Phys. Rev. Lett. **93**, 257202 (2004).

[Hil65] M. Hillert: *On the theory of normal and abnormal grain growth*, Acta Metall. **13**, 227 (1965).

[Hil02] B. Hillebrands, and K. Ounadjela: *Spin Dynamics in Confined Magnetic Structures*, Springer, Berlin, 2002.

[Hub13a] R. Huber, M. Krawczyk, T. Schwarze, H. Yu, G. Duerr, S. Albert, and D. Grundler: *Reciprocal Damon-Eshbach-type spin wave excitation in a magnonic crystal due to tunable magnetic symmetry*, Appl. Phys. Lett. **102**, 012403 (2013).

[Hub13b] R. Huber, T. Schwarze, and D. Grundler: *Subwavelength-wide Nanostripe as a Switchable Semitransparent Mirror for Spin Waves in a Magnonic Crystal*, Phys. Rev. B **88**, 100405(R) (2013).

[JHP01] T. S. Jong-Hee Park (ed.): *Chemical Vapor Deposition*, ASM International, 2001.

[Jil88] D. C. Jiles, T. T. Chang, D. R. Hougen, and R. Ranjan: *Magnetic Properties of Nickel-Copper and Nickel-Cobalt Alloys*, J. Phys. Colloques **49** (1988).

[Joa97] J. Joannopoulos, P. Villeneuve, and S. Fan: *Photonic Crystals*, Sol. Stat. Comm. **102**, 165 (1997).

[Joa08] J. D. Joannopoulos *et al.*: *Photonic Crystals: Molding the Flow of Light*, Princeton Univ. Press., Princeton, 2008, Second edn..

[Koe07] J. Kötzler, D. Görlitz, and F. Wiekhorst: *Strong spin-orbit-induced Gilbert damping and g-shift in iron-platinum nanoparticles*, Phys. Rev. B **76**, 104404 (2007).

[Kal86] B. Kalinikos, and A. Slavin: *Theory of dipole-exchange spin wave spectrum for ferromagnetic films with mixed exchange boundary conditions*, J. Phys. C **19**, 7013 (1986).

[Kal06] S. S. Kalarickal, P. Krivosik, M. Wu, C. E. Patton, M. L. Schneider, P. Kabos, T. J. Silva, and J. P. Nibarger: *Ferromagnetic resonance linewidth in metallic thin films: Comparison of measurement methods*, J. Appl. Phys. **99**, 093909 (2006).

[Kar10] S. K. Karuturi, L. Liu, L. T. Su, Y. Zhao, H. J. Fan, X. Ge, S. He, and A. T. I. Yoong: *Kinetics of Stop-Flow Atomic Layer Deposition for High Aspect Ratio Template Filling through Photonic Band Gap Measurements*, J. Phys. Chem. C **114**, 14843 (2010).

[Kea13] P. S. Keatley, P. Gangmei, M. Dvornik, R. J. Hicken, J. Grollier, and C. Ulysse: *Isolating the Dynamic Dipolar Interaction between a Pair of Nanoscale Ferromagnetic Disks*, Phys. Rev. Lett. **110**, 187202 (2013).

[Khi05] A. Khitun, and K. L. Wang: *Nano scale computational architectures with Spin Wave Bus*, Superlattices Microstruct. **38**, 184 (2005).

[Kit48] C. Kittel: *On the Theory of Ferromagnetic Resonance Absorption*, Phys. Rev. **73**, 155 (1948).

[Kit68] C. Kittel: *Einführung in die Festkörperphysik*, R. Oldenburg, 1968.

[KM07] M. Knez, K. Nielsch, and L. Niinistö: *Synthesis and Surface Engineering of Complex Nanostructures by Atomic Layer Deposition*, Adv. Mater. **19**, 3425 (2007).

[Kno09] H. C. M. Knoops, A. J. M. Mackus, M. E. Donders, M. C. M. van de Sanden, P. H. L. Notten, and W. M. M.

Kessels: *Remote Plasma ALD of Platinum and Platinum Oxide Films*, Electrochem. Solid-State Lett. **12**, G34 (2009).

[Kos05] M. P. Kostylev, A. A. Serga, T. Schneider, B. Leven, and B. Hillebrands: *Spin-wave logical gates*, Appl. Phys. Lett. **87**, 153501 (2005).

[Kos12] M. Kostylev, A. A. Stashkevich, Y. Roussigné, N. A. Grigoryeva, A. A. Mistonov, D. Menzel, N. A. Sapoletova, K. S. Napolskii, A. A. Eliseev, A. V. Lukashin, S. V. Grigoriev, and S. N. Samarin: *Microwave properties of Ni-based ferromagnetic inverse opals*, Phys. Rev. B **86**, 184431 (2012).

[Koz09a] A. Kozhanov, D. Ouellette, Z. Griffith, M. Rodwell, A. P. Jacob, D. W. Lee, S. X. Wang, and S. J. Allen: *Dispersion in magnetostatic CoTaZr spin waveguides*, Appl. Phys. Lett. **94**, 012505 (2009).

[Koz09b] A. Kozhanov, D. Ouellette, M. Rodwell, S. J. Allen, A. P. Jacob, D. W. Lee , and S. X. Wang: *Dispersion and spin wave "tunneling" in nanostructured magnetostatic spin waveguides*, J. Appl. Phys. **105**, 07D311 (2009).

[Kra08] M. Krawczyk, and H. Puszkarski: *Plane-wave theory of three-dimensional magnonic crystals*, Phys. Rev. B **77**, 054437 (2008).

[Kru10] V. V. Kruglyak, S. O. Demokritov, and D. Grundler: *Magnonics*, J. Phys. D: Appl. Phys. **43**, 264001 (2010).

[Kua02] B. K. Kuanr, M. Buchmeier, D. E. Bürgler, and P. Grünberg: *Exchange coupling of molecular-beam-epitaxy-grown Fe/Al/Fe trilayers by dynamic techniques*, J. Appl. Phys. **91**, 7209 (2002).

[Lan35] L. D. Landau, and E. Lifschitz: *On the theory of the dispersion of magnetic permeability in ferromagnetic bodies*, Physik. Z. Sowjetunion **8**, 153 (1935).

[Lan11] T. Langner, B. Obry, P. Pirro, T. Brächer, K. Vogt, B. Leven, and B. Hillebrands: *Spin-wave tunneling through a mechanical gap in a microstructured* $Ni_{81}Fe_{19}$-*stripe*, Annual Report Technische Universität Kaiserslautern p. 69 (2011).

[Lar07] D. Laroze, J. Escrig, P. Landeros, D. Altbir, M. Vázquez, and P. Vargas: *A detailed analysis of dipolar interactions in arrays of bi-stable magnetic nanowires*, Nanotechnology **18**, 415708 (2007).

[LB03] R. G. Lim B.S., A. Rahtu: *Atomic layer deposition of transition metals*, Nature Mater. **2**, 749 (2003).

[Lee09] H.-B.-R. Lee, W.-H. Kim, Y. Park, S. Baik, and H. Kim: *Cobalt and nickel atomic layer depositions for contact applications*, Interconnect Technology Conference, 157 - 158 (2009).

[Len11] B. Lenk, H. Ulrichs, F. Garbs, and M. Münzenberg: *The building blocks of magnonics*, Physics Reports **507**, 107 (2011).

[Les02] M. Leskelä, and M. Ritala: *Atomic layer deposition (ALD): from precursors to thin film structures*, Thin Solid Films **409**, 138, Proceedings of the 2nd Asian Conference on Chemical Vapour Depostion (2002).

[Les11] M. Leskelä: *Challenges in Atomic Layer Deposition*, Wiley-VCH Verlag GmbH & Co. KGaA, 2011.

[Leu93] K. M. Leung: *Photonic Band Gaps and Localization*, Plenum Press, New York, 1993.

[Lu08] H. Lu, G. Scarel, X. Li, and M. Fanciulli: *Thin MnO and NiO films grown using atomic layer deposition from ethylcyclopentadienyl type of precursors*, J. Cryst. Growth **310**, 5464 (2008).

[Mad10] M. Madami, S. Tacchi, G. Gubbiotti, G. Carlotti, F. Montoncello, G. Capuzzo , and F. Nizzoli: *Magnetic normal* *modes of elliptical NiFe nanoring studied by micro-focused Brillouin light scattering*, JPCS **200**, 042008 (2010).

[Mar87] Y. Martin, and H. K. Wickramasinghe: *Magnetic imaging by "force microscopy" with 1000 Å resolution*, Appl. Phys. Lett. **50**, 1455 (1987).

[Mar11] A. B. F. Martinson, M. J. DeVries, J. A. Libera, S. T. Christensen, J. T. Hupp, M. J. Pellin, and J. W. Elam: *Atomic Layer Deposition of Fe_2O_3 Using Ferrocene and Ozone*, J. Phys. Chem. C **115**, 4333 (2011).

[Mav96] R. Mavaddat: *Network Scattering Parameters*, Singapore ; River Edge, N.J. : World Scientific, 1996.

[May74] A. F. Mayadas, J. F. Janak, and A. Gangulee: *Resistivity of Permalloy thin films*, J. Appl. Phys. **45**, 2780 (1974).

[McG07] D. McGrouther, S. McVitie, J. N. Chapman, and A. Gentils: *Controlled domain wall injection into ferromagnetic nanowires from an optimized pad geometry*, Appl. Phys. Lett. **91**, 022506 (2007).

[Mil09] B. Mills: *Ball-and-stick model of ferrocene*, Wikipedia (2009).

[Miy12] T. Miyazaki, and H. Jin: *The Physics of Ferromagnetism*, chap. 11, Springer Berlin Heidelberg, 2012, 384–392.

[ML00] M. J. Mayor-López, H. P. Lüthi, H. Koch, P. Y. Morgantini, and J. Weber: *Coupled-cluster calculations on ferrocene and its protonated derivatives: Towards the final word on the mechanism of protonation of ferrocene?*, J. Chem. Phys. **113**, 8009 (2000).

[Neu08a] S. Neusser, B. Botters, M. Becherer, D. Schmitt-Landsiedel, and D. Grundler: *Spin-wave localization between nearest and next-nearest neighboring holes in an antidot lattice*, Appl. Phys. Lett. **93**, 122501 (2008).

[Neu08b] S. Neusser, B. Botters, and D. Grundler: *Spin wave modes in antidot lattices: Localization, confinement, and field-controlled propagation*, Phys. Rev. B **78**, 087825 (2008).

[Neu09a] T. Neumann, A. A. Serga, B. Hillebrands, and M. P. Kostylev: *Frequency-dependent reflection of spin waves from a magnetic inhomogeneity induced by a surface direct current*, Appl. Phys. Lett. **94**, 042503 (2009).

[Neu09b] S. Neusser, and D. Grundler: *Magnonics: Spin Waves on the Nanoscale*, Adv. Mater. **21**, 2927 (2009).

[Neu10] S. Neusser, G. Duerr, H. G. Bauer, S. Tacchi, M. Madami, G. Woltersdorf, G. Gubbiotti, C. H. Back, and D. Grundler: *Anisotropic Propagation and Damping of Spin Waves in a Nanopatterned Antidot Lattice*, Phys. Rev. Lett. **105**, 067208 (2010).

[Neu11a] S. Neusser: *Spin Waves in Antidot Lattices: From Quantization to Magnonic Crystals*, Ph.D. thesis, Technical University Munich (2011).

[Neu11b] S. Neusser, H. G. Bauer, G. Duerr, R. Huber, S. Mamica, G. Woltersdorf, M. Krawczyk, C. H. Back, and D. Grundler: *Tunable metamaterial response of a* $Ni_{80}Fe_{20}$ *antidot lattice for spin waves*, Phys. Rev. B **84**, 184411 (2011).

[Ngu07] H. T. Nguyen, T. M. Nguyen, and M. G. Cottam: *Dipole-exchange spin waves in ferromagnetic stripes with inhomogeneous magnetization*, Phys. Rev. B **76**, 134413 (2007).

[Ngu11] H. T. Nguyen, and M. G. Cottam: *Microscopic dipole-exchange theory for planar nanostriped magnonic crystals*, J. Phys. D: Appl. Phys. **44**, 315001 (2011).

[Nic02] D. M. C. Nicholson, Y. Wang, and M. Widom: *Calculated Effect of Alloy Additions on the Saturation Magnetization of* $Fe_{0.80}B_{0.20}$, MRS Online Proc. Library **754**, (2002).

[OBr12] L. OBrien, D. E. Read, D. Petit, and R. P. Cowburn: *Dynamic propagation and nucleation in domain wall nanowire devices*, J. Phys.: Condens. Matter **24**, 024222 (2012).

[Par08] S.-J. Park, W.-H. Kim, W. Maeng, Y. Yang, C. Park, H. Kim, K.-N. Lee, S.-W. Jung, and W. Seong: *Effect oxygen exposure on the quality of atomic layer deposition of ruthenium from bis(cyclopentadienyl)ruthenium and oxygen*, Thin Solid Films **516**, 7345 (2008).

[Pat75] C. E. Patton, Z. Frait, and C. H. Wilts: *Frequency dependence of the parallel and perpendicular ferromagnetic resonance linewidth in Permalloy films, 2-36 GHz*, J. Appl. Phys. **46**, 5002 (1975).

[Pir11] P. Pirro, T. Brächer, K. Vogt, B. Obry, H. Schultheiss, B. Leven, and B. Hillebrands: *Interference of coherent spin waves in micron-sized ferromagnetic waveguides*, Phys. Status Solidi (b) **248**, 2404 (2011).

[Pol08] S. Polisetty, J. Scheffler, S. Sahoo, Y. Wang, T. Mukherjee, X. He, and C. Binek: *Optimization of magneto-optical Kerr setup: Analyzing experimental assemblies using Jones matrix formalism*, Rev. Sci. Instrum. **79**, 055107 (2008).

[Pug99] D. L. Pugmire, C. M. Woodbridge, S. Root, and M. A. Langell: *Nickelocene adsorption on single-crystal surfaces*, in *Symposium of the American Vacuum Society*, vol. 17, AVS, 1999, 1581–1586.

[Puu05] R. L. Puurunen: *Surface chemistry of atomic layer deposition: A case study for the trimethylaluminum/water process*, J. Appl. Phys. **97**, 121301 (2005).

[Qiu00] Z. Q. Qiu, and S. D. Bader: *Surface magneto-optic Kerr effect*, Rev. Sci. Instrum. **71**, 1243 (2000).

[Rub88] M. Rubinstein, F. J. Rachford, W. W. Fuller, and G. A. Prinz: *Electrical transport properties of thin epitaxially grown iron films*, Phys. Rev. B **37**, 8689 (1988).

[Rue12] D. Rüffer, R. Huber, P. Berberich, S. Albert, E. Russo-Averchi, M. Heiss, J. Arbiol, A. Fontcuberta i Morral, and D. Grundler: *Magnetic states of an individual Ni nanotube probed by anisotropic magnetoresistance*, Nanoscale **4**, 4989 (2012).

[Rue14] D. Rüffer: Ph.D. thesis, EPFL (2014).

[Rug90] D. Rugar, H. J. Mamin, P. Guethner, S. E. Lambert, J. E. Stern, I. McFadyen , and T. Yogi: *Magnetic force microscopy: General principles and application to longitudinal recording media*, J. Appl. Phys. **68**, 1169 (1990).

[Rus96] D. K. Russell: *Gas-Phase Pyrolysis Mechanisms in Organometallic CVD*, Chem. Vap. Deposition **2**, 223 (1996).

[RV12] J. Romero Vivas, S. Mamica, M. Krawczyk, and V. V. Kruglyak: *Investigation of spin wave damping in three-dimensional magnonic crystals using the plane wave method*, Phys. Rev. B **86**, 144417 (2012).

[Sch08a] T. Schneider, A. A. Serga, B. Leven, B. Hillebrands, R. L. Stamps, and M. P. Kostylev: *Realization of spin-wave logic gates*, Appl. Phys. Lett. **92**, 022505 (2008).

[Sch08b] H. Schultheiss, C. W. Sandweg, B. Obry, S. Hermsdörfer, S. Schäfer, B. Leven , and B. Hillebrands: *Dissipation characteristics of quantized spin waves in nano-scaled magnetic ring structures*, J. Phys. D: Appl. Phys. **41**, 164017 (2008).

[Sch10] T. Schneider, A. A. Serga, A. V. Chumak, B. Hillebrands, R. L. Stamps, and M. P. Kostylev: *Spin-wave tunnelling through a mechanical gap*, EPL **90**, 27003 (2010).

[Sek10] K. Sekiguchi, K. Yamada, S. M. Seo, K. J. Lee, D. Chiba, K. Kobayashi, and T. Ono: *Nonreciprocal emission of spin-wave packet in FeNi film*, Appl. Phys. Lett. **97**, 022508 (2010).

[Ser10] A. A. Serga, A. V. Chumak, and B. Hillebrands: *YIG magnonics*, J. Phys. D: Appl. Phys. **43**, 264002 (2010).

[Shi11] H. Shimizu, K. Sakoda, and Y. Shimogaki: *CVD and ALD of Cobalt-Tungsten Alloy Film as a Novel Ccopper Diffusion Barrier*, 2011 IEEE International ((IITC/MAM)), 1-3 (2011).

[Sil99] T. J. Silva, C. S. Lee, T. M. Crawford, and C. T. Rogers: *Inductive measurement of ultrafast magnetization dynamics in thin-film Permalloy*, J. Appl. Phys. **85**, 7849 (1999).

[Sim01] R. N. Simons: *Coplanar Waveguide, Circuits, Components, And Systems*, John Wiley & Sons, New York, 2001.

[Sok11] M. Sokolovskyy, and M. Krawczyk: *The magnetostatic modes in planar one-dimensional magnonic crystals with nanoscale sizes*, J. Nanoparticle Res. **13**, 6085 (2011).

[Sta09] D. Stancil, and A. Prabhakar: *Spin Waves, Theory and Application*, Springer Science and Business Media, 2009.

[Stu11] T. Stückler: *Magnetowiderstand von ferromagnetischen Filmen auf 3D beschichteten Substraten*, Master's thesis, Technische Universität München (2011).

[Sun77] T. Suntola, and J. Antson: U.S. Patent **4,058,430** (1977).

[Sun92] T. Suntola: *Atomic layer epitaxy*, Thin Solid Films **216**, 84 (1992).

[Tac09] S. Tacchi, M. Madami, G. Gubbiotti, G. Carlotti, S. Goolaup, A. O. Adeyeye, H. T. Nguyen, and M. G. Cottam: *Field dependence of collective spin modes in transversely magnetized stripes with homogeneous and alternating width*, J. Appl. Phys. **105**, 07C102 (2009).

[Tac10a] S. Tacchi, M. Madami, G. Gubbiotti, G. Carlotti, A. Adeyeye, S. Neusser, B. Botters, and D. Grundler: *Magnetic Normal Modes in Squared Antidot Array With Circular Holes: A Combined Brillouin Light Scattering* *and Broadband Ferromagnetic Resonance Study*, IEEE Trans. Mag. **46**, 172 (2010).

[Tac10b] S. Tacchi, M. Madami, G. Gubbiotti, G. Carlotti, A. O. Adeyeye, S. Neusser, B. Botters, and D. Grundler: *Angular Dependence of Magnetic Normal Modes in NiFe Antidot Lattices With Different Lattice Symmetry*, IEEE Trans. Mag. **46**, 1440 (2010).

[Tac10c] S. Tacchi, M. Madami, G. Gubbiotti, G. Carlotti, S. Goolaup, A. O. Adeyeye, N. Singh, and M. P. Kostylev: *Analysis of collective spin-wave modes at different points within the hysteresis loop of a one-dimensional magnonic crystal comprising alternative-width nanostripes*, Phys. Rev. B **82**, 184408 (2010).

[Tog11] Y. Togawa, T. Kimura, K. Harada, A. Tonomura, and Y. Otani: *Control of magnetic domain wall displacement using spin current in small in-plane magnetic field in Permalloy nanowires*, J. Phys. D: Appl. Phys. **44**, 064015 (2011).

[Top08] J. Topp, J. Podbielski, D. Heitmann, and D. Grundler: *Internal spin-wave confinement in magnetic nanowires due to zig-zag shaped magnetization*, Phys. Rev. B **78**, 024431 (2008).

[Top09] J. Topp, J. Podbielski, D. Heitmann, and D. Grundler: *Formation and control of internal spin-wave channels in arrays of densely packed Permalloy nanowires*, J. Appl. Phys. **105**, 07D302 (2009).

[Top10] J. Topp, D. Heitmann, M. P. Kostylev, and D. Grundler: *Making a Reconfigurable Artificial Crystal by Ordering Bistable Magnetic Nanowires*, Phys. Rev. Lett. **104**, 207205 (2010).

[Top11a] J. Topp, G. Duerr, K. Thurner, and D. Grundler: *Reprogrammable magnonic crystals formed by interacting ferromagnetic nanowires*, Pure Appl. Chem. **83**, 1989 (2011).

[Top11b] J. Topp, S. Mendach, D. Heitmann, M. Kostylev, and D. Grundler: *Field- and geometry-controlled avoided crossings of spin-wave modes in reprogrammable magnonic crystals*, Phys. Rev. B **84**, 214413 (2011).

[Twi03] D. J. Twisselmann, and R. D. McMichael: *Intrinsic damping and intentional ferromagnetic resonance broadening in thin Permalloy films*, J. Appl. Phys. **93**, 6903 (2003).

[Vas96] J. O. Vasseur, L. Dobrzynski, B. Djafari-Rouhani, and H. Puszkarski: *Magnon band structure of periodic composites*, Phys. Rev. B **54**, 1043 (1996).

[Vii94] H. Viirola, and L. Niinistä: *Controlled growth of antimony-doped tin dioxide thin films by atomic layer epitaxy*, Thin Solid Films **251**, 127 (1994).

[Vin05] A. Vindigni, A. Rettori, L. Bogani, A. Caneschi, D. Gatteschi, R. Sessoli , and M. A. Novak: *Fast switching of bistable magnetic nanowires through collective spin reversal*, Appl. Phys. Lett. **87**, 073102 (2005).

[Vla10] V. Vlaminck, and M. Bailleul: *Spin-wave transduction at the submicrometer scale: Experiment and modeling*, Phys. Rev. B **81**, 014425 (2010).

[Vre92] R. Vreeburg, W. van Kooten, O. Gijzeman, and J. Geus: *The reduction of oxidized Ni(111)-Fe surfaces by hydrogen*, Surface Science **262**, 287 (1992).

[Wag61] C. Wagner: *Theorie der Alterung von Niederschlägen durch Umlösen (Ostwald-Reifung)*, Zeitschrift fr Elektrochemie, Berichte der Bunsengesellschaft fr physikalische Chemie **65**, 581 (1961).

[Wan90] Y.-C. Wang, and J. A. Okoro: *Impedance calculations for modified coplanar waveguides*, Int. J. of Electronics **68**, 861 (1990).

[WD39] R. Becker, and W. Döring: *Ferromagnetismus*, Julius Springer, 1939.

[Web12] D. P. Weber, D. Rüffer, A. Buchter, F. Xue, E. Russo-Averchi, R. Huber, P. Berberich, J. Arbiol, A. Fontcuberta i Morral, D. Grundler, and M. Poggio: *Cantilever Magnetometry of Individual Ni Nanotubes*, Nano Letters **12**, 6139 (2012).

[Wer97] W. Wernsdorfer, E. B. Orozco, K. Hasselbach, A. Benoit, B. Barbara, N. Demoncy, A. Loiseau, H. Pascard, and D. Mailly: *Experimental Evidence of the Néel-Brown Model of Magnetization Reversal*, Phys. Rev. Lett. **78**, 1791 (1997).

[Wol09] G. Woltersdorf, M. Kiessling, G. Meyer, J.-U. Thiele, and C. H. Back: *Damping by Slow Relaxing Rare Earth Impurities in* $Ni_{80}Fe_{20}$, Phys. Rev. Lett. **102**, 257602 (2009).

[Xio05] G. Xiong, J. W. Elam, H. Feng, C. Y. Han, H.-H. Wang, L. E. Iton, L. A. Curtiss, M. J. Pellin, M. Kung, H. Kung, and P. C. Stair: *Effect of Atomic Layer Deposition Coatings on the Surface Structure of Anodic Aluminum Oxide Membranes*, J. Phys. Chem. B **109**, 14059 (2005).

[Yam04] A. Yamaguchi, T. Ono, S. Nasu, K. Miyake, K. Mibu, and T. Shinjo: *Real-Space Observation of Current-Driven Domain Wall Motion in Submicron Magnetic Wires*, Phys. Rev. Lett. **92**, 077205 (2004).

[Yan01] M. Yan, Y. Koide, J. R. Babcock, P. R. Markworth, J. A. Belot, T. J. Marks , and R. P. H. Chang: *Selective-area atomic layer epitaxy growth of ZnO features on soft lithography-patterned substrates*, Appl. Phys. Lett. **79**, 1709 (2001).

[Yu12] H. Yu, R. Huber, T. Schwarze, F. Brandl, T. Rapp, P. Berberich, G. Duerr , and D. Grundler: *High propagating velocity of spin waves and temperature dependent damping in a CoFeB thin film*, Appl. Phys. Lett. **100**, 262412 (2012).

[Zig07] F. Zighem, Y. Roussigno, S.-M. Charif, and P. Moch: *Spin wave modelling in arrays of ferromagnetic thin stripes:*

application to Brillouin light scattering in permalloy, J. Phys.: Cond. Matter **19**, 176220 (2007).

Publications

- R. Huber, P. Klemm, S. Neusser, B. Botters, A. Wittmann, M. Weiler, S.T.B. Goennenwein, C. Heyn, M. Schneider, P. Böni, and D. Grundler: Advanced techniques for all-electrical spectroscopy on spin caloric phenomena, Solid State Communications 150, 492 (2010)

- R. Huber and D. Grundler: Ferromagnetic nanodisks for magnonic crystals and waveguides, Proc. SPIE 8100, Spintronics IV, 81000D (2011)

- S. Neusser, G. Duerr, F. Brandl, R. Huber, T. Schwarze, and D. Grundler: Transmission of GHz spin waves through periodically nanopatterned ferromagnets, Metamaterials 2011: The Fifth International Congress on Advanced Electromagnetic Materials in Microwaves and Optics, Metamorphose-VI, ISBN 978-952-67611-0-7, p. 922 (2011)

- S. Neusser, H.G. Bauer, G. Duerr, R. Huber, S. Mamica, G. Woltersdorf, M. Krawczyk, C.H. Back, and D. Grundler: Tunable metamaterial response of a Ni80Fe20 antidot lattice for spin waves, Phys. Rev. B 84, 184411 (2011)

- T. Schwarze, R. Huber, G. Duerr, F. Brandl, S. Neusser, K. Thurner, and D. Grundler: Microwave Antennas for Broadband Spectroscopy on Magnonic Metamaterials, Metamaterials 2011: The Fifth International Congress on Advanced Electromagnetic Materials in Microwaves and Optics, Metamorphose-VI, ISBN 978-952-67611-0-7, p. 576 (2011)

- T. Schwarze, M. Okuda, R. Huber, J.-C. Eloi, F. Brandl, L. Dreher, M.S. Brandt, D. Grundler, and W. Schwarzacher: Fabrication and characterization of crystallized magnetoferritin as an artificial magnetic metamaterial, Metamaterials 2011:

The Fifth International Congress on Advanced Electromagnetic Materials in Microwaves and Optics, Metamorphose-VI, ISBN 978-952-67611-0-7, p. 125 (2011)

- M. Bareiss, A. Hochmeister, G. Jegert, U. Zschieschang, H. Klauk, R. Huber, D. Grundler, W. Porod, B. Fabel, G. Scarpa, and P. Lugli: Printed array of thin-dielectric metal-oxide-metal (MOM) tunneling diodes, J. Appl. Phys. 110, 044316 (2011)
- R. Huber, T. Schwarze, P. Berberich, T. Rapp, and D. Grundler: Atomic layer deposition for the fabrication of magnonic metamaterials, Metamaterials 2011: The Fifth International Congress on Advanced Electromagnetic Materials in Microwaves and Optics, Metamorphose-VI, ISBN 978-952-67611-0-7, p. 588 (2011)
- G. Duerr, R. Huber, and D. Grundler: Enhanced functionality in magnonics by domain walls and inhomogeneous spin configurations, J. Phys.: Cond. Matter 24, 024218 (2012)
- D.P. Weber, D. Rüffer, A. Buchter, F. Xue, E. Russo-Averchi, R. Huber, P. Berberich, J. Arbiol, A. Fontcuberta i Morral, D. Grundler, and M. Poggio: Cantilever Magnetometry of Individual Ni Nanotubes, Nano Lett. 12, 6139 (2012)
- D. Rüffer, R. Huber, P. Berberich, S. Albert, E. Russo-Averchi, M. Heiss, J. Arbiol, A. Fontcuberta i Morral, and D. Grundler: Magnetic states of an individual Ni nanotube probed by anisotropic magnetoresistance, Nanoscale 4, 4989 (2012)
- H. Yu, R. Huber, T. Schwarze, F. Brandl, T. Rapp, P. Berberich, G. Duerr, and D. Grundler: High propagating velocity of spin waves and temperature dependent damping in a CoFeB thin film, Appl. Phys. Lett. 100, 262412 (2012)
- G. Duerr, K. Thurner, J. Topp, R. Huber, and D. Grundler: Enhanced transmission through squeezed modes in a self-cladding magnonic waveguide, Phys. Rev. Lett. 108, 227202 (2012)
- T. Schwarze, R. Huber, G. Duerr, and D. Grundler: Complete band gaps for magnetostatic forward volume waves in a two-dimensional magnonic crystal, Phys. Rev. B 85, 134448 (2012)

- R. Huber, M. Krawczyk, T. Schwarze, H. Yu, G. Duerr, S. Albert, and D. Grundler: Reciprocal Damon-Eshbach-type spin wave excitation in a magnonic crystal due to tunable magnetic symmetry, Appl. Phys. Lett. 102, 012403 (2013)
- S. Neusser, G. Duerr, R. Huber, and D. Grundler: Artificial crystals and metamaterials for spin waves from nanopatterned Ni80Fe20 antidot lattices, Chapter 14 (pp. 191 - 203) in Topics in Applied Physics: Magnonics, S.O. Demokritov, A.N. Slavin (Eds), Springer (2013)
- A. Buchter, J. Nagel, D. Rüffer, F. Xue, D. P. Weber, O. F. Kieler, T. Weimann, J. Kohlmann, A. B. Zorin, E. Russo-Averchi, R. Huber, P. Berberich, A. Fontcuberta i Morral, M. Kemmler, R. Kleiner, D. Koelle, D. Grundler, and M. Poggio, Phys. Rev. Lett. 111, 067202 (2013)
- J. Nagel, A. Buchter, F. Xue, O. F. Kieler, T. Weimann, J. Kohlmann, A. B. Zorin, D. Rüffer, E. Russo-Averchi, R. Huber, P. Berberich, A. Fontcuberta i Morral, D. Grundler, R. Kleiner, D. Koelle, M. Poggio, and M. Kemmler, Phys. Rev. B 88, 064425 (2013)
- R. Huber, T. Schwarze and D. Grundler: Nanostripe of Subwavelength Width as a Switchable Semitransparent Mirror for Spin Waves in a Magnonic Crystal, Phys. Rev. B 88, 100405(R) (2013)
- H. Yu, G. Duerr, R. Huber, M. Bahr, T. Schwarze, F. Brandl, and D. Grundler, Nature Commun. 4, 2702 (2013)

Acknowledgements

I would like to express gratitude to all people who supported me during this work. In particular:

- Univ.-Prof. Dr. Peter Vogl for supervision of the PhD examination, Univ.-Prof. Dr. Dirk Grundler for being the first examiner, Univ.-Prof. Paolo Lugli for being the second examiner.
- Univ.-Prof. Dr. Dirk Grundler for giving me the possibility to work at E10. The fruitful and interesting discussions led to deeper insight in physics.
- Dr. Paul Berberich for unrestricted support with the ALD, for reducing hundreds of ALD samples, and for help and advice in all situations.
- The collegues in the spin dynamics group: Florian Brandl, Thomas Schwarze, Georg Dürr, Sebastian Neusser, Florian Heimbach, Haiming Yu, and Tobias Stückler.
- Dr. Maciej Krawczyk at AMU Posnan for the calculations on 1D magnonic crystals.
- Prof. Dr. Anna Fontcuberta i Morral, Daniel Rüffer, Anna Dalmau, Eleonora Russo-Averchi, and Martin Heiss at EPF Lausanne for a fruitful collaboration.
- Prof. Dr. Jordi Arbiol at Universitat Autònoma de Barcelona in Spain for performing Transmission electron microscopy and electron energy loss spectroscopy.
- Prof. Dr. Paolo Lugli and Mario Bareiß at Institute for Nanoelectronics (TUM) for a fruitful collaboration.
- Prof. Dr. Sergei Nikitov, Dr. Yuri Filimonov, Dr. Yuri Khivintsev, Dr. Sergei Vysotsky, Dr. Aleksandr Kozhevnikov, and Valentin Sakharov at the Kotel'nikov Institute of Radio Engineering and Electronics of RAS in Moscow and Saratov for the support in Russia.
- Prof. Dr. Alexander Holleitner and Peter Weiser at the Walter Schottky Institut, Center for Nanotechnology and Nano-

materials for providing access to nanolithography facilities and respective support and maintenance.

- Photolithography masks have been provided by Claudia Paulus at the Walter Schottky Institut.
- Dr. Markus Becherer at the Chair of Technical Electronics (TUM) for support at the MFM.
- The group of M. Poggio at University of Basel for cantilever nanomagnetometry on Ni nanotubes.
- Roswitha Hoppen and Claudine Voelcker for organizational support.
- Thomas Rapp, Thomas Neukel, Stephan Lichtenauer, and Johannes Seitz for continuous technical support.
- Bernhard Gebauer for continuous help with the problems of VNA calibration.
- Everybody at E10 for good times at work, in particular Stephan Albert, Matthias Brasse, Stefanos Chalkidis, Amadeus Mlynarski, Klaus Thurner, Marc Wilde, and Tjark Windisch.
- My friends, my family, and Angi for providing me emotional support during the whole time.

The research leading to these results has received funding from the European Community's Seventh Framework Programme (FP7/2007-2013) under Grant No. 228673 (MAGNONICS), Grant No. 247556 (NoWaPhen), the Technische Universität München - Institute for Advanced Study, funded by the German Excellence Initiative, and the German Excellence Cluster Nanosystems Initiative Munich (NIM). The support is gratefully acknowledged.